Characterization and Modification of Fiber-based Photon Pair Sources

by

Jennifer Erskine

A thesis submitted to the Faculty of Graduate and
Postgraduate Studies under the supervision of B. J. Sussman
in partial fulfillment of the requirements for the degree of

Masters of Science

in Physics

Department of Physics
University of Ottawa

Abstract

Non-classical light sources are a fundamental building block of quantum photonic technologies. As these photonic technologies require higher numbers of sources and more specific source properties, it becomes increasingly important to characterize and manipulate these sources effectively. This thesis consists of three main projects, all relating to non-classical sources of light. First, we present a method for the rapid measurement of the joint spectral intensity of fiber-based photon pair sources. This method extends the concept of Stimulated Emission Tomography, using a chirped, broadband seed beam to stimulate the four wave mixing interaction. The use of the broadband seed, generated through supercontinuum generation, allows for measurements on the few second timescale and requires only a single pump laser to achieve high resolution joint spectra.

In the second project, we use this characterization tool to test a variety of different fiber-based photon pair sources. We use three different modification approaches (bending, squeezing, and tapering) to induce changes in the joint spectral properties of the photon pair sources. We show that each of these modifications has some impact on the joint spectra measured. The resulting joint spectra are very complex, highlighting the importance of performing measurements rather than relying on calculations alone.

Lastly, we demonstrate a fast switch for the manipulation of single photons. The switch uses the optical Kerr effect to rotate the polarization state of single photons at ultrafast timescales. The implementation of this switch is experimentally straightforward, using a commercial, single mode fiber as the Kerr medium and nJ level pump powers. We operate at an 80 MHz repetition rate and measure 97% switching efficiency, picosecond level switching speed, and approximately 800:1 signal to noise ratio from the operation.

Acknowledgements

I acknowledge the generous financial support of the University of Ottawa, the National Research Council of Canada (NRC), and the Natural Sciences and Engineering Research Council of Canada.

I am sincerely grateful to my supervisor, Ben Sussman, for his support, encouragement, and mentorship throughout my time at NRC. While I may never share his love of textbooks, his propensity to find you just the right book speaks to both his own depth of knowledge and his commitment to the academic growth of others.

I would also like to extend my heartfelt thanks to Duncan England, with whom I have had the pleasure of working and sharing an office. At every step of this thesis, Duncan has provided countless hours of support and guidance. Both in the lab and beyond, his help and feedback have helped me grow as a scientist, and I feel fortunate to have worked with him.

I appreciate the work of Denis Guay and Doug Moffatt, who have graciously provided valuable techical support for my experiments. I would also like to thank Rune Lausten for the considerable time he has spent teaching me about lasers, optics, and laboratory best practices. His insights, advice, and willingness to share his wealth of experience are much appreciated.

Many people at NRC have made my time there such a positive experience. In particular, I would like to acknowledge Connor Kupchak, whom I had the pleasure of working directly with on the Kerr switch experiment, Philip Bustard, for all that he taught me back when I was a summer student, and our excellent summer student Joscelyn van der Veen, for her enthusiasm and her assistance in the lab. I also thank Khabat Heshami for his theory insights, as well as Robert Walker and Huimin Ding for their generosity with their time and equipment.

Looking beyond physics, I am grateful to the femto, theory, and atto group members at NRC for lively conversations, both science related and otherwise, whether over lunch, Friday coffee, or an after-work drink. I also thank my friends at the University of Ottawa, in particular Davor, Guilmot, and Ludka, for all the fun times outside of class.

Last, but certainly not least, I am incredibly grateful for the unconditional love and support from my family.

Contents

Abstract ii

Acknowledgements iii

1 Introduction 1
1.1 Author's contributions . . . 2

2 Overview of Photon Pair Sources based on Nonlinear Optics 4
2.1 Introduction to single photon sources . . . 4
2.1.1 Deterministic single photon sources . . . 5
2.1.2 Probabilistic photon sources . . . 6
2.1.2.1 Entangled photons . . . 7
2.1.3 Attenuated coherent states . . . 8
2.2 Applications in quantum protocols . . . 8
2.2.1 Quantum computing . . . 9
2.2.2 Quantum cryptography . . . 11
2.3 Types of photon pair sources . . . 12
2.3.1 Nonlinear optical processes . . . 12
2.3.1.1 Spontaneous and stimulated processes . . . 13
2.3.2 Media of generation . . . 16
2.4 Photon source statistics . . . 18
2.4.1 Mean photon number and heralding efficiency . . . 18
2.4.2 Second order cross-correlation . . . 19
2.4.3 Second order autocorrelation . . . 21

3 Spectral Measurements of Photon Pair Sources 24
3.1 Joint spectral amplitude and intensity . . . 24
3.2 Spectrally resolved coincidence counting with monochrometers . . . 26
3.3 Dispersive fibers and time-resolved coincidence counting . . . 27
3.4 Fourier transform spectroscopy . . . 28
3.5 Stimulated emission tomography . . . 30
3.5.1 Phase sensitive measurements . . . 31
3.5.2 Characterization of entangled photon pairs . . . 31
3.6 Conclusion . . . 32

4 Joint Spectral Intensity Measurement using Broadband Light 33
4.1 Introduction . . . 33
4.2 Experimental setup . . . 34
4.2.1 Photon pair source . . . 36
4.2.2 Supercontinuum generation . . . 39
4.2.3 Idler calibration . . . 40
4.2.4 Idler normalization . . . 42
4.2.5 Seeding enhancement factor . . . 42
4.3 Results . . . 43
4.3.1 Asymmetry . . . 44
4.3.2 Speed . . . 47
4.3.3 Resolution . . . 48
4.4 Conclusion . . . 50

5 Tunable JSI through Fiber Modification 52
5.1 Introduction . . . 52
5.1.1 Background . . . 53
5.2 Experiment and results . . . 54
5.2.1 Squeezing . . . 56
5.2.1.1 Manual fiber polarization controller . . . 56
5.2.1.2 Micro-vise . . . 57
5.2.2 Bending . . . 61
5.2.3 Tapering . . . 64
5.3 Conclusion . . . 67

6 Optical Kerr Switching of Single Photons 69
6.1 Introduction . . . 69
6.1.1 Theory . . . 70
6.2 Experiment . . . 72
6.3 Results . . . 74
6.3.1 Characterization of the switched photons . . . 76
6.3.1.1 Second order autocorrelation . . . 77
6.3.1.2 JSI measurement . . . 78
6.4 Conclusion and applications . . . 80

7 Conclusion 81
7.1 Summary . . . 81
7.2 Future work . . . 82

Bibliography 84

Chapter 1

Introduction

Since the first laser was built in 1960, photonics has become an increasingly important and valuable field. Applications of lasers and photonics span a broad range of industries, including healthcare, communications, manufacturing, and sensing. They are found in our day to day lives, in the internet, printers, and barcode scanners, as well as in highly specialized applications, such as surgery and laser welding. In addition to present-day applications, photonics also promises to be an important platform for technologies of the future. One area where photonics will certainly play an essential role is the emerging field of quantum technologies. Quantum technologies have the potential for significant improvements in a variety of fields, including communication, computing, and sensing, among others. While certainly not the only route towards quantum technologies, quantum photonics has shown a lot of promise in many applications. With many quantum photonic protocols demonstrated on small scales, efforts to push to larger systems are ongoing.

An essential area of photonics is light sources, and quantum photonics requires non-classical light sources. This area of non-classical light sources is the focus of this thesis. The work outlined here shows a way of characterizing a particular type of non-classical light sources, photon pair sources. We demonstrate how this characterization method can be used to examine not just sources, but also processes and their effects on light. Tools such as this will be increasingly important as the field of quantum photonics grows and scales up to larger systems. With continuous research into both non-classical sources of light and quantum photonic processes, the ability to characterize these elements quickly and reliably will be essential.

1.1 Author's contributions

The work presented in this thesis is the result of scientific collaboration between myself and several others. In this section, I outline my personal contributions to each chapter discussed in this thesis.

Chapters 2 and 3 contain introductory and background material, and both were written by me. Chapter 4 describes a method for the rapid joint spectral measurements of photon pair sources using a chirped supercontinuum seed. The idea of performing Stimulated Emission Tomography with a chirped, broadband seed was proposed by Duncan England and Ben Sussman. Starting with a laser and an empty optical table, I designed and built the experimental apparatus with guidance from Rune Lausten and Duncan England. In particular, Rune Lausten and Duncan England provided considerable support in managing laser stability issues and diagnosing perceived problems in the experiment. I wrote the majority of the data acquisition software, with some assistance from Doug Moffatt. I was responsible for the collection and analysis of all data, except for the photon source statistics data, which was collected jointly with Duncan England. Lastly, I wrote the first draft of the paper based on this work. This was then edited by Duncan England, Ben Sussman, and myself, with small edits from Khabat Heshami and Connor Kupchak.

Chapter 5 outlines how the characterization apparatus from Chapter 4 was used to test two different fiber sources under modification. The general premise of looking at ways to dynamically tune fiber-based photon sources came from Duncan England. Ideas regarding how to modify the fibers were suggested by myself, Duncan England, Rune Lausten, and several members of the Fiber Group at the National Research Council (NRC). I prepared the fiber samples used for the squeezing and bending tests with the assistance of Robert Walker and Huimin Ding, and Huimin prepared all the fiber samples that were tapered. Denis Guay helped me with the procurement and set-up of the squeezing apparatus. I collected all data and performed all the analysis in this section. I also performed the calculations regarding expected birefringence induced by bending and lateral stress.

Chapter 6 describes the polarization switching of heralded single photons through the optical Kerr effect. For this experiment, much of the Kerr switching apparatus was built by Connor Kupchak for a previous demonstration. I built the heralded single photon source for the work demonstrated in Chapter 4. Duncan England proposed combining those to elements to demonstrate switching of heralded single photons. Connor Kupchak and I both contributed to modifying existing experimental apparatus to combine the photon source and Kerr switching sections. After the experiment was functioning with

good, but not great switching efficiency, I made improvements to the apparatus in an effort to improve the efficiency. Most preliminary data and some final data was taken jointly by myself and Connor Kupchak. For the final data set, I recorded the second order autocorrelation measurements and joint spectral data as well analyzed those sections, including the incoherent model comparison. Connor Kupchak made all the figures except the joint spectral intensity comparison figure, and he wrote the first draft of the paper. I contributed to editing the draft, as did Duncan England, Ben Sussman, and Connor Kupchak.

Chapter 2

Overview of Photon Pair Sources based on Nonlinear Optics

This chapter aims to provide an overview of photon pair sources based on nonlinear optics. The chapter will first outline the basic concepts of single photon sources, including deterministic and probabilistic sources, and highlight some common applications of single photons. Since this thesis focuses on probabilistic photon sources, the remainder of the chapter will provide a more in-depth discussion of photon pair sources. Theoretical background, descriptions of methods for experimental implementation, and statistics commonly used to characterize photon pair sources are discussed.

Several review papers provide a more extensive description of single photon sources [1–3].

2.1 Introduction to single photon sources

Over the past several decades, progress in single photon sources has been largely driven by keen interest across the globe in quantum information. Both public institutions and private corporations are putting significant resources towards the development of quantum technologies. Some quantum information protocols, including many protocols for Quantum Key Distribution (QKD), demand the use of single photons. Without true single photons, the security of these protocols is compromised, undermining the advantage of QKD over classical technologies. As such, single photon sources are currently a very active area of research.

For a single photon source, as with every piece of technology, there are certain qualities that define an ideal device. The perfect single photon source is an on-demand source

which produces exactly one photon, never zero photons and never more than one photon. Here, on-demand is taken to mean that a single photon can be produced at any particular time, as selected by the user. By extension, the ideal source is also capable of an arbitrarily fast repetition rate. Additionally, the photons emitted from the source are indistinguishable from each other, requiring well-controlled spatial and spectral properties [1]. A common term used to describe an ideal single photon source is a 'photon gun', where exactly one photon is emitted in a well-defined mode anytime the user triggers the source [3]. Real-world implementations of single photon sources strive towards these qualities, but certainly do not achieve them all. In practice, single photon sources are split into two categories to describe their principles of operation: deterministic and probabilistic sources. Both categories have their advantages and limitations, outlined in the following sections.

2.1.1 Deterministic single photon sources

Deterministic sources are so named because they come closest to fulfilling the 'on-demand' requirement of an ideal single photon source. These sources respond to an external excitation by producing a single photon. They include platforms such as quantum dots [4], colour centers [5], trapped ions [6], and ensembles of atoms [7] among others. The majority of deterministic sources fall into the category of single-emitter sources. These systems are chosen or engineered to approximate a two-level system. When a photon is desired, an external control places the system in its excited state. After some time, the system relaxes back to the ground state, producing a single photon [1]. In theory, a photon is produced every time the system is excited and there is no possibility of multi-photon emission. However in practice, not all photons are collected and noise and imperfections in the system contribute to multi-photon states. An important property of single-emitter sources is the lifetime of the excited state; long lifetimes can limit the the maximum repetition rate of the system and lead to greater uncertainty in the time of emission of the single photon. This can make it difficult to temporally overlap the photon with other optical elements or beams. The emitted photon may not radiate in the desired collection mode, resulting in loss of the signal photons; however, the use of a cavity around the single emitter can significantly improve collection efficiency [2]. Some approaches, such as quantum dots and colour centers can have distinguishability issues. Other approaches, such as trapped ions, have complex experimental requirements [1]. In addition to single emitters, deterministic sources can also use ensembles of atoms; these systems use collective excitations in the ensemble as the excited state. A common implementation uses Raman scattering (DLCZ protocol) [7]. While exciting the ensemble is a probabilistic process in this protocol, the

excitation can be read out very efficiently, so it is often grouped under deterministic photon sources.

While there remain some experimental challenges, deterministic photon sources are attractive in that if and when these challenges are addressed, they have the potential to approach ideal single photon sources. Unlike probabilistic sources, for deterministic sources there is no trade-off between source brightness and the probability of multi-photon emission. As deterministic sources become more compact and user-friendly, perhaps they will gain popularity [3], but for now probabilistic photon sources are the workhorse source for quantum optics experiments.

2.1.2 Probabilistic photon sources

The second approach to single photon sources involves probabilistic photon sources, also called photon pair sources or heralded single photon sources. These sources make use of nonlinear optical processes where correlated pairs of photons are generated. One or more pump beams are directed into a nonlinear medium, resulting in the creation, with some probablity, of a pair of correlated photons and the annihilation of one (or two) pump photon(s). The key idea is that these types of processes always generate a pair of photons, never a single photon. While it is not possible to predict whether a given pump pulse will create a photon pair, one of the two created photons can be used to 'herald' the existence of the other. After generation, the two daughter photons are separated and one is sent to a detector. Since the photons are created in pairs, detecting one of the two photons implies the existence of the other photon. A schematic of a heralded single photon source is shown in Figure 2.1.

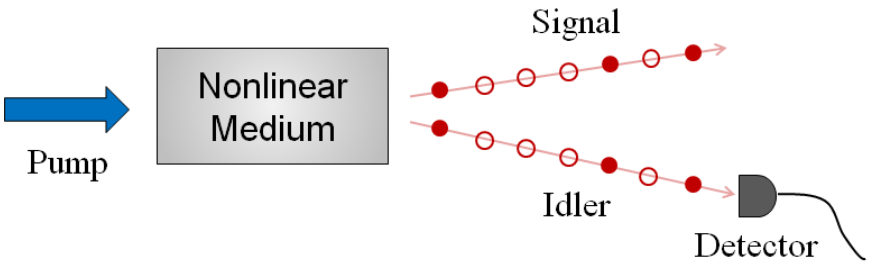

FIGURE 2.1: Schematic of a heralded single photon source: a strong beam pumps a nonlinear medium, generating a pair of photons. The filled red circles indicate pump pulse time bins where a photon pair was created, while the empty circles represent pump pulses where no photon pair was generated. One of the two photons is sent to a detector to herald the presence of the other photon.

Probabilistic photon sources have some inherent differences from the ideal single photon source, since there is always a non-zero probability of generating two or more photon

pairs. The vast majority of single photon detectors are not photon number resolving, therefore it is not possible to identify these multi-photon pair emissions through the herald detection. To limit the probability of multiple photon pairs, these sources are typically run with a pump power low enough that far less than one photon pair per pump pulse is generated. Clearly, this is far from the on-demand nature of an ideal single photon source. An additional issue arising from the probabilistic nature of photon pair sources is scalability. Since the probability of generating a photon pair on any given pump pulse is kept low by necessity, it becomes increasingly difficult to perform any experiments requiring more than one or two heralded single photons. Even experiments requiring 4 heralded photons takes a prohibitively long amount of time [8].

Loss in the system, limited detector efficiencies, and noise all negatively affect the source properties. When heralding photons (the idler photons shown in Fig. 2.1 are lost, their photon partner (the signal photon in Fig. 2.1) is wasted because there is no indication that a photon pair has been produced. When there is loss in the other (signal photon) channel, the creation of the photon pair is heralded, but the heralded single photon is lost and never arrives. Noise arising from detector dark counts, other nonlinear processes such as Raman scattering, or other sources also reduce the quality of the heralded single photon source. However, in general probabilistic photon sources can be set up for good indistinguishability and the single photons are emitted in a well-defined temporal mode. They are relatively straightforward to implement experimentally compared to some types of deterministic sources.

2.1.2.1 Entangled photons

While this section has focused on using photon pair sources as heralded single photon sources, another major application of photon pair sources is the generation of entangled photons. Entangled photon states are of broad interest to the quantum photonic community, with extensive applications in protocols for quantum teleportation [9] and linear quantum computing [10]. Entanglement occurs when the quantum state of the system of interest must be stated for the system as a whole. The quantum state cannot be factored such that it is the product of two states, one for each part of the system.

For example the following would represent a system of two photons, entangled in their polarization degree of freedom

$$|\Psi\rangle = \frac{1}{\sqrt{2}}\Big(|H\rangle_1 |H\rangle_2 + |V\rangle_1 |V\rangle_2 \Big), \tag{2.1}$$

where H and V represent a photon in the horizontally or vertically polarized photon respectively, and the subscripts 1 and 2 denote the states of the first and second photons.

For comparison, Eq. 2.2 shows a system which is not entangled and thus can be written as the product of two states

$$\begin{aligned} |\Psi\rangle &= \frac{1}{2}\Big(|H\rangle_1 |H\rangle_2 + |H\rangle_1 |V\rangle_2 + |V\rangle_1 |H\rangle_2 + |V\rangle_1 |V\rangle_2 \Big) \\ &= \frac{1}{2}\Big(|H\rangle_1 + |V\rangle_1 \Big) \otimes \Big(|H\rangle_2 + |V\rangle_2 \Big). \end{aligned} \tag{2.2}$$

By appropriate engineering of a photon pair source, entanglement can be produced in a variety of degrees of freedom, including polarization, time-frequency, direction of propagation, and orbital angular momentum (OAM) [11]. Polarization-entangled photon pairs are most widely used [12], largely because it is experimentally straightforward to manipulate the polarization state of light.

2.1.3 Attenuated coherent states

While they are arguably not single photon sources, attenuated (weak) coherent states are often used when low photon numbers are desired. To produce an attenuated coherent state, a light source, typically a laser, is attenuated to well below one mean photon per mode (or per pulse for a pulsed laser). In this regime, most modes contain no photons, some modes contain a single photon, and only a small proportion of modes contain more than one photon. This distribution is governed by Poissonian statistics and it is not possible for weak coherent states to have the sub-Poissonian (anti-bunched) number distribution desired for single photon sources [3]. Like probabilistic photon pair sources, there is a trade-off between the source brightness and the proportion of multi-photon events but unlike heralded single photon sources, it is not possible to detect which modes (pulses) contain one or more photons, rather than zero photons. However, attenuated coherent states are much easier to implement compared to 'true' single photon sources, explaining their popularity. Weak coherent states have been successfully used to demonstrate many quantum protocols [13, 14].

2.2 Applications in quantum protocols

The number and range of quantum protocols which have been or could be demonstrated with single photon sources is vast. Some of these applications include quantum sensing

and metrology [15, 16], quantum illumination and imaging [17, 18], quantum simulation [19], and quantum teleportation [9]. Two of the applications with the most active fields of research, quantum computing and quantum cryptography, are briefly described in the following subsections.

While photonics is a promising platform for many emerging quantum technologies, in all of the fields mentioned above there are also several different technology platforms currently being pursued. For example, trapped ions, quantum dots, superconducting qubits, and neutral atoms in optical lattices are all being investigated as paths towards quantum computing [20]. In many ways, these differering platforms are complementary, and eventual quantum networks will likely combine several different technologies. Each platform has its advantages and disadvantages, therefore different platforms are best suited for varying applications. Looking at photonics, photons do not interact strongly with their environment or each other, which makes it more difficult to implement photonic quantum logic gates, particularly two-qubit operations [1]. However, these same properties make photons very attractive for travelling over long distances, as they travel at the speed of light and are less susceptible to noise compared to many other platforms.

Just as classical technologies are far more powerful when networked together, networks of quantum technologies will be fare more interesting than isolated quantum technologies. Regardless of the platforms used by these technologies, photons are the obvious choice for medium and long-distance connections between different systems. Accordingly, the development of quantum photonic components, as well as ways to interface between photons and other technology platforms will continue to be a priority over the next many years.

2.2.1 Quantum computing

Quantum computing is of global interest, with many organizations racing to develop the first large-scale quantum computers. The main idea is that quantum systems can make use of properties inherent to quantum mechanics, such as entanglement and superposition, to perform computational tasks. When they are realized, these quantum computers could theoretically perform tasks either faster than a classical computer or tasks which are not practically feasible on a classical computer. This outperformance of classical computers is known as quantum supremacy. Two examples of such applications where quantum computers would have a definite advantage are the factorization of large integers into their prime factors through Shor's Algorithm [21] and the simulation of quantum systems [22]. Other quantum algorithms and a further description of quantum computing can be found in [23].

An incredible array of platforms are being explored for use in quantum computing. Some of these platforms include photons, superconducting circuits, trapped ions, cold atoms, impurities in silicon and diamond, and quantum dots [20]. Superconducting qubits in particular are a very promising platform for local quantum computation, since quantum logic gates are easily implemented through microwave pulses (one-qubit gates) or through inductive or capacitive coupling (two-qubit gates) [20].

Compared to these other platforms, photonics has some advantages and disadvantages. Photonic systems have far less noise at room temperature, and information can be encoded in photons in a variety of ways, including polarization, time-bins, and path [20]. However, it can be difficult to get photons to interact with each other, making two and three photon logic gates difficult to realize. A major step forward on this concern came with the publication of a scheme for linear optical quantum computing (LOQC) in the well-known KLM paper [10]. This protocol showed that efficient quantum computing can be implemented with only single photons, detectors, and linear optical circuits, and several experimental demonstrations with small numbers of qubits [24, 25] based on LOQC have been shown. While eliminating the need for nonlinear interactions, LOQC still requires ancilla resources, quantum teleportation, error correction, and near-perfect quantum gates, all of which are non-trivial requirements. With current efficiencies for quantum gates, photon sources, and detectors, the resources required for LOQC scale rapidly with the number of qubits desired [26], making large-scale photonic quantum computing a daunting task.

While it may not eventually win the race for universal quantum computing, photonics is extremely well suited for boson sampling, a non-universal form of quantum computation [27]. Boson sampling involves sending an input state consisting of n photons in m modes through a linear optics network. The network implements a unitary map on the input state, and the output of the network is a superposition of all possible output configurations. With boson sampling, a measurement is performed at the network output to sample this superposition, resulting in the measurement of one of these configurations. The probability distribution of measuring particular output configurations is related to the calculation of matrix permanents. Particularly for large matrices with complex elements, calculating matrix permanents is considered a difficult problem for classical computers, and quantum boson sampling may provide a computational advantage [28]. Photonic boson sampling requires only indistinguishable photons, passive linear optical elements, and single photon detectors, all of which are well-established photonic technologies. It does not require nonlinear interactions or entanglement between photons, which are more challenging to implement but required for universal photonic quantum computation. This makes boson sampling a much easier concept to implement experimentally, and several demonstrations have already been performed [19, 29]. While

current demonstrations use only a small number of photons, as these systems are scaled up, they may provide a strong example of quantum supremacy.

2.2.2 Quantum cryptography

Quantum cryptography, and specifically Quantum Key Distribution (QKD), is one of the most exciting applications of non-classical states of light. Some of the basic principles of quantum mechanics make it inherently well suited for cryptographic applications. For example, the inability to perfectly replicate an unknown quantum state (No Cloning Theorem), the inability to make measurements in orthogonal bases simultaneously, and the inherent disruption to a quantum state through measurement can all be exploited to ensure secure communication [13]. The most well-known protocol for QKD, called BB84, was developed by Charles Bennett and Gilles Brassard [30].

Several other protocols exist, such as the Ekert protocol, as well as many variations on the BB84 protocol. All of these require non-classical states of light, particularly either single photons (BB84), or entangled photon pairs (EPR) [13]. Experimentally, many demonstrations of these protocols have been performed with photon pair sources, such as in [31–33]. Demonstrations are pushing further and further beyond the laboratory scale, with successful results in free space links [34], kilometer scale fiber networks [35], and satellite communication [36]. A small number of commercial companies have also developed commercial QKD systems.

Due to the relative ease of implementation, many QKD demonstrations are done using attenuated coherent states. Both attenuated coherent states and photon pair sources have inherent probabilities of generating multi-photon states, however, photon pair sources offer a significant advantage when it comes to detector and channel noise [13]. To keep the probability of a mode containing more than one photon low, both methods of generating single photons operate in regime of low mean photon number ($\mu < 1$), and thus most modes contain no photons. However, noise in the channel and detector dark counts become problematic, as a noise photon can be detected when no signal photon was really sent. This is a much larger problem for attenuated coherent sources. Since the sender and receiver don't know when a photon was sent, the detectors must be active all the time; this increases the number of noise photons that will be detected. In a heralded single photon source, the detectors only need to be active when a herald photon is detected, significantly increasing the signal to noise ratio [13].

2.3 Types of photon pair sources

Probabilistic single photon sources are generally based on one of two nonlinear optical processes: spontaneous parametric downconversion (SPDC) and spontaneous four wave mixing (SFWM). Single photons can also be generated through a third nonlinear process, Raman scattering, through the Duan, Lukin, Cirac, Zoller (DLCZ) protocol [7]. In this two-step protocol, once the system is in the excited state the excitation can generally be read out very efficiently, emitting a single photon. Accordingly, this protocol is typically grouped under deterministic photon sources and will not be covered in greater depth in this section.

Sources based on SPDC and SFWM can be implemented in a variety of materials; the most common being nonlinear crystals, such as β-barium borate (BBO) and potassium dihydrogen phosphate (KDP) for SPDC, and fibers and waveguides for SFWM. However, photon pair generation has also been observed in alternative media, such as microring resonators [37]. As the work described in this thesis is based on the SFWM process, this chapter will use equations that describe SFWM. However, the description of SPDC is very similar and follows naturally if one replaces the two pump photons from SFWM with a single photon for SPDC. Much of the experimental work presented in this thesis can be extended to SPDC as well.

2.3.1 Nonlinear optical processes

A schematic illustrating the energy level diagrams for both SPDC and SFWM is shown in Figure 2.2.

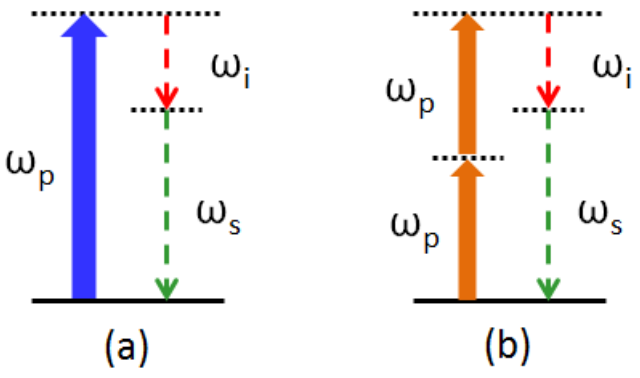

FIGURE 2.2: Energy level diagram of (a) spontaneous parametric down conversion (SPDC) and (b) degenerate four wave mixing. In both cases, one signal photon (ω_s) and one idler photon (ω_i) are created and one (SPDC) or two (SFWM) pump photons (ω_p) are annihilated. Thick arrows denote a strong beam, and dotted lines denote single photons.

Both processes involve the annihilation of pump photon(s) and the creation of two photons (usually termed signal and idler). Both are parametric processes, meaning that no energy is left in the material and the final quantum state is the same as the initial quantum state [38]. The difference between SPDC and SFWM is that in SPDC, only one pump photon is annihilated during the process, while in SFWM, two pump photons are annihilated. In SFWM, the two pump photons can be either the same wavelength (degenerate SFWM) or different wavelengths (non-degenerate SFWM).

SPDC can only occur in materials with a second order $\left(\chi^{(2)}\right)$ nonlinearity, while SFWM can occur in any materials with a third order $\left(\chi^{(3)}\right)$ nonlinearity. In general $\chi^{(2)}$ is much larger than $\chi^{(3)}$ (on the order of 10^{12} times larger); this is why efficient second order processes can be performed in bulk crystals, but third order processes often use waveguides to increase the interaction length of the process. However, many materials possess symmetry such that $\chi^{(2)} = 0$. Any materials which are centrosymmetric, in other words possess inversion symmetry, must have a second order nonlinearity of 0 [38].

Since both SPDC and SFWM are parametric processes with no energy stored in the medium, photon energy and linear momentum must be conserved. Using a general equation for SFWM, energy conservation is obtained by ensuring

$$\omega_1 + \omega_2 = \omega_3 + \omega_4, \tag{2.3}$$

where ω_1 and ω_2 are pump photons, and ω_3 and ω_4 are the signal and idler photons.

The conservation of momentum can be represented by the following equation

$$\Delta\vec{k} = \vec{k}_1 + \vec{k}_2 - \vec{k}_3 - \vec{k}_4 \tag{2.4}$$

where Δk is the phase mismatch term and $k_i = \frac{2\pi}{\lambda_i}$ is the wave vector for photons $i = 1, 2, 3, 4$. For a parametric nonlinear process to occur efficiently, it must be well phase-matched ($\Delta k << 1$). When processes are not well phase-matched, light generated at different points in the medium are out of phase and destructively interfere, limiting overall efficiency.

2.3.1.1 Spontaneous and stimulated processes

The concepts of down-conversion and four wave mixing can be understood as entirely classical, nonlinear optical effects. Taking non-degenerate four wave mixing as an example, one can send the pump beams as well as a beam at the signal wavelength into the

nonlinear medium. The interaction between the pump and signal causes the generation of the idler beam and amplification of the signal, termed stimulated four wave mixing. Note that equally, one could seed the process with a beam at the idler wavelength and generate the signal wavelength.

The following equations are outlined in [38]

The total electric field can be defined as the sum of the two pump beams (subscripts 1 and 2) and the signal beam (subscript 3)

$$\widetilde{E}(t) = E_1 e^{i\omega_1 t} + E_2 e^{i\omega_2 t} + E_3 e^{i\omega_3 t} + c.c., \tag{2.5}$$

where E_i is the amplitude of the electric field at frequency ω_i and c.c. stands for complex conjugate. Given that the polarization $\widetilde{P}(t)$ of a material depends on the electric field in both a linear and a nonlinear way, we can describe this total polarization by

$$\widetilde{P}(t) = \epsilon_0 \Big[\chi^{(1)} \widetilde{E}(t) + \chi^{(2)} \widetilde{E}^2(t) + \chi^{(3)} \widetilde{E}^3(t) + ... \Big]. \tag{2.6}$$

Of specific interest for the four wave mixing process is the $\chi^{(3)}$ nonlinear effect, which depends on the electric field to the third power. As previously discussed, any materials with inversion symmetry have a $\chi^{(2)} = 0$, making $\chi^{(3)}$ the dominant nonlinear effect

$$\widetilde{P}^{(3)}(t) = \epsilon_0 \chi^{(3)} \widetilde{E}^3(t). \tag{2.7}$$

Subbing in Equation 2.5 into Equation 2.7 and expanding, it is evident that $\widetilde{P}^{(3)}(t)$ contains energy at new frequencies that were not present in $\widetilde{E}(t)$. Moving to a Fourier series representation, the complex amplitude of the frequency components present can be represented by $P(\omega_n)$, where n spans all positive and negative frequencies present in $\widetilde{P}^{(3)}(t)$. Then any time domain signal can be represented as

$$\widetilde{P}(t) = \sum_n P(\omega_n) e^{-i\omega_n t}. \tag{2.8}$$

Examining the four wave mixing process, the amplitude corresponding to the new frequency generated through the process (ω_4) can be expressed as

$$P^{(3)}(\omega_4 = \omega_1 + \omega_2 - \omega_3) = 6\epsilon_0 \chi^{(3)} E_1 E_2 E_3^*., \tag{2.9}$$

where the * denotes a complex conjugate. Looking at the specific case of degenerate four wave mixing and stimulating the interaction with the signal beam, Equation 2.9 can be rewritten as

$$P^{(3)}(\omega_i = 2\omega_p - \omega_s) = 6\epsilon_0 \chi^{(3)} E_p^2 E_s^*. \tag{2.10}$$

From Equation 2.10 it is evident that the amplitude of the polarization at the idler frequency depends quadratically on the amplitude of the pump field and linearly on the amplitude of the signal field and on $\chi^{(3)}$. Equivalently, the intensity of the output idler beam varies quadratically with the pump intensity and linearly with the signal intensity. Note that in the case of stimulating the interaction with the idler (rather than the signal), the s and i labels can simply be swapped in Equation 2.10.

The classical derivation would imply that if one of the driving fields in a nonlinear process is not present (has an amplitude of 0) that the polarization amplitude of any frequency terms involving that driving field would also be 0, and those processes would never occur. However, the quantum mechanical approach implies a different result.

In quantum mechanics, even a mode that contains no photons has a zero point energy ($\frac{1}{2}\hbar\omega$). For optical modes, this is usually thought of as originating from the vacuum field [39]. The vacuum field can be though of a fluctuating, random field that is present everywhere. While the mean of the vacuum field is zero, the mean of the vacuum field squared is non-zero.

To show this mathematically following from [40], first we define a number state containing n photons to be an eigenstate of the number operation ($\hat{a}^\dagger \hat{a}$) where $\hat{a}^\dagger$ and $\hat{a}$ are the usual creation and annihilation operators

$$\hat{a}^\dagger \hat{a} \left|n\right\rangle = n \left|n\right\rangle. \tag{2.11}$$

Then the mean value of the field squared for a given number eigenstate is given by

$$\begin{aligned} \left\langle n\right| \hat{E}^2(z,t) \left|n\right\rangle &= \epsilon_0^2 sin^2(kz) \left\langle n\right| \hat{a}^{\dagger 2} + \hat{a}^2 + \hat{a}^\dagger \hat{a} + \hat{a}\hat{a}^\dagger \left|n\right\rangle \\ &= 2\epsilon_0^2 sin^2(kz)\left(n + \frac{1}{2}\right). \end{aligned} \tag{2.12}$$

Clearly, even when there are no photons ($n = 0$) there is still some energy present in the field.

Therefore, in the quantum mechanical approach, nonlinear processes can occur even if one of the fields involved has an average amplitude of 0. For example, four wave mixing can occur even when only the pump field is present, and there is no beam at the signal

or idler field to stimulate the process. In this case, the four wave mixing interaction can be thought of as being stimulated by the vacuum field. This situation is referred to as spontaneous four wave mixing (SFWM). Similarly, for the $\chi^{(2)}$ process the terms spontaneous parametric down-conversion (SPDC) and Difference Frequency Generation (DFG) are generally used for the spontaneous and stimulated cases respectively. The difference between a stimulated and a spontaneous nonlinear process is shown in Fig. 2.3.

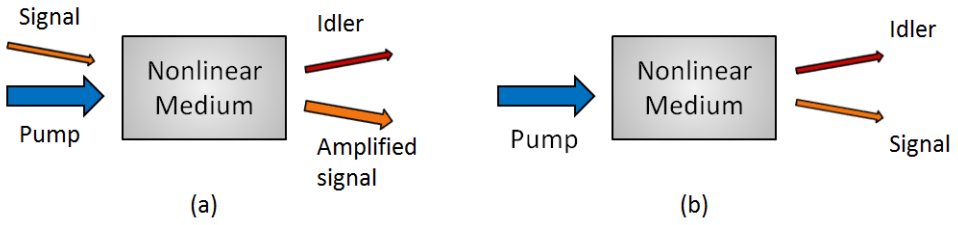

FIGURE 2.3: Schematics of (a) a stimulated nonlinear process and (b) a spontaneous nonlinear process. (a) could represent either stimulated four wave mixing or difference frequency generation, while (b) could represent either spontaneous four wave mixing or spontaneous parametric downconversion.

2.3.2 Media of generation

Most nonlinear processes are performed in either bulk media, such as a nonlinear crystal, or in a waveguide such as an optical fiber. Nonlinear crystals are generally birefringent, with some axis (or axes) of propagation having a larger index of refraction than another axis. While some types of nonlinear optical effects can be done in regular silica fiber (for example Kerr effect processes), often some level of birefringence is also required in the optical fiber to achieve proper phase-matching. Phase matching can also be achieved in some photonic crystal fibers (PCFs), which can be designed to have regions of low or anomalous dispersion. Where birefringence is desired, polarization maintaining fibers (PMFs) can be used. A PMF has two axis of propagation, at right angles to each other, which have different indices of refraction. Due to the birefringence, linearly polarized light launched along either of these two axes will maintain its polarization state, hence the name polarization maintaining fibers.

There are three main types of PM fibers; all three need some way to break the symmetry of a regular fiber, as shown in Figure 2.4. The elliptical core fiber uses a non-circular core to define the two axes of propagation. The panda and bow-tie type fibers both use stress rods placed in the fiber to introduce stress along a particular axis in the core. The stress rods are made of material with different thermal properties than the fiber cladding, so as the fiber is drawn and cools, the different materials will expand and contract at different rates [41].

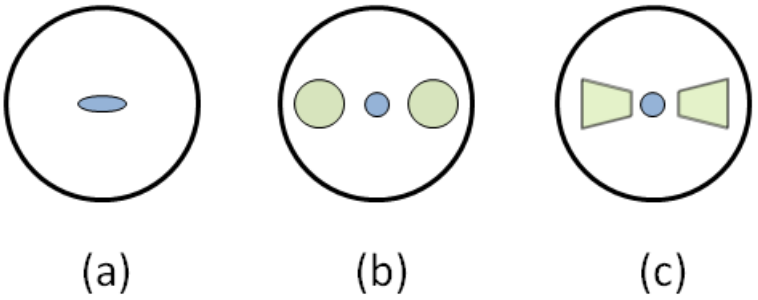

FIGURE 2.4: Illustrations of three types of polarization mainting fiber (PMF), including (a) elliptical core fiber (b) panda type fiber (c) bow-tie type fiber. In these illustrations, the blue area represents the core of the fiber, while the green area represents stress rods. For all three fiber types, the slow axis is oriented horizontally and the fast axis is oriented vertically. Illustrations are not to scale.

There are several reasons why performing nonlinear optics in fiber is advantageous. In general, fibers can provide good spatial confinement over longer interaction lengths as compared to bulk media. In bulk media, the beams are focussed to their beam waist (w_0) and then quickly diverge on the scale of a Rayleigh range $\left(z_r = \frac{\pi w_0^2}{\lambda}\right)$. In many applications, one tries to maximize the product of the beam intensity at the focus and the length of the interaction region (which scales with the Rayleigh range). However, the intensity scales with $\frac{1}{w_0^2}$ and the Rayleigh range scales with w_0^2. Conversely in fiber the beam is guided by the fiber core (often on the order of a few microns in diameter) and remains guided over the length of the fiber, which can be much longer than the equivalent Rayleigh range for that beam waist. Performing nonlinear optics in fiber also helps ensure a well-defined output spatial mode, which is particularly helpful if recoupling to a single mode fiber afterwards.

There are also some downsides to performing nonlinear optics in fiber. Depending on the pulse durations and energies, temporal walkoff between the two pulses due to material dispersion can limit the effective interaction length. Since the refractive index is wavelength dependent, pulses at different wavelengths will travel at different speeds, gradually moving away from each other as they propagate through the fiber. Additionally, with a longer interaction region, intensity dependent phenomena such as self phase modulation and cross phase modulation can have more noticeable effects, and attenuation due to absorption or losses to other modes can be significant. Fiber can also limit the power used for an interaction, since too much power can cause material damage. In general, these downsides also apply to bulk media with a long interaction length. In contrast, bulk media are often advantageous because they can be easily tuned for phase matching. Many bulk nonlinear optical crystals can be angle tuned or temperature

tuned to achieve the desired birefringence. In contrast, fibers are quite difficult to tune. However, this idea of fiber tuning is quite interesting and forms the basis of Chapter 5.

Significant progress has been made recently in on-chip SPDC and SFWM sources, largely using silicon or lithium-niobate based waveguides [42]. Some of these structures, such as periodically poled crystals in waveguides [38, 43] take advantage of both the high nonlinearities of nonlinear crystals and the tight confirnement of waveguides. Structures such as spiralled waveguides [44] and ring-resonators have been used [37], with high spectral purity and high visibility quantum interference successfully demonstrated. However, further discussion on integrated sources is outside the scope of this work.

2.4 Photon source statistics

In general, photon statistics can be used to describe and classify types of light, such as thermal and coherent light. Importantly, photon statistics can be used to measure whether light is nonclassical. Nonclassical light can only be described using quantum optics, and cannot be described with classical electromagnetism.

2.4.1 Mean photon number and heralding efficiency

A commonly used metric for sources generating very low levels of light is the mean photon number per mode μ. This is used to describe both single photon sources and highly attenuated coherent beams, which are often used as substitutes for true single photon sources. An ideal single photon source would have a mean photon number of one, with every mode containing exactly one photon. In both probabilistic sources and attenuated coherent beams however, there is a trade-of between the total number of photons produced and the proportion of modes which contain more than one photon. Note that this trade-off does not exist for deterministic single photon sources. For particular applications, such as quantum cryptography, an optimal value for μ exists when using probabilistic photon sources. This optimal value depends on losses in the communication channel as well as assumptions made about the technology of a potential eavesdropper [13].

For heralded photon sources, another important metric is the heralding efficiency of the system (η). Here, we define the heralding efficiency as the conditional probability of detecting a heralded photon, given that a herald photon has been collected and detected. This can be expressed as [45]

$$\eta = \frac{N_C}{N_H} \tag{2.13}$$

where N_C and N_H are the number of two-fold coincidences detected and the number of herald photons detected in a set time interval respectively. Note that the heralding efficiency can be defined in a range of ways, depending on the application [45]. For example, one could define a heralding efficiency for the collection of a heralded photon directly after the source, or one could define a heralding efficiency for a photon which propagates through a more complex system before being detected. Often, approximate or measured values for the detector efficiency are factored out of the heralding efficiency to calculate the losses in the channel before the detector.

2.4.2 Second order cross-correlation

Correlation functions are generally used to study the statistical properties of light. First order correlation functions are related to correlations in the amplitude fields, while second order correlation functions look at intensity correlations. First order correlation functions are not sufficient to distinguish between different types of light, such as thermal or coherent light [46]. However, higher order correlation functions can make this determination, thus the second order correlation function is generally used to assess properties of light sources.

The second order cross-correlation function is used to examine correlations in the photon number degree of freedom between the signal and idler of a photon pair source. Additionally, it can be used to determine whether a heralded single photon source produces non-classical states of light. The cross-correlation function is defined in Equation 2.14

$$g_c^{(2)}(\tau) = \frac{\langle I_1(t) I_2(t+\tau) \rangle}{\langle I_1(t) \rangle \langle I_2(t) \rangle}, \tag{2.14}$$

where $g_c^{(2)}(\tau)$ is the second order cross-correlation at time delay τ and I_1 and I_2 are the intensities of the two beams. For very low intensities where the probability of detecting more than one photon per detector at a time is low, we can approximate the second order cross-correlation as

$$g_c^{(2)}(\tau) = \frac{P_{i,s}(\tau)}{P_i P_s}, \tag{2.15}$$

where $P_{i,s}(\tau)$ is the probability of detecting a coincidence between a signal and idler photon with τ delay between them, and P_i, P_s are the probabilities of detecting an

idler photon and a signal photon respectively. The probability of event x is simply $P_x = N_x/N_p$ where N_x represents the number of events in a given time interval and N_p represents the number of trials (pump pulses) in that same time interval. Therefore, we can rewrite Eq. 2.16 at zero time delay as

$$g^{(2)}_{s,i}(0) = \frac{N_{s,i}N_p}{N_s N_i}. \tag{2.16}$$

The value of of the cross-correlation function at $\tau = 0$ $\left(g^{(2)}_c(0)\right)$ can be used to classify states of light. Coherent light has $g^{(2)}_c(0) = 1$, while single mode thermal states have $g^{(2)}_c(0) = 2$ [46]. It can also be used to show that a photon pair source is indeed nonclassical by showing a violation of the Cauchy-Schwarz inequality [47]

$$\left(g^{(2)}_{s,i}(0)\right)^2 \leq g^{(2)}_{s,s}(0) \cdot g^{(2)}_{i,i}(0), \tag{2.17}$$

where $g^{(2)}_{s,s}(0), g^{(2)}_{i,i}(0)$ are second order autocorrelation functions given by $g^{(2)}_{x,x}(0) = P_{x,x}/P_x^2$. Since no classical states or light have a second order cross-correlation function at $\tau = 0$ greater than 2, any measurement of $g^{(2)}_c(0) > 2$ indicates a non-classical state.

Another commonly used measure of heralded single photon source correlations is the Coincidence to Accidental Ratio (CAR) [48, 49]. The CAR is the ratio between the rate of coincidences between the signal and idler photons at zero relative delay compared to the rate of accidental coincidences arising from uncorrelated photons. For a pulsed source, this accidental ratio is simply the rate of coincidences at a relative signal/idler delay of any integer number of pulse periods (mT) [49] where m is an integer an T is the pulse period

$$CAR = \frac{P_{s,i}(0)}{P_{s,i}(mT)}. \tag{2.18}$$

In a probabilistic heralded single photon source, the probability of a coincidence between a signal and idler from adjacent pulses is simply the product of the individual probabilities of detecting a signal and idler photon ($P_{s,i}(T) = P_i P_s$). In this case, we see that Eq. 2.18 reduces to Eq. 2.15 and the CAR is the same as the second order cross-correlation at zero time delay.

For an ideal source with ideal detectors (where $P_s = P_i = P_{s,i}$), $g^{(2)}_{s,i}(0)$ scales as $1/P_i$. In real systems, $g^{(2)}_{s,i}(0)$ can deviate from this trend due to detector dark counts, other noise in the channel, or low heralding efficiency [49].

2.4.3 Second order autocorrelation

An ideal photon pair source emits a maximum of one photon pair per pump pulse. However, for photon pair sources based on nonlinear optics such as PDC and SFWM, there is always a non-zero probability of creating multiple photon pairs from a single pump pulse. Noise in the system can also lead to multiple photons in a given mode or false detection events (electrical dark counts). One way to characterize the probability of these multiple photon pair events and the noise in the system is through the heralded second-order autocorrelation function. To perform this measurement, the signal photons are split with a 50/50 beamsplitter and sent to two separate detectors (s1 and s2), as shown in Fig. 2.5. The heralded autocorrelation is given by

$$g_H^{(2)}(0) = \frac{P_{s1,s2|i}}{P_{s1|i}P_{s2|i}} = \frac{N_{s1,s2,i}N_i}{N_{s1,i}N_{s2,i}}, \tag{2.19}$$

where $P_{x|y}$ is the conditional probability of event x occuring given that event y occured.

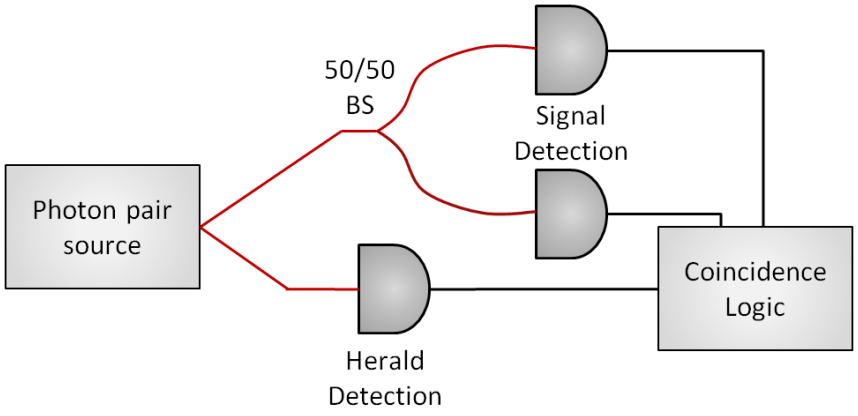

FIGURE 2.5: Schematic showing a second order autocorrelation measurement. The signal photons are split on a 50/50 beamsplitter (BS).

For an ideal photon pair source in a noiseless system, no coincidences ever occur between signal detectors s1 and s2, so the heralded autocorrelation is 0. In actual photon pair sources, a heralded autocorrelation as low as possible is preferred. In general, the heralded autocorrelation increases with pump power, since increased pump power results in an increase in the mean number of photons per pulse (μ). Poissonian statistics dictate that as μ increases, so does the probability of creating more than one photon pair in a single pump pulse. Dark counts and other noise also contribute to a higher autocorrelation.

Another important measure of a heralded single photon source is the purity of the single photons, which can be examined using the unheralded autocorrelation function

$$g_U^{(2)}(0) = \frac{P_{s1,s2}}{P_{s1}P_{s2}} = \frac{N_{s1,s2}N_p}{N_{s1}N_{s2}}. \tag{2.20}$$

This unheralded autocorrelation relates to the purity (P) of the heralded single photons. It also provides a measure of the Schmidt Number (K), or the effective number of modes contributing to the source, as outlined in [47, 50] through the following relationship

$$g_{s,s}^{(2)}(0) = 1 + 1/K = 1 + P. \tag{2.21}$$

A quantum state consisting of a single mode (P=1) has a photon number distribution which is thermal (Bose-Einstein distribution) where $g_U^{(2)}(0) = 2$ [51], while a highly mixed state containing many modes (P→0) has a photon number distribution which approaches a Poissonian distribution ($g_U^{(2)}(0) = 1$) [50].

Written in terms of the mean photon number $\bar{n}$ per mode, the Bose-Einstein distribution has the form [51]

$$p(n) = \frac{\bar{n}^n}{(1+\bar{n})^{1+n}}, \tag{2.22}$$

and a variance given by

$$\Delta n^2 = \bar{n}^2 + \bar{n}, \tag{2.23}$$

where $p(n)$ is the probability of a mode containing n photons. A Poissonian distribution has the form

$$p(n) = \frac{e^{-\bar{n}}\bar{n}^n}{n!}, \tag{2.24}$$

and a variance given by

$$\Delta n^2 = \bar{n}, \tag{2.25}$$

When photon pair sources are used as heralded single photon sources, high purity is desired. Correlations between the herald and signal photon, such as spectral correlations, decrease the signal photon purity. Accordingly, spectral and spatial filters are often used to increase purity [47]. However, this inherently reduces the overall number of heralded photons. Efforts have also been made to produce high purity heralded single photons without spectral filtering through appropriate engineering of the photon pair source, both in bulk media [52] and in silica and silicon based microstructures [37, 47].

In summary, this chapter has outlined the importance of single photon and photon pair sources, as well as described the basic principles of photon pair sources based on SPDC and SFWM. As discussed at the end of the chapter, the purity of heralded single photons

from SPDC and SFWM is of significant interest and importance for many quantum applications. Spectral correlations between the signal and idler photons significantly impact the the purity of these photon sources, and the next chapter outlines different approaches for measuring these correlations.

Chapter 3

Spectral Measurements of Photon Pair Sources

For many applications of photon pairs, it is important to measure the spectral properties of the photon pair source. It is important to know the wavelengths of the output modes as well as their bandwidths. Additionally, it is useful to know about the spectral correlations between the two output modes. Will measuring the wavelength of one of the two output photons provide any information regarding the spectral properties of the other output photon? This spectral correlation information is usually represented through a Joint Spectral Amplitude (JSA) or a Joint Spectral Intensity (JSI). This chapter will provide an overview of spectral correlation measurements and the different measurement approaches used over the years.

For additional discussion and comparison of different joint spectrum measurement approaches, the majority of the topics discussed in this chapter are covered in greater depth in a review aticle [53] published in 2017.

3.1 Joint spectral amplitude and intensity

The joint spectral amplitude (JSA) and joint spectral intensity (JSI) are both ways of characterizing the spectral correlations between the two daughter photons of a photon pair source. The JSA, also known as the biphoton wavefunction, is phase-sensitive, while the JSI is not. Both the JSI and JSA are a product of two functions: the phasematching function and the pump bandwidth. In essence, the pump bandwidth provides information regarding the distribution of wavelengths present in the pump. The pump spectral amplitude term(s) in the JSA/JSI relate to the conservation of energy for a given set of

signal, idler, and pump photons. Similarly, for a given pump photon (or pair of pump photons) and a given signal/idler photon pair, the phasematching function represents how well momentum is conserved for those wavelengths. The phase mismatch is related to the probability that the nonlinear process will occur for those wavelengths.

The phasematching function is defined as

$$\phi(\omega_s, \omega_i) = \text{sinc}\Big(\frac{\Delta k L}{2}\Big) \exp\Big(\frac{i \Delta k L}{2}\Big), \tag{3.1}$$

where L is the interaction length. The Δk term is the phase mismatch given by the difference in wavevectors ($k = \frac{2\pi}{\lambda}$) between the pump, signal, and idler. For a degenerate SFWM process, the phase mismatch is defined by Equation 3.2

$$\Delta \vec{k} = 2\vec{k}_p - \vec{k}_s - \vec{k}_i. \tag{3.2}$$

For a SPDC process, you simply remove the factor of 2 in front of k_p, since only one pump photon is annihilated.

As discussed in [54], for a degenerate SFWM process that occurs in a birefringent fiber, the phase mismatch can be defined as

$$\Delta k = 2\frac{\omega_p}{c}\Big(n(\omega_p) + \Delta n\Big) - \frac{\omega_s}{c} n(\omega_s) - \frac{\omega_i}{c} n(\omega_i) + \frac{2}{3}\gamma P, \tag{3.3}$$

where c is the speed of light, $n(\omega)$ is the refractive index, Δn is the added offset in refractive index of the slow fiber axis, which we assume to be independent of ω, γ is the nonlinear parameter of the fiber, and P is the pump peak power. The JSI of a source can be defined by

$$|f(\omega_s, \omega_i)|^2 = \left| \int d\omega_p \alpha(\omega_p) \alpha(\omega_s + \omega_i - \omega_p) \phi(\omega_s, \omega_i) \right|^2, \tag{3.4}$$

where $\alpha(\omega)$ is the pump spectral amplitude and $\phi(\omega_s, \omega_i)$ is the phasematching function defined in Eq. 3.1. The bi-photon wavefunction, also known as the JSA can be defined by [55]

$$|\Psi_{s,i}\rangle = \iint d\omega_s d\omega_i f(\omega_s, \omega_i) \, |\omega_s\rangle \, |\omega_i\rangle \,, \tag{3.5}$$

where $f(\omega_s, \omega_i)$ is defined in Equation 3.4. Since it is not phase sensitive, the JSI is much easier to measure than the JSA, and a variety of approaches have been demonstrated for JSI measurement. Recently however, at least one approach for the more difficult phase-sensitive JSA measurement has been demonstrated [55]. In the remainder of this chapter, we outline the main approaches used for JSI measurements. Additionally, we describe one technique for JSA measurement, and two alternatives to full joint spectral measurements, when only photon purity is of interest.

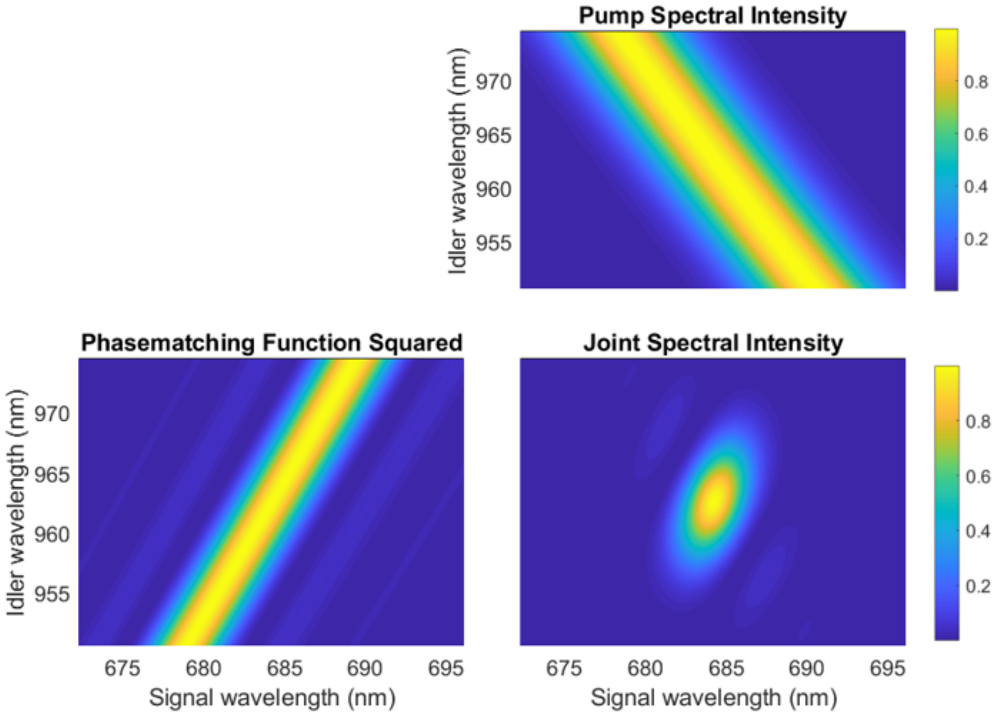

FIGURE 3.1: Example showing how the phasematching function and pump spectrum combine to produce the JSI. This JSI is modelled for a 2.5 cm bow-tie style fiber made from fused silica with a birefringence of 3.64×10^{-4}, with a pump centered at 800 nm and a bandwidth of 6 nm.

3.2 Spectrally resolved coincidence counting with monochromators

Historically, the most common method for measuring the JSI of a photon pair source involved spectrally resolved coincidence counting of single photons. In this method, the JSI is built up pixel by pixel. Using two frequency-selective single photon detectors, coincidence measurements are made between a given idler spectral mode and a given signal frequency mode. The number of coincidences detected per unit time corresponds

to the intensity of that particular pixel. Usually, scanning monochromators are used to provide the spectral resolution, as described in [53, 56].

The scanning monochromator approach has some limitations on its speed and resolution largely due to low photon count rates. Only one pixel is measured at a time, so the vast majority of photon pairs created during any given measurement period are discarded since they do not fall into that pixel. Additionally, in this type of measurement one is limited by the low rate of pair generation necessary. While in principle, the pump power can be increased to produce photon pairs at a higher rate, a higher pump power also increases the probability of generating more than one photon pair per pump pulse. This would introduce unwanted errors in the form of false coincidences (photons created in the same pump pulse, but from different photon pairs). Thus the scanning nature of the measurement, coupled with the modest quantum efficiency of single photon detectors and the low rate of pair generation lead to measurement times of hours or longer [53, 56]. In turn, these low light levels and long measurement times limit the feasible resolution obtainable through this approach.

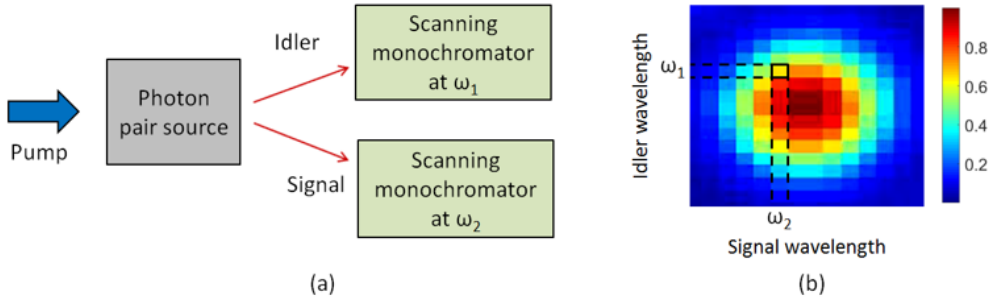

FIGURE 3.2: (a) Simplified sketch of the components in a JSI measurement involving scanning monochrometers. (b) Illustration of how this type of measurement is performed pixel by pixel.

3.3 Dispersive fibers and time-resolved coincidence counting

Another approach to JSI measurement also involves spectrally resolved coincidence counting. However in this case, the signal and idler photons are mapped from the frequency domain to the time domain and their arrival times are used to determine their spectral mode [57]. After the photon pairs are generated, the signal and idler are both sent through some material with significant chromatic Group Delay Dispersion (GDD). This ensures that the photons will exit the material after a delay that depends on their colour. The photons are then detected using single photon detectors with high timing resolution. Then coincidences coming from photons generated from the same pump

pulse can be examined, using the exact arrival times of the signal and idler photons to map back to the frequency domain. To provide the level of GDD necessary, approaches have been demonstrated using kilometers of optical fiber [57], and more recently with chirped fiber bragg gratings (FBGs) [58].

The time-resolved approach has one significant advantage over the scanning monochrometer approach: it can measure all frequency modes at any given time, so photon pairs are not wasted. Measurement times, on the scale of 5 minutes [58], have been demonstrated. However, this approach is still limited by the low rate of photon pair creation in the source. As the resolution of the measurement is increased, a fixed rate of photon pairs is spread over more and more pixels. Additionally, the resolution is usually increased by using a longer optical fiber; this introduces additional loss, particularly with wavelengths outside the low-loss telecom bands (around 1550 nm). This negatively affects the Signal to Noise Ratio (SNR), requiring longer measurement times. Chirped FBGs can also be used to improve resolution, however, writing very broadband gratings can be challenging. These gratings must be designed for a specified wavelength, making them less flexible as a measurement tool.

Single photon detectors currently suffer from timing jitter, where the timing of the detector output has some deviation from the timing of the detector input. The timing jitter limits the resolution with which the frequency-time mapping can be performed, and thus the overall resolution of the measurement [53]. The fastest single photon detectors are expensive, and even they have non-negligible jitter.

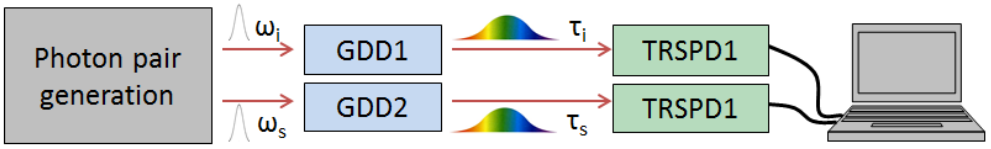

FIGURE 3.3: A block diagram demonstrating the principle of operation behind time-resolved coincidence counting JSI measurements. After creation, the idler and signal photons travel through a material with high group delay dispersion (GDD). This GDD maps the frequency of each photon (ω_i, ω_s) to a time delay (τ_i, τ_s) relative to a trigger from the pump. The photons are then collected using time resolved single photon detectors (TRSPD), which send the arrival times to a computer. The timing information is then mapped back to the frequency domain to create the JSI.

3.4 Fourier transform spectroscopy

A different approach to measuring the joint spectrum of a photon pair source makes use of 2 dimensional Fourier spectroscopy [53]. In the 1 dimension case, Fourier spectroscopy uses a time-domain signal collected from an interferometer with a variable path length

in one arm. As the path length of one interferometer arm is varied, the light intensity at the detector will change. Thus a time-domain signal can be collected as a function of the optical path diffference in the interferometer. Using a Fourier Transform, this time-domain signal can be used to extract the spectrum of the input light [59].

The following mathematical description is developed in [59]. For a single frequency ν, the light intensity at the detector is shown in Eq. 3.6

$$G(\tau) = g(\nu) + g(\nu)cos(2\pi\nu\tau), \tag{3.6}$$

where τ is the optical path difference (in units of time) in the interferometer arms and $G(\tau)$ is the intensity at the detector.

In Eq. 3.6 the $g(\nu)$ term is independent of τ, so it is ignored. To get the inteferogram signal ($F(\tau)$), which is the variable portion of the signal measured by the detector, one has to integrate over all spectral components contained in the input signal

$$F(\tau) = \int_0^\infty g(\nu)cos(2\pi\nu\tau)d(\nu). \tag{3.7}$$

Then a Fourier Transform can be applied to extract the input spectrum

$$g(\nu) = 4\int_0^\infty F(\tau)cos(2\pi\nu\tau)d\tau. \tag{3.8}$$

The maximum resolution obtainable using this approach depends on the maximum optical delay available in the interferometer. For an interferometer which can be varied from $-\tau_m < 0 < \tau_m$ then the maximum resolution possible is

$$\Delta\nu = 1/2\tau_m. \tag{3.9}$$

A 1-dimensional Fourier Transform spectroscopy measurement can be used to measure the spectrum of either the signal or idler on its own. For a joint spectral measurement, a 2-dimensional version of Fourier Spectroscopy is needed. Interferometers are set up in both the signal and idler arms and are varied independently. Coincidences are measured between the signal and idler detectors to build up a time-domain function ($I(\tau_s, \tau_i)$) dependent on both τ_s and τ_i, the optical path delay in the signal and idler arms respectively. Then a 2-dimensional Fourier Transform can be used to extract the joint spectral information [53].

This approach has been successfully experimentally demonstrated, with a total measurement time on the order of 12 minutes and an SNR of approximately 47 [53].

3.5 Stimulated emission tomography

More recently, a JSI measurement technique based on stimulated emission, rather than spontaneous emission, was theorized and demonstrated [56, 60, 61]. This technique is referred to as stimulated emission tomography (SET) [60]. The JSI is built up by scanning a narrow bandwidth seed beam through the bandwidth of one of the two output modes. This seed drives the nonlinear process in the stimulated regime (i.e. stimulated FWM or DFG, rather than SFWM, or SPDC). The spectrum of the other output mode is measured for each seed wavelength and these spectral slices can be pieced together to generate the entire JSI.

Unlike the coincidence counting approaches, SET is not limited by the rate of spontaneous photon pair creation. The seeding drastically increases the number of photon pairs, allowing for a much faster measurement, superior resolution, and better SNR. Due to the increased resolution and SNR, JSI features not discernable in a coincidence counting approach have been seen using an SET based measurement [56]. High resolution JSI have been recorded on the scale of a few minutes, as demonstrated in [61].

Equation 3.10 [60] demonstrates the enhancement factor provided by seeding the process:

$$\frac{\langle b_k^\dagger b_k \rangle_{stim}}{\langle b_k^\dagger b_k b_{k'}^\dagger b_{k'} \rangle} \approx |B_{k'}|^2, \tag{3.10}$$

where $b^\dagger, b$ represent creation and annihilation operators, and k and k' represent the wave vectors of the generated and seed modes respectively. The term $|B_{k'}|^2$ is the average number of coherent photons in the seed pulse, which approximately equal to the enhancement factor in the number of photon pairs produced. The approximate equality comes from two factors: firstly, in Eq. 3.10 the spontaneous term is neglected, and secondly, the shape of the seed pulse is neglected (a constant energy density in the seed pulse is assumed).

This technique requires that $k \neq k'$ since the two wavevectors must be separable after generation. Therefore the signal and idler must have different energies.

Excellent examples of the difference in resolution and SNR of SET as compared to coincidence counting measurements can be found in [53, 56, 61]. Direct comparisons

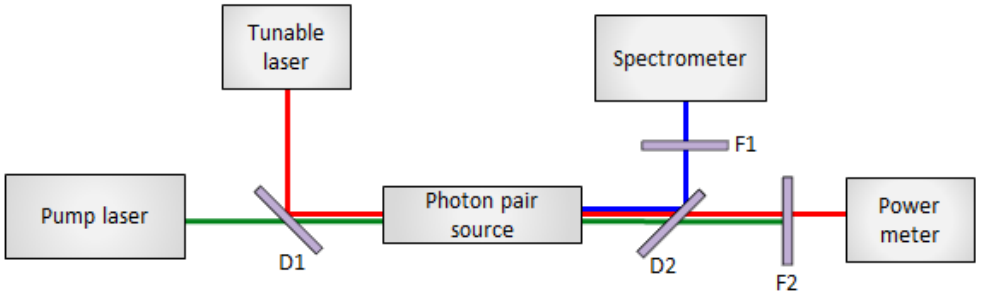

FIGURE 3.4: Block diagram showing the experimental setup for SET. The green line is used to show the pump path, the red line to show the CW seed beam, and the blue line to show the generated signal beam.

demonstrate how SET can reveal features not measurable in coincidence counting techniques.

3.5.1 Phase sensitive measurements

In 2016, the SET technique was extended to demonstrate phase-sensitive JSA measurements [55]. It was demonstrated that information not obtainable through the JSI could be measured using this phase sensitive technique. In particular, using a chirped pump pulse, compared to a transform-limited pump pulse, showed changes in the measured JSA, but not the JSI.

In this technique, a pump and seed pulse are used, as in SET, but additionally a reference pulse is used at the stimulated emission frequencies. For example, if the process is seeded at the signal wavelength, a pulse is needed at the idler frequency to act as a phase reference. The stimulated emission frequencies are interfered with the reference pulse at an Optical Spectrum Analyzer to provide phase-sensitive detection. For each slice, the measurement was performed 4 times, each time with a different phase applied to the seed pulse (0, $\pi/2, \pi, 3\pi/2$). Looking at the difference between pairs of measurements allowed the authors to extract the real and imaginary components of the JSA.

3.5.2 Characterization of entangled photon pairs

A really interesting application of Stimulated Emission Tomography is its application exploring quantum correlations, something usually performed through quantum state tomography (QST) [62]. In this context, QST involves the reconstruction of the quantum state of a system by analyzing a variety of measurements of the system projected onto different states. Accordingly, it can be very resource intensive. For example, characterizing a photon pair in the polarization degree of freedom requires 16 separate

measurements [63]. Traditionally, QST is performed by looking at coincidences between single photons, leading to long measurement times. Similarly to joint spectral measurements, SET provides a path to much faster measurements compared to conventional QST due to the significant increase in light, as shown in [62, 63].

Perhaps of even greater interest, SET has allowed groups to probe deeper than conventional QST would allow. Since SET provides a considerable improvement in measurement times, it allows for measurement of correlations across more than one degree of freedom; these correlations require too many measurements to study feasibly using conventional QST.

For example, in [62], the authors studies correlations between the polarization and energy degrees of freedom in polarization-entangled photon pairs. This helps with understanding the degradation of polarization-entangled photon pairs due to undesirable spectral correlations. In [63], the use of SET allowed the authors to examine correlations between the polarization degree of freedom and emission angle. Conversely, the emission angle is a degree of freedom which conventional QST averages over.

Clearly, SET provides a way to extract additional information about quantum systems compared to conventional QST based on single photon coincidences. Moving forward, this will allow for both better characterization and better control of quantum correlations in entangled systems.

3.6 Conclusion

Spectral correlations are an important aspect of photon pair sources which needs to be measured and controlled. Particularly for heralded single photon sources, spectral correlations need to be kept to a minimum. Conversely, for some applications, such as frequency entangled photon pairs, strong spectral correlations are necessary. This chapter has summarized a variety of techniques used for measuring the joint spectral intensity (JSI) of photon pair sources. The next chapter will build upon the concept of Stimulated Emission Tomography (SET), one of the approaches discussed in this chapter, and demonstrate an extension of SET which allows for joint spectral measurements on the few-second timescale.

Chapter 4

Joint Spectral Intensity Measurement using Broadband Light

This chapter is based on the following publication:

Jennifer Erskine, Duncan England, Connor Kupchak, and Benjamin Sussman. Real-time spectral characterization of a photon pair source using a chirped supercontinuum seed. *Opt. Lett.*, 43(4):907–910, Feb 2018

This chapter assumes a basic knowledge of Stimulated Emission Tomography, which is discussed in Chapter 3.

4.1 Introduction

Photon pair sources have wide ranging applications in a variety of quantum photonic experiments and protocols, as discussed in Chapter 2. Many of these protocols require well controlled spectral correlations between the two output photons. However, measuring the joint spectral properties of photon pair sources has historically been a challenging and time-consuming task. Here, we present an approach for the real-time measurement of the joint spectral properties of a fiber-based four wave mixing source.

The spectral characterization of a photon pair source is usually represented through its joint spectral intensity (JSI). In the past, measurements were based on spectrally resolved coincidence counting of single photons, generally using two monochromators [56]. Due to the probabilistic nature of the photon pair generation and the scanning nature

of the measurement, this type of measurement has resulted in limited resolution and long measurement times. More recently, other approaches to the measurement of joint spectral intensities have been demonstrated, including the use of time resolved single photon detectors with chirped fiber bragg gratings [58] or long spools of fiber [57], and Stimulated Emission Tomography (SET) [60, 61], as discussed in Chapter 3. Both of these methods have offered significant improvements in measurement times, requiring as little as several minutes [58, 61].

Previous demonstrations of the stimulated emission technique made use of a tunable, continuous wave (CW) laser [56, 61] or a broadband (30 nm) pump and a dynamically tunable filter [55] as the seed beam. Here, we demonstrate an extension of the stimulated emission approach, studying four wave mixing in a polarization maintaining fiber (PMF) [54]. For the seed beam, we make use of white light generated from the pump through supercontinuum generation in a photonic crystal fiber (PCF). The supercontinuum is heavily chirped such that only a narrow bandwidth is temporally overlapped with the pump, and the seed wavelength is tuned by changing the delay between pump and seed. This technique leverages recent developments in PCF technology which have allowed for efficient supercontinuum generation at nJ pulse energies in affordable, commercially available fibers. This allows seeding over a large bandwidth without the need for a separate seed laser, greatly reducing experimental overhead. Furthermore, this approach offers a significant improvement in speed, as the measurement speed is limited only by the movements of an optical delay line. Measurement durations have ranged from 5 s up to 30 s depending on the desired resolution and data acquisition software used. Additional benefits of this approach include flexible resolution and large measurement bandwidth.

Lastly, a significant advantage of using SET, regardless of the type of seed beam used, is the option to work with a bright beam. With SET, the photon pair source emits a bright beam at both the signal and idler energies with the same spatial and polarization modes, as well as similar temporal properties as any photon pairs produced in that source. It is significantly easier to work with bright beams than with single-photon level beams, making the alignment of any components after the photon pair source much easier. This is discussed further in Chapter 6.

4.2 Experimental setup

Figure 4.1 shows the experimental apparatus. A Ti:Sapph laser generates pulses at 800 nm with a bandwidth of 12 nm and a repetition rate of 80 MHz. The beam is split on a polarizing beam splitter (PBS) and one part of the beam is coupled into a PCF

(FemtoWHITE CARS from NKT Photonics) where supercontinuum generation occurs. Use of a prism compressor ensures that the pump is transform limited at the input to the PCF, increasing the stability and bandwidth of the white light. The output from the PCF contains light from 650 nm to over 1000 nm. The white light is coupled into 8 m of single mode fiber (SMF), chirping the pulse by approximately 380 fs/nm. A 900 nm long-pass filter removes any light at the signal wavelength. A total of 30 mW of pump power is sent to the PCF which has a coupling efficiency of approximately 50%. After spectral and polarization filtering only 1.5 mW of power, spread from 900 nm to 1000 nm, is used to seed the FWM process, which is driven by 10 mW of pump power.

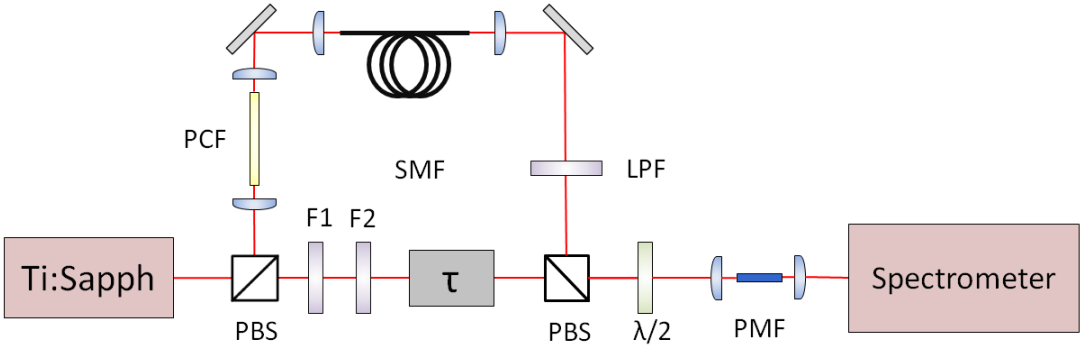

FIGURE 4.1: Schematic of the experimental setup. Ti:Sapph, Ti:Sapphire femtosecond oscillator at 800 nm, 80 MHz repetition rate, 80 fs pulse duration; PBS, polarizing beam splitter; $\lambda/2$, half wave plate; PMF, polarization maintaining fiber; SMF, single mode fiber; τ, time delay; F1 and F2, bandpass filters to shape the pump spectrum; PCF: photonic crystal fiber; LPF, 900 nm long pass filter.

The remaining pump passes through two angle-tuned bandpass filters (F1 and F2 in Fig. 4.1) to achieve the desired bandwidth before passing through a delay line τ. The pump then recombines with the seed light on a PBS. The two beams are coupled into a bow-tie style 2.5 cm long PMF (Fibercore HB800) with the pump polarized along the slow axis and the seed light along the fast axis. Due to the chirp in the seed beam and the differences in temporal duration between the two beams, the short pump only overlaps with a narrow spectral component of the seed beam, stimulating the four wave mixing process. The spectral component overlapped with the pump is adjusted by changing the pump delay, as shown in Fig. 4.2.

FIGURE 4.2: Schematic showing how the pump pulse (red pulse) interacts with a specific spectral component of the chirped seed (multicoloured pulse) depending on the delay between them.

Stimulated four wave mixing occurs in the PMF, generating light at both the seed (idler) wavelength and its corresponding signal wavelength. Compared to the spontaneous case, the seeding enhances the probability of generating a photon pair by a factor approximately equal to the number of photons in the seed beam, as discussed in Eq. 3.10. The signal and idler beams are separated on a dichroic mirror, and the signal is measured with a spectrometer (example spectrum shown in Fig. 4.3). This generates a slice of the joint spectrum corresponding to that particular seed wavelength. The seed is scanned through the idler bandwidth and the slices are stacked together to produce the full joint spectrum. Each slice is normalized based on the seed intensity for that slice.

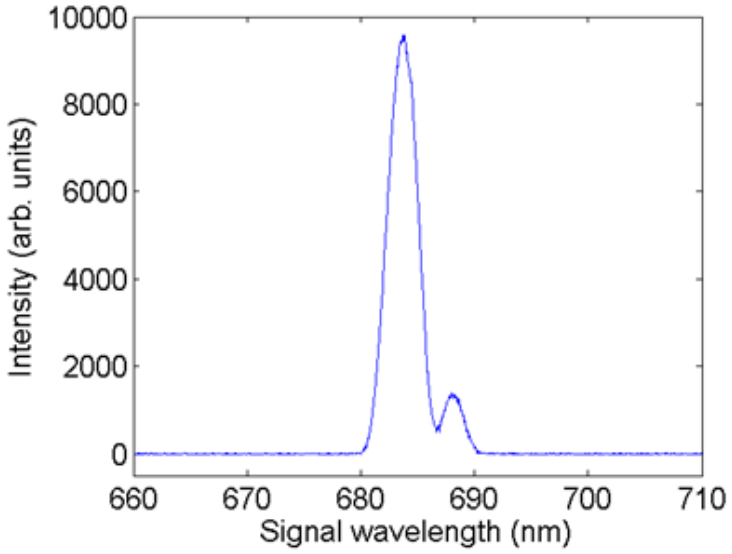

FIGURE 4.3: Example of a signal spectrum recorded during a JSI measurement using a 50 ms integration time.

4.2.1 Photon pair source

We also characterized the spontaneous operation of the photon pair source. Descriptions and theoretical background on the second order correlation functions measured here can be found in Section 2.4.

First, we measure the rate of photon detection events for both the signal and idler photons, as well as the rate of signal/idler coincidences as a function of pump power using a 2 ns coincidence window, as shown in Fig. 4.4.

To look at correlations in the photon number degree of freedom between the signal and idler, we measure the second order cross-correlation ($g^{(2)}_{s,i}(0)$) function as a function of pump power, as shown in Figure 4.5. For a source based on four wave mixing, the probability of generating a photon pair is proportional to the square of the pump

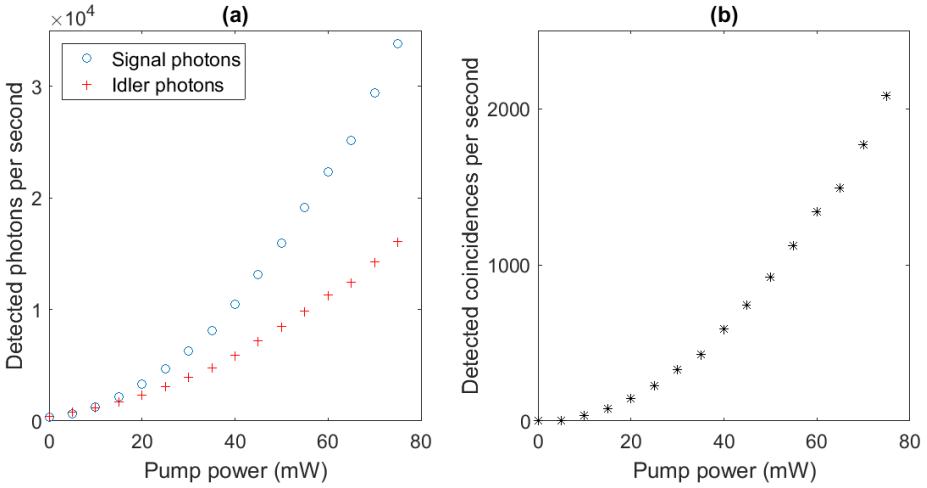

FIGURE 4.4: (a) rate of detected signal and idler photons generated in the photon pair source. (b) rate of coincidences between the signal and idler photons. With the scales used in this figure, Poissonian errorbars are too small to clearly seen, and are thus not shown.

power, so the cross-correlation for an ideal photon pair source would scale with $\sim 1/I_p^2$. At high powers, Figure 4.5 shows a clear, nonlinear decrease in the crosscorrelation as pump power increases, as expected. At low powers, the rollover and subsequent decrease in the cross-correlation with decreasing pump power is the result of background light and dark counts on the detector. For all powers measured, the $g^{(2)}_{s,i}(0)$ had a value of several hundred or more, showing strong photon number correlation between the signal and idler.

To help quantify the single photon nature of the signal photons, we measure the heralded autocorrelation as a function of pump power (Figure 4.6). Here, we use a detection set-up as outlined in Fig. 2.5. While a perfect heralded single photon source would have a $g^{(2)}_{s,s}(0)$ of 0, noise and multi-photon pair emissions inherent in real systems increase this value. The heralded autocorrelation measured varies from approximately $(2-8)\times 10^{-3}$, showing the photon source is of high quality. Figure 4.6 shows a definite increase in the $g^{(2)}_{s,s}(0)$ with pump power, as expected, since higher pump power leads to a higher probability of multi-photon pair emission.

Lastly, the unheralded autocorrelation for a variety of pump powers is shown in Fig. 4.7. The average value is 1.30+/-0.02, indicating a purity of 0.3, or a K value of 3.33, and no major dependence on pump power is observed. The low purity is indicative of significant spectral correlations between the signal and idler. This is consistent with expectations, since the pump bandwidth used (9 nm) was too large to produce a largely uncorrelated joint spectrum and no effort was made to spectrally filter the peripheral lobes in the joint spectrum. A measurement of this joint spectrum can be found in Ch. 6, Fig. 6.6.

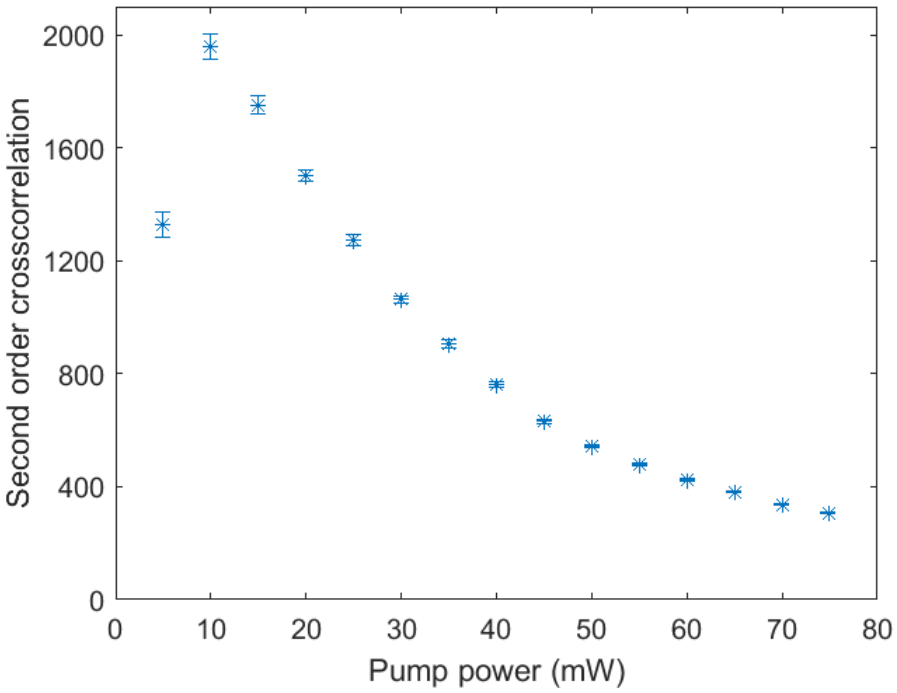

FIGURE 4.5: Measurement of the second order crosscorrelation function $g^{(2)}_{s,i}(0)$ as a function of pump power. Poissonian errorbars are shown.

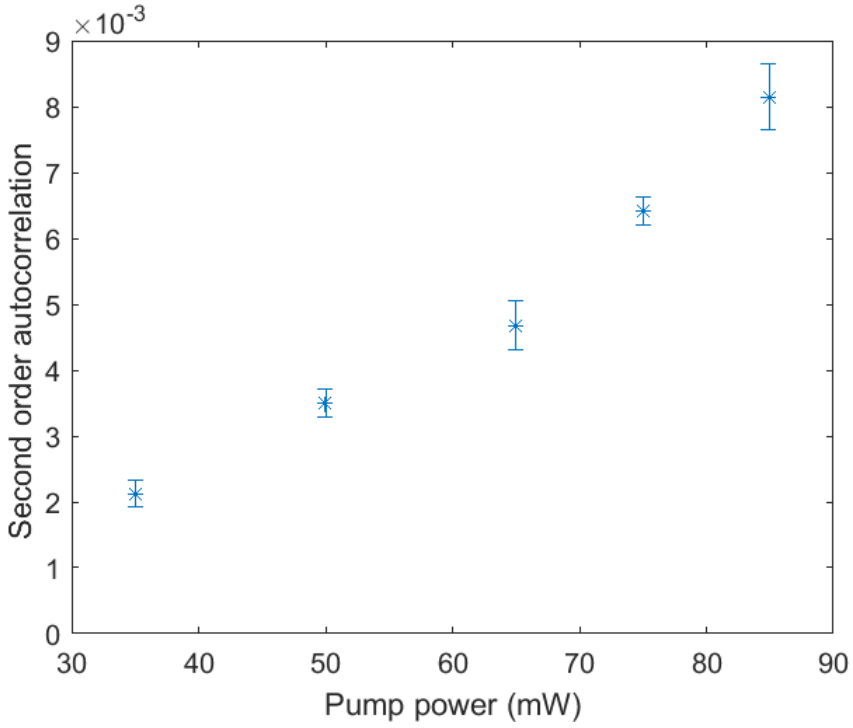

FIGURE 4.6: Measurement of the heralded second order autocorrelation function $g^{(2)}_{s,s}(0)$ as a function of pump power. Poissonian errorbars are shown.

Due to the length of the fiber, there will also be some temporal correlations which also decrease the source purity.

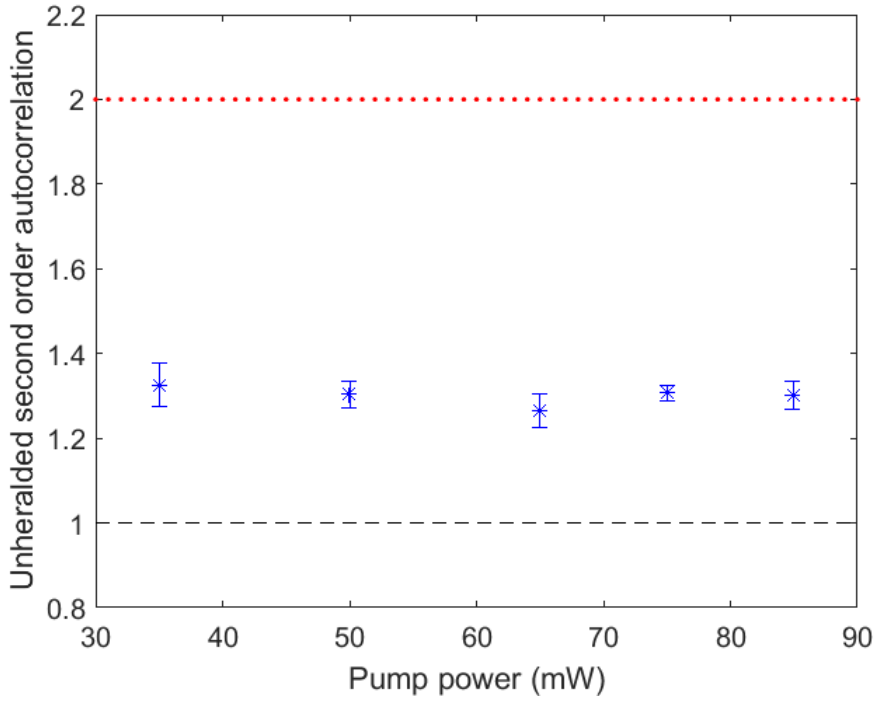

FIGURE 4.7: Measurement of the unheralded second order autocorrelation function (blue points) as a function of pump power. Poissonian errorbars are shown. A black line indicates a value of 1 (autocorrelation of a highly mixed state) and a red line shows a value of 2 (autocorrelation of a perfectly pure state).

4.2.2 Supercontinuum generation

Laser light, which has a high level of coherence and limited spectral bandwidth, can be converted to a much broader spectral range through a combination of highly nonlinear optical processes; this is called supercontinuum generation. The resulting spectrum is usually very broad, with a low degree of temporal coherence. There are several nonlinear optical effects which can contribute to supercontinuum generation, including self-phase modulation, four-wave mixing, and Raman scattering [65]. In some cases, soliton fission and other soliton dynamics can play an important role. However, in general the dynamics behind supercontinuum generation are very complex, with multiple effects occuring simultaneously.

Supercontinuum generation has been demonstrated in a variety of media, including bulk glass and various kinds of optical fibers. Photonic crystal fibers are particularly interesting, as their dispersion properties can be engineered to achieve particular types of nonlinear interactions. Even at nJ level input pulse powers, spectra containing several

hundred nanometers of bandwidth can be generated through supercontinuum generation [66].

To generate the broadband seed needed in this JSI measurement technique, the NKT Photonics femtoWHITE CARS PCF was used. The PCF was pumped with pulses centered at 800 nm, with 80 fs duration, and 30 mW (0.375 nJ/pulse) pump power. An example of the broadband pulse used for seeding is shown in Figure 4.8.

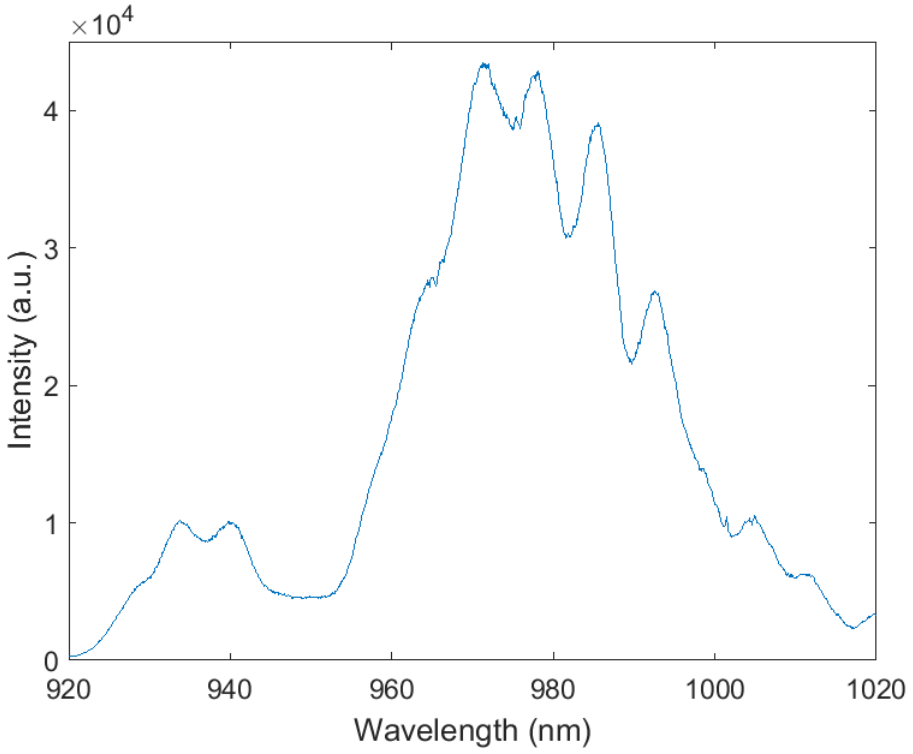

FIGURE 4.8: Example of seed spectrum generated through supercontinuum generation.

4.2.3 Idler calibration

For added clarity in this section, we will refer to the light generated through supercontinuum generation as the broadband seed, and the portion of this light which is temporally overalapped with the pump as the instantaneous seed. A calibration step is needed to determine the instantaneous seed wavelength as a function of pump delay. This is performed by recording the broadband seed spectrum with the pump on and off and subtracting the two to return a differential spectrum. Initially, it was expected that there would be a spike at the instantaneous seed wavelength. In this four-wave mixing process, two pump photons are annihilated and both a signal and idler photon are created. Thus it was expected that at the instantaneous seed wavelength, amplification would occur due to the idler photons created.

However, the observed trend was substantially different, as shown in Figure 4.9. Through the optical Kerr effect, the strong pump pulse induces an intensity dependent change in the refractive index of the PM fiber and the weaker seed beam sees this changing refractive index. As the pump walks through the seed this causes both an up-chirp and a down-chirp, resulting in some energy getting pushed from the central instantaneous seed wavelength to the red and blue side. No net energy is lost or stored in the medium, and we note that the broadband seed is too weak to affect itself or the pump through self or cross-phase modulation. This interaction with the pump results in the spectrum of the instantaeous seed being broadened slightly. A $\sim 1\%$ dip can be seen in the differential spectrum at the instantaneous seed wavelength, with corresponding increases on either side of the dip [67].

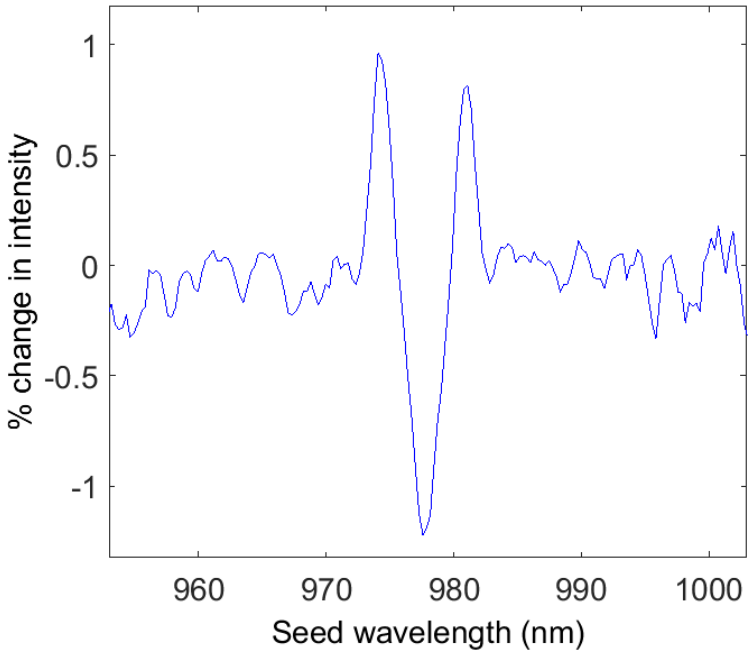

FIGURE 4.9: Example of a coherent artifact in the seed wavelength. The coherent artifact is found by taking the difference between the seed spectra recorded with the pump on and off. The dip corresponds to the seed wavelength best temporally overlapped with the pump.

To calibrate the instantaneous seed with respect to the pump delay, we measure the position of the dip as a function of delay, making several measurements over the range of seed wavelengths used. A linear fit is performed for the set of measurements.

4.2.4 Idler normalization

In the regime studied, the intensity of the signal spectrum depends linearly on the intensity of the seed, as shown in Fig. 4.10. This measurement is performed for a fixed seed wavelength of 965 nm. This linear relationship confirms that the generation of photon pairs is proportional to the number of seed photons, as expected 3.10. It also confirms that normalizing each JSI slice by its instantaneous seed intensity is appropriate.

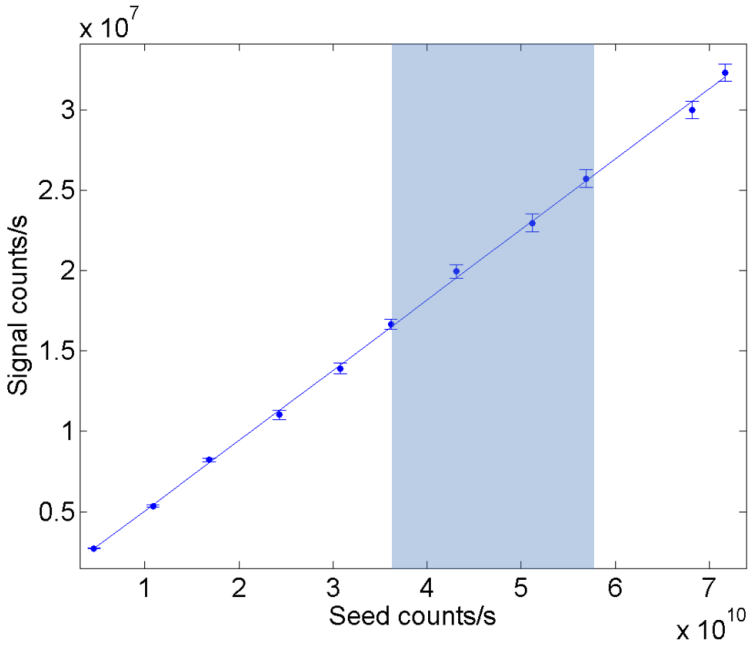

FIGURE 4.10: Correlation between seed intensity and signal intensity. A least squares linear fit is shown and the error bars for the signal count rate show an uncertainty of two standard deviations, determined from a set of 20 measurements taken at each point. The shaded region indicates the range of seed intensities used during joint spectra measurements.

4.2.5 Seeding enhancement factor

We compare the number of photons generated through stimulated four wave mixing compared to the spontaneous process to estimate the enhancement factor obtained by seeding the process. Using neutral density (ND) filters calibrated at the appropriate wavelength, we measure the number of counts per second at a given wavelength registered on a spectrometer for each process. For the seed intensity used in this demonstration, we measure that the total enhancement factor is on the order of 10^5. As discussed in Ch. 3, this should be approximately equal to the number of coherent photons in the instantaneous seed. Based on the power of the seed beam, the seed spectrum, and the walk-off within the PMF, we calculate the number of photons in the instantaneous seed to be on the order of 10^5, which agrees well with the measured enhancement factor.

4.3 Results

Three measured joint spectra are shown in Fig. 4.11 along with their theoretical counterparts. Here we demonstrate changing the pump bandwidth to tune the joint spectra to correlated, largely uncorrelated, and anti-correlated states.

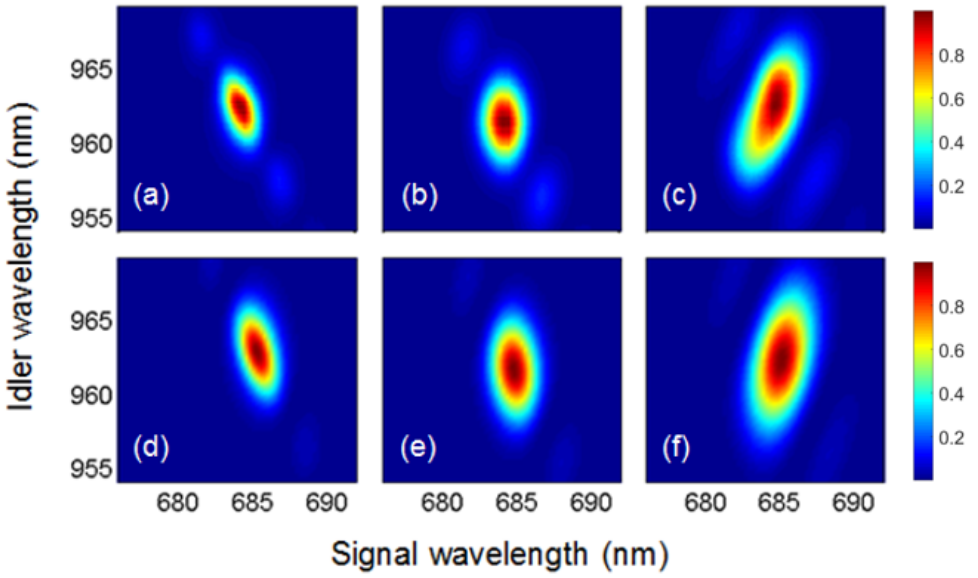

FIGURE 4.11: Measured (a)-(c) and theoretical (d)-(f) joint spectra for a 2.5 cm birefringent fiber. Pump bandwidth was varied between (a,d) 2 nm, (b,e) 4 nm, and (c,f) 8 nm to show different types of spectral correlations. All pump bandwidths are quoted as intensity full width at half maximum (FWHM).

The theoretical joint spectra were generated numerically by calculating the product of the pump envelope $\alpha(\omega_p)$ and the phase matching function $\phi(\omega_s, \omega_i)$, as outlined in 3.4 in Chapter 3. The fiber tested has a birefringence of $\Delta n = 3.6 \times 10^{-4}$. The refractive index $n(\omega)$ is approximated by the Sellmeier equation for fused silica, with a constant offset of 0.0088 (based on discussion with the manufacturer) to account for the addition of germanium dopant in the core of the fiber.

These theoretical calculations do not take in to account several factors including waveguide dispersion, chirp, walk-off, and multimode propagation in the PMF as well as competing nonlinear processes such as cross-phase modulation and two-photon absorption, which are challenging to model. These factors lead to small discrepancies between the measured (a-c) and calculated (d-f) JSIs in Fig. 4.11 and highlight the importance of performing these measurements.

To further verify the validity of this technique, a fixed idler wavelength was selected and a comparison was made between spectral slices obtained by studying the spontaneous and stimulated processes, as shown in Fig. 4.12. In the spontaneous case, two

monochromators with outputs coupled to single photon detectors were used for spectrally resolved coincidence counting. The idler monochromator was left fixed at 964 nm and the signal monochrometer was scanned through a range of wavelengths for several hours. The blue points in Fig. 4.12 show the rate of coincidences between the idler and signal monochrometers. In the stimulated case, a seed pulse at 964 nm was used, and the same signal monochromator was used to measure the spectrum of the stimulated signal. In this case, the signal monochrometer spent only a few seconds at each point, and used a much smaller step size. The solid line in Fig. 4.12 shows the rate of photons detected by the signal monochrometer when seeding is present.

Clearly, there is good agreement between the two measurement methods, supporting that the measurement of stimulated FWM can be appropriately used to measure the JSI of a photon pair source based on spontaneous FWM.

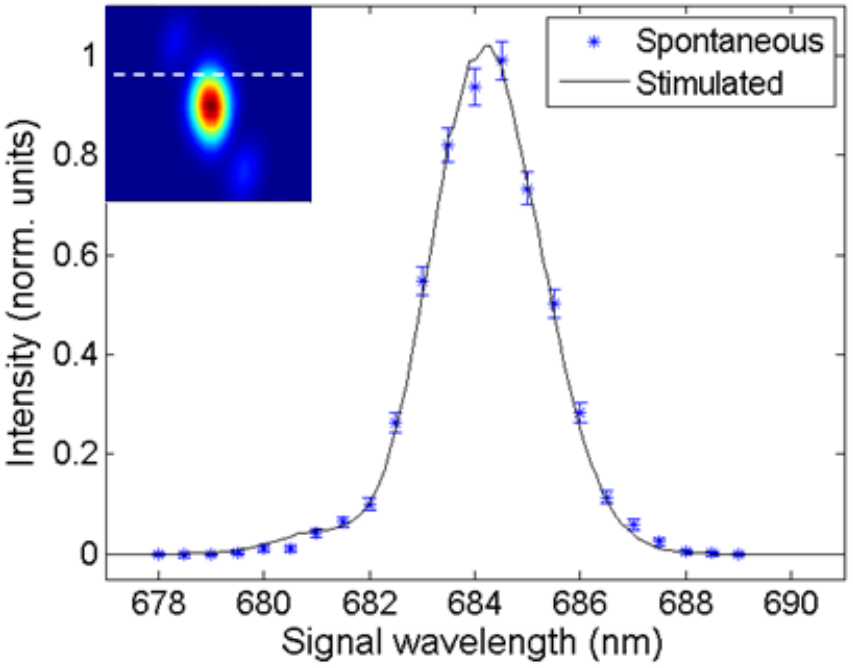

FIGURE 4.12: Comparison between spontaneous (points) and stimulated (solid line) cases for a fixed idler wavelength at a pump bandwidth of 4 nm. For the spontaneous case, Poissonian error bars are shown. Inset shows the location of the comparison in the overall joint spectrum.

4.3.1 Asymmetry

Based on the equations describing the JSI, as discussed in Chapter 3, there should be two axes of symmetry in the JSI. One comes from conservation of energy ($2\omega_p = \omega_i + \omega_s$) and the other from the phase matching condition ($2\omega_p(n(\omega_p) + \Delta n) = \omega_s n(\omega_s) + \omega_i n(\omega_i)$).

However, in early trials, significant asymmetry was observed in the measured JSIs, as seen in Fig. 4.13.

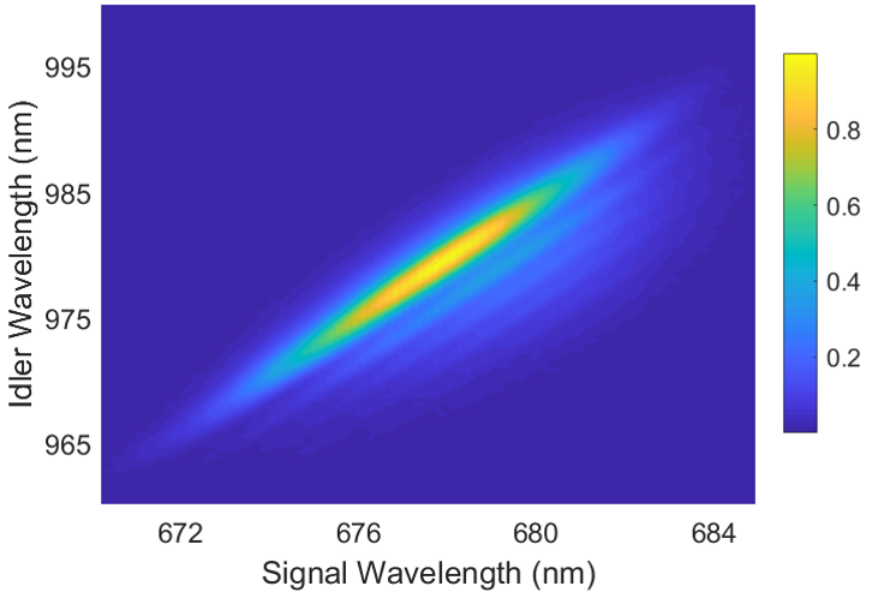

FIGURE 4.13: Measured JSI showing asymmetry in the sidelobes. Suspected cause of this asymmetry is stress on the fiber.

This asymmetry was unexpected and several possible explanations were considered. These included multimode behaviour in the birefringent fiber, a satellite pulse, nonlinear effects such as cross-phase modulation (XPM) and self-phase modulation (SPM), stress on the fiber, soliton dynamics in the PCF, or effects related to walk-off within the fiber. As much as possible, these potential explanations were investigated in the hopes of either confirming or ruling them out.

The idea of satellite pulses was investigated by performing an autocorrelation of the pump just before it is coupled into the birefringent fiber. No satellite pulses were found in the pump during the autocorrelation. Unfortunately the seed beam was too weak for an autocorrelation, so a cross-correlation was performed by looking at Sum Frequency Generation (SFG) between the pump and seed. Again, no evidence of satellite pulses were detected.

To examine the possibility of multimode behaviour, the pump was tuned to the red such that the pump, idler, and signal wavelengths were all above the fiber cutoff wavelength. However, the asymmetry was still visible at these new wavelengths.

Cross phase modulation (XPM) and other nonlinear optical effects were also considered. As shown in [68], XPM can cause asymmetry in in fibers when there is walk-off between the pump and signal. In particular, a spectrum with lobes on one side only can result

when the pump and signal coincide at the fiber tip, and then the pump walks through the signal. To explore this possibility, power scans were performed where the pump and seed powers were varied independently. As shown in Fig. 4.14, changing the pump power had no significant effect on the spectrum of idler light created during stimulated FWM (at this time, the process was seeded using the signal mode).

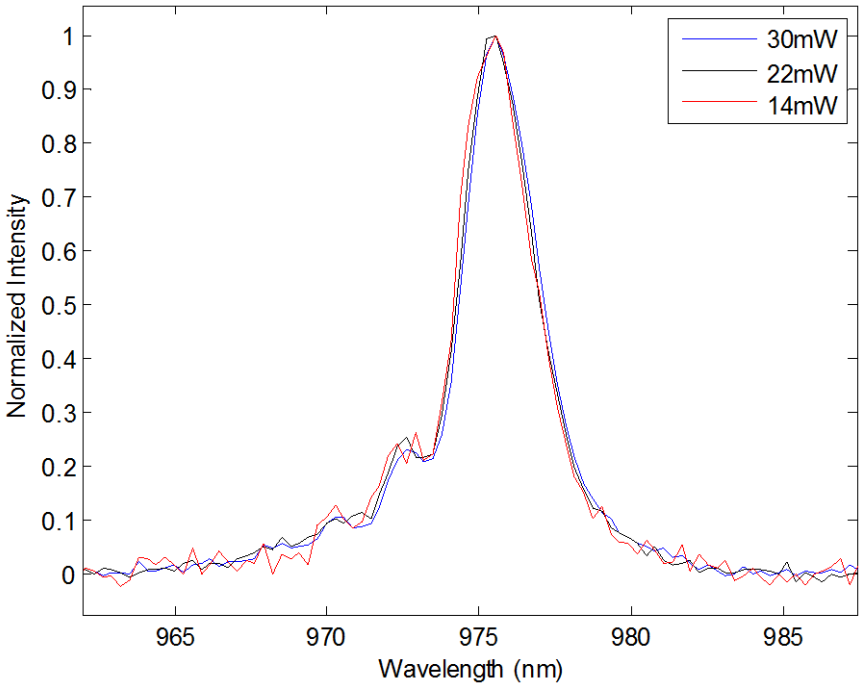

FIGURE 4.14: Spectra of stimulated FWM at three different pump powers. The seed wavelength and seed intensity were kept constant. No significant change is observed in the stimulated FWM spectrum, suggesting that the asymmetry observed is not dependent on the pump power.

Similarly, in Fig. 4.15, the asymmetry persists even at low intensities of the seed pulse. At low seed intensities, the spontaneous FWM spectrum becomes more visible. The spontaneous spectrum is not expected to show any asymmetry, since it is an integration over all signal frequencies. However, the presence and location of the asymmetric sidelobes is present in all seeded spectra. Since the asymmetry persists regardless of pump and probe power, this suggests that it is not likely the result of XPM or another nonlinear effect, since nonlinear effects are inherently intensity dependent.

Fig. 4.15 is also interesting because it shows the relative importance of the spontaneous and stimulated processes at various seed intensities. The spectrum of the spontaneous process is negligible at high seed intensities, but it contributes significantly to the overall idler spectrum at very low seed powers, as expected. Looking at the line corresponding to ND5 in Fig. 4.15, we see that the stimulated and spontaneous processes make comparable contributions to the idler spectrum. This is consistent with previous measurements indicating that the enhancement factor is of the order 10^5.

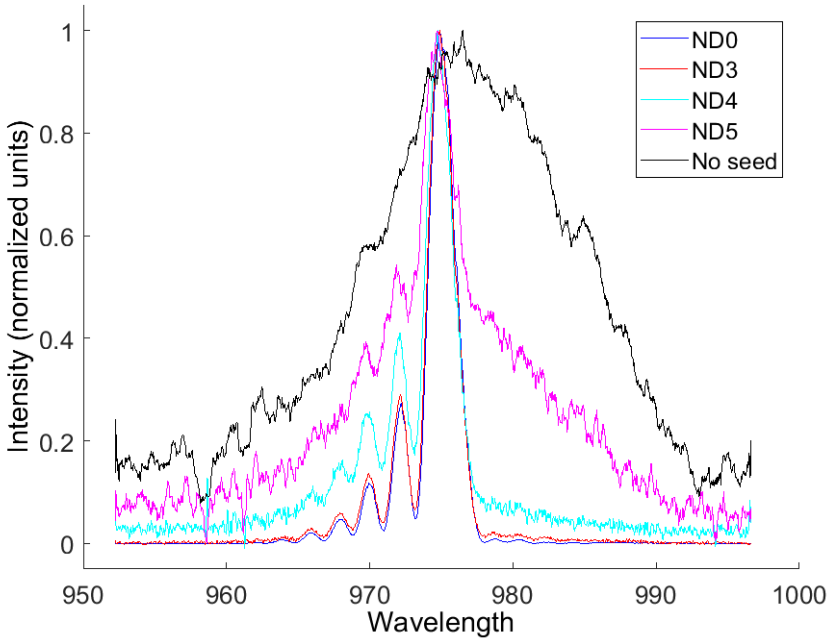

FIGURE 4.15: Spectra of stimulated FWM at five different seed powers. Neutral density (ND) filters of varying optical densities were used to attenuate the seed. For example in the legend, ND5 indicates that a neutral density filter of optical density 5 was used. The seed wavelength and pump intensity were kept constant. At low seed powers, the spectrum idler mode from spontaneous FWM is more prominent.

A different segment of the same fiber was tested and no asymmetry was observed. This suggests that the asymmetry was likely caused by something inherent in the first fiber, such as some sort of stress, perhaps induced by the jacket or FC connectors. Similar types of asymmetry were observed when fibers were deliberately stress (discussed in Chapter 5), which further supports this theory.

This example highlights the need for fast and reliable joint spectral measurements. Such a technique can quickly diagnose fibers with unusual or undesirable properties.

4.3.2 Speed

A major advantage of the approach outlined in this chapter is the speed of data acquisition. Measurements can be performed in 5-30 s depending on the desired resolution. This represents a significant improvement over other demonstrations of JSI measurement approaches which have shown measurement times on the order of 5 minutes [58, 61].

The speed depends on both the resolution desired and the spectrometer used. The two spectrometers used for data collection are the Ocean Optics USB2000+ and the Princeton Instruments Acton SP2300 spectrometer with ProEM CCD camera. The Princeton Instruments spectrometer has much higher resolution; however, the software

is slower than the Ocean Optics unit. Fig. 4.11 (subplots a-c) are representative of the quality of measurement obtainable with this spectrometer, and measurement times varied from 20-30 s depending on the range and resolution of the plot.

The Ocean Optics spectrometer offered a substantially lower resolution, but the software was much faster. Measurements could be made in as little as 5 s, as shown in 4.16. Depending on the size of the joint spectrum and the features of interest, this level of resolution is suitable for many applications.

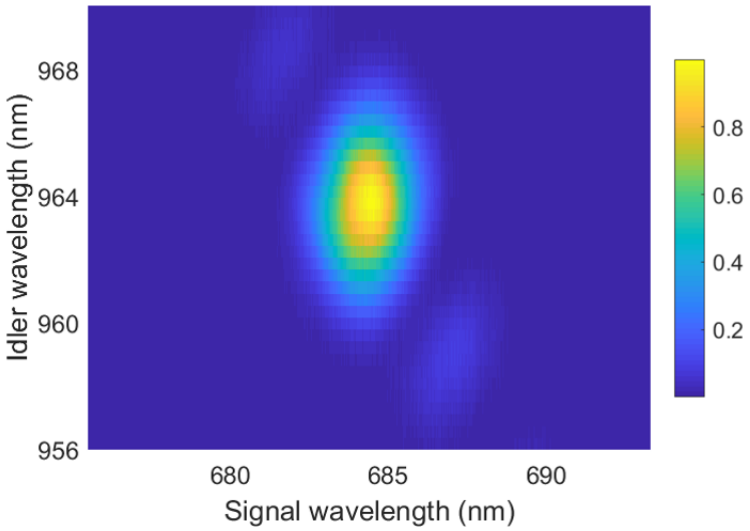

FIGURE 4.16: JSI measurement made in 5 s with a tabletop spectrometer (Ocean Optics USB2000+).

These few-second measurements are particularly interesting because open the door to real-time JSI measurements. One could imagine making adjustments such as tuning the pump bandwidth or adding spectral filters and monitoring the effects of those adjustments on the JSI in real time.

4.3.3 Resolution

The lower limits on the resolution of the JSI are given by the spectrometer resolution in the signal axis and the step size between seed wavelengths in the idler axis. For the plots shown in Fig. 4.11, those values are 0.13 nm and 0.05 nm respectively. However, in this approach we use a chirped, broadband pulse as the seed. This stimulates the interaction with an effective seed bandwidth defined by the range of seed frequencies temporally overlapped with the pump in the birefringent fiber. This effective seed bandwidth depends on three factors: the pump duration, the temporal walkoff between the pump and seed in the fiber, and the chirp on the seed pulse. The result of this effective

seed bandwidth (compared to a monochromatic seed) is a smoothing effect in the idler axis, reducing the resolution.

Here, the pump has a duration of 120-470 fs depending on the bandwidth tuning. The fiber has a length of $L = 2.5\,\text{cm}$ with a birefringence of 3.6×10^{-4}. With material dispersion and the birefringence (we assume waveguide dispersion is negligible), the walkoff between the pump centered at 800 nm and a seed centered at 965 nm is 320 fs over the length of the fiber. This can be calculated according to Equation 4.1

$$\tau_{walk-off} = \frac{L}{c}\Big(n_g(\omega_p) - n_g(\omega_i)\Big). \tag{4.1}$$

To model these effects, we represent the pump duration as a Gaussian filter and the walkoff as a moving average filter, combining the two through convolution. Accounting for both effects, the pump interacts with the a seed bandwidth covering a duration of 320-520 fs. As the seed beam is chirped to 380 fs/nm, this corresponds to an effective seed bandwidth of 0.84-1.4 nm.

To demonstrate the significance of this smoothing effect, we apply several moving average filters of different widths to a theoretical JSI cross-section, shown in Figure 4.17. In Figure 4.17, the red line (1 nm moving average) is a good approximationg of the experiment shown. In order to quantify the effect of the smoothing, we calculate the overlap integral between the smoothed and non-smoothed cross-sections, according to Eq. 4.2:

$$OI(f,g) = \frac{\left|\int f(x)g(x)dx\right|^2}{\int |f(x)|^2dx \int |g(x)|^2dx}. \tag{4.2}$$

Since the features of the JSI measured here are gradual on the scale of the effective seeding bandwidth, this method of seeding has little effect on the measurement. The overlap integrals for the three filters shown are all above 0.99, demonstrating good agreement with the original cross-section. For cases where sharp or narrow features are expected, this smoothing would have a larger impact on the measurement. To minimize the smoothing effect, the chirp on the seed pulse could be increased until the effective seeding bandwidth is small compared to the JSI features of interest. However, this comes at the expense of decreasing the spectral intensity of the seed and correspondingly decreasing the signal to noise ratio (SNR).

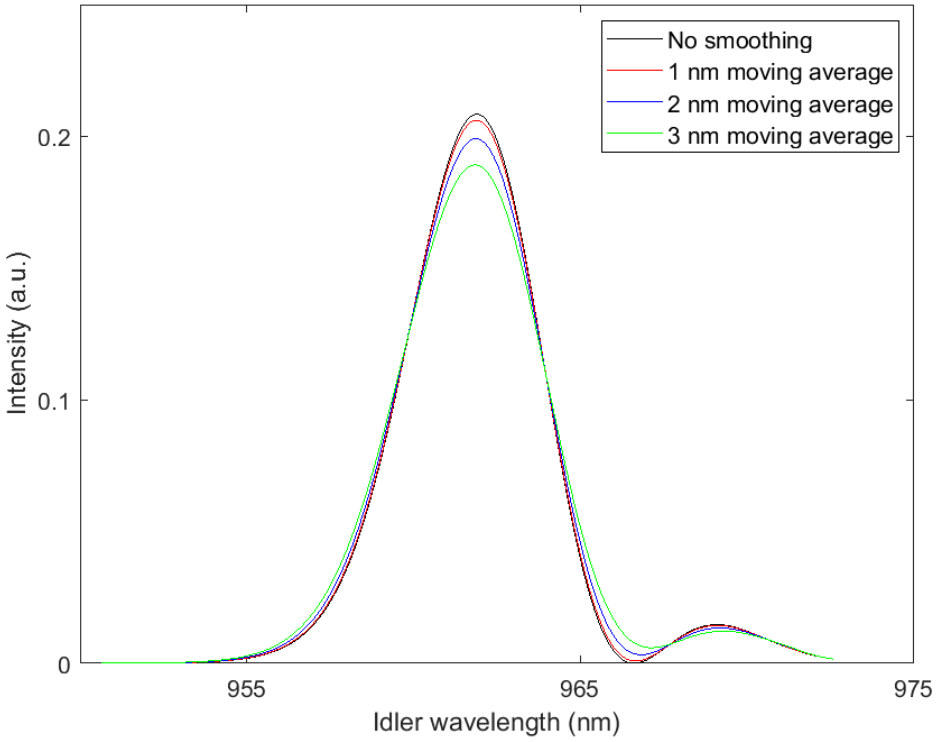

FIGURE 4.17: Cross-section of a theoretical joint spectrum plot with the idler wavelength equal to 960 nm. Varying amounts of smoothing are shown, implemented using moving average filters of different widths. Overlap integrals between the smoothed and unsmoothed data were also calculated, giving the following values: 0.9999 for 1 nm moving average, 0.9987 for 2 nm moving average, and 0.9942 for 3 nm moving average.

4.4 Conclusion

In summary, we have demonstrated an approach to JSI measurements of photon pair sources using stimulated four wave mixing, seeding the process with chirped white light. This approach can perform a joint spectrum measurement in as little as 5 s and high resolution joint spectra can be obtained in under 30 s. This offers substantial improvements in speed compared to both recently demonstrated techniques [58, 61] and traditional techniques [56] with measurement times on the scale of minutes and hours respectively. A further advantage of this technique is the reduced need for experimental apparatus compared to other joint spectrum measurement methods. Rather than requiring multiple laser sources, only one pulsed laser and a method for supercontinuum generation are required. Photonic crystal fibers, or other highly nonlinear medium, can easily generate the needed seed bandwidth. Depending on the resolution desired, an inexpensive, modular spectrometer is often sufficient, no other detectors are needed.

This approach may also be particularly useful in characterizing unknown photon pair sources. The seed produced through supercontinuum generation spans over 350 nm,

meaning that one can easily scan through a large range of seed wavelengths to rapidly identify a source's output modes. The rapid characterization opens the door to real time adjustments and measurements. In the following chapter, we make use of this rapid measurement tool to characterize the effect on the JSI of various modifications to fiber-based photon sources. The speed of the tool allows us to record a large number of joint spectra as various fiber parameters are changed.

Chapter 5

Tunable JSI through Fiber Modification

5.1 Introduction

Birefringent optical fibers are a versatile medium for photon pair generation. As discussed in Ch. 3, the joint spectral intensity (JSI) is a convenient way to measure the spectral properties photon pair sources. Together, the pump bandwidth, material dispersion, fiber length, and fiber birefringence all determine the JSI. An interesting question is can we modify the JSI of photon pair sources in a useful way?

One example of a useful modification would be the ability to shift the produced signal and idler wavelengths. Many optical components, such as filters, waveplates, and detectors, work best at a particular wavelength. It would be ideal if the output of a photon pair source could be tuned depending on the surrounding experimental apparatus. Additionally, this could allow a source to alternate between several different frequency channels. Another interesting possibility is changing the shape of a photon pair's joint spectrum. As discussed in Ch. 2, the shape of the JSI is strongly tied to the purity of heralded single photons, so the ability to change JSI shape could make it easier to produce highly pure heralded photons. Looking beyond photon purity however, are there more interesting, unconventional JSI shapes that could be useful? For example, a fiber with a JSI containing two or more main lobes could act like a frequency multiplexed photon pair source.

One way to modify the joint spectrum of a photon pair source is to change the spectral profile of the pump; these effects can be calculated using the equations outlined in Ch. 3. However, it is not always possible or desirable to change the pump spectrum. The pump

intensity can also result in changes to the JSI, but this effect is usually small [69]. Another option, which is the subject of this chapter, is to change the birefringence of the optical fiber.

In this chapter, we explore how a variety of modifications to birefringent optical fibers affect the JSI of the photon pairs produced. The technique outlined in Ch. 4 is used to make rapid, high resolution measurements of the joint spectra as they change. First, this chapter outlines a few possible methods of birefringence modification and summarizes some previously demonstrated work. Then, we discuss several different approaches used here and their results.

5.1.1 Background

Birefringent fibers rely on asymmetry within the fiber to create two defined axes, a slow axis and a fast axis. One type of polarization maintaining (PM) fiber introduces this asymmetry with an elliptical fiber core, creating a defined axis of mechanical stress within the core. PM fibers with higher birefringence tend to use stress rods included within the fiber cladding to create a defined axis [41]; these are usually classified as panda and bow-tie type fibers, as described in Ch. 2.

Since the birefringence in PM fibers arises from stress in the fiber, it follows that changing the stress profile in the fiber should have some effect on the birefringence. A number of approaches have been tried or suggested to induce these birefringence changes. Some of these approaches are non-permanent changes, such as squeezing, bending, and temperature tuning the fiber. Other approaches are more permanent, including etching away some of the fiber cladding or tapering the fiber.

Some success in modifying the birefringence of polarization-maintaining fibers was achieved in the 1980's through bending fibers [70, 71]. Four-wave mixing in a birefringent fiber was studied and the central anti-Stokes wavelength was used to calculate the fiber birefringence. Bend-induced birefringence changes up to $\Delta n = 7 \times 10^{-5}$ were measured [70] in an elliptical core fiber. The same group also looked at birefringence changes in a PM fiber due to applied external stress [72]. This was significantly less successful than the bend-induced birefringence approach, producing only a small ($\Delta n \simeq 1 \times 10^{-5}$) shift in the birefringence, approximately 7 times less than the observed shift in the bending approach. The group also looked at the effect of temperature on the birefringence of an elliptical core fiber. The results were modest, showing a change in the birefringence of $\Delta n \simeq 7 \times 10^{-6}$ at a temperature of 700 °C. Something to consider is that fiber development has progressed significantly since the 1980's. In particular, other types of

birefringent fibers, such as panda and bow-tie style fibers have been introduced. Additionally, today's fibers are typically designed to be more stress, temperature, and bend insensitive, meaning that dynamic tuning of typical commercial fibers may be more difficult.

Outside the realm of traditional PM fibers, a variety of approaches have been demonstrated. Looking at microstructured fibers, significant success in birefringence tuning was achieved by filling air holes in a microstructured fiber with a polymer, then temperature tuning the refractive index of that polymer [73]. In that implementation, the authors were able to demonstrate a change in the birefringence of up to $\Delta n = 4 \times 10^{-4}$.

5.2 Experiment and results

In this chapter, we modify photon sources based on polarization maintaining fibers and explore the joint spectral effects due to these changes. A simple schematic of the experimental apparatus is shown in Fig. 5.1. The apparatus is very similar to that described in Ch. 4, and a more detailed experimental figure can be found in Fig. 4.1. The stimulated emission tomography approach to JSI measurements described in Ch. 4 is used here to make joint spectral measurements while the fiber-based sources are modified. The stimulated four wave mixing process is seeded using a chirped, broadband pulse covering the idler wavelength and the generated signal beam is measured with a spectrometer.

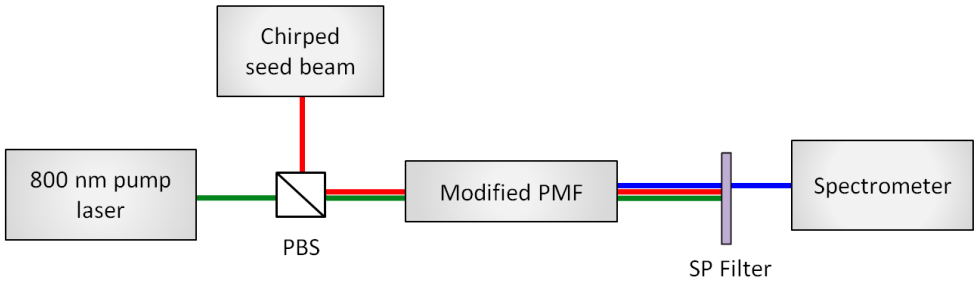

FIGURE 5.1: Block diagram of the experimental apparatus used to test the modified fibers. The green line is used to shown the pump path, the red line shows the seed beam, and the blue line shows the signal beam generated in the stimulated four wave mixing process. PBS, polarizing beamsplitter; PMF, polarization maintaining fiber; SP filter, 750 nm short pass filter.

It should be noted that for some of the results described in this section, the fibers tested were relatively long (>10 cm) compared to the 2.5 cm photon source in Ch. 4. Due to the length of these fibers, walk-off between the pump and the seed beam is non-negligible and causes a substantial smoothing effect in the idler axis (described further in Ch. 4). Despite this effect, the joint spectra presented in this section are still able to show the major effects due to the fiber modifications. More accurate joint spectral measurements

could be achieved by increasing the chirp on the seed beam. However, this would also result in a decrease in intensity of the signal beam produced through stimulated four wave mixing.

Two different fibers were modified and tested: a traditional single mode, PM fiber, as well as a PM microstructured fiber. Both fibers support a single mode at the pump wavelength and both have relatively high birefringence. The high birefringence helps ensure that the idler photon wavelength is suitably far from the pump wavelength. This makes it easier to distinguish the idler photons from noise generated through Raman scattering. The traditional single mode fiber was the Fibercore HB800; this is a bow-tie style PM fiber with a germanium-doped silica core. It is the same fiber used in Chapters 4 and 6 for the photon pair source. The microstructured fiber tested is the Thorlabs LMA-PM-5, which is an endlessly single-mode PM photonic crystal fiber with a 5 μm core diameter. This fiber has a hollow capillary structure designed so that the fiber is single-mode for all wavelengths where fused silica is transparent. Additionally, it has two stress rods (panda type) to provide birefringence in the fiber. An illustration showing the approximate structure of these two fibers is shown in Fig. 5.2. Both fibers also have an acrylate protective coating (not shown in Fig. 5.2).

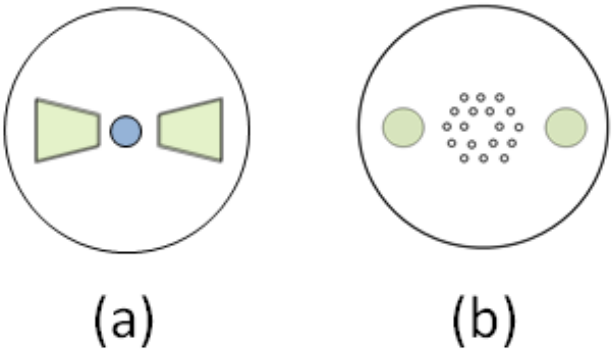

FIGURE 5.2: Illustrations of (a) a bow-tie style PM fiber and (b) and panda style PM photonic crystal fiber. Illustrations are not to scale. The blue area in (a) represents the fiber core, the green areas in (a) and (b) represent stress rods, and the small circles in (b) represent air holes in the PCF.

Three main approaches to modifying the PM fibers were used: squeezing, bending, and tapering the fibers. These approaches are described in more detail in the following sections. The first two approaches are dynamic in that they are non-permanent changes which could conceivably be made in-situ, and adjusted in real time. Dynamic techniques to JSI modification are highly desirable because they would increase the versatility and range of applications of photon sources. The third approach, tapering the fiber, is a permanent change and not dynamically tunable. Once the taper has been made, it is

fixed. However, tapering is a well-established and highly reproducible technique for fiber modification, which would be advantageous from a production standpoint.

5.2.1 Squeezing

One approach used to modify the joint spectrum of photon pair sources was based on squeezing the fiber source to provide lateral stress. As stress is applied across the fiber, it is reasonable to expect that there may be some resultant change to the birefringence in the fiber. Two different ways of squeezing the fiber were explored: a manual fiber polarization controller and a micro-vise.

5.2.1.1 Manual fiber polarization controller

Manual fiber polarization controllers are commercially available products which can be used to produce an arbitrary output polarization state for an arbitrary input polarization. The fiber is clamped at both ends of the device, while the middle section of the polarization controller can rotate around the fiber and squeeze the fiber with a variable pressure, as shown in Fig. 5.3. The external pressure introduces a small birefringence in the fiber, which acts as a waveplate. As the controller squeezes harder on the fiber, the birefringence increases, increasing the retardance of the induced waveplate [74]. Here, we use the polarization controller to squeeze a PM fiber in a effort to change the existing birefringence of the fiber.

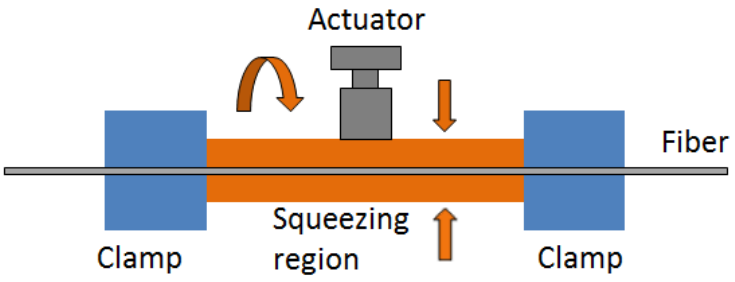

FIGURE 5.3: Schematic of a manual fiber polarization controller based on a rotatable squeezing element. The squeezed region is 4.5 cm long.

Using the manual fiber polarization controller, a 10 cm long piece of the PM photonic crystal fiber was tested. As shown in Fig. 5.4, some changes in the shape of the JSI of the photon pair source were observed based on squeezing. However, no large shifts in the central wavelengths of the signal and idler photons were observed. For some levels of squeezing, the JSI sidelobes become much brighter compared to the intensity of the main feature. At other levels of squeezing, such as subplot (d) in Fig. 5.4, the JSI looks very similar to the joint spectrum of the unsqueezed fiber. The effects also

show some dependence on the angle of squeezing relative to the axis of the stress rods in the PM fibers, as shown in Fig. 5.5, but the overall JSI characteristics are similar. The orientation of the fiber was measured by looking at which linear polarizations were preserved in the fiber. While the joint spectra shown here are for the PCF tested, the HB800 PM fiber was also tested, with similar results.

Interestingly, some of the results from these tests help strengthen the conclusions made in Chapter 4 regarding the cause of an asymmetric measured joint spectrum. Looking at subplots (b) and (d) in particular from Fig. 5.4, there is a clear asymmetry in the sidelobes relative to the highest intensity feature. This suggests that external stress on a fiber can cause the kind of joint spectral asymmetry described in Chapter 4.

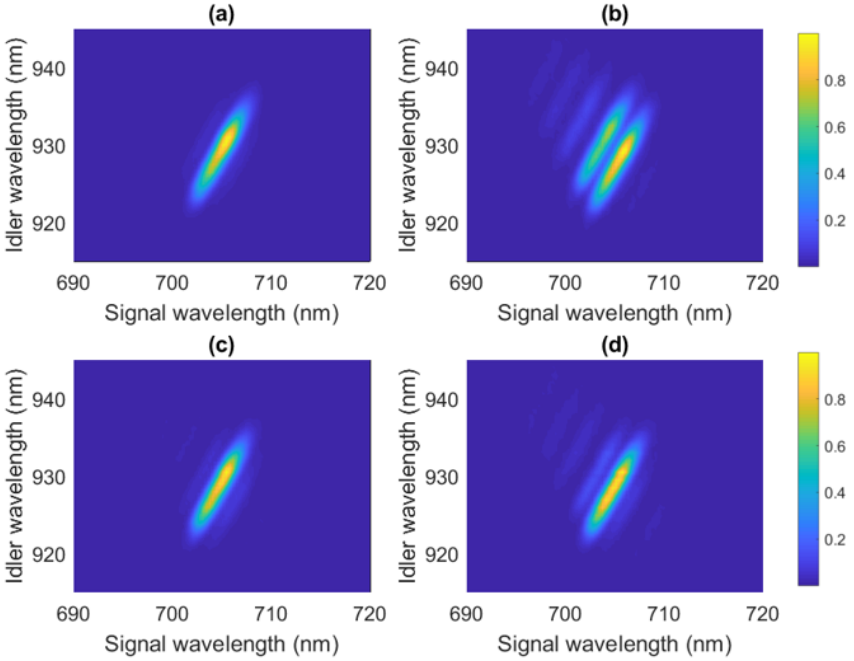

FIGURE 5.4: Example joint spectra of a PCF squeezed along the fiber fast axis using a manual fiber polarization controller. (a) no squeezing, (b-d) increasing levels of squeezing.

5.2.1.2 Micro-vise

To achieve the largest dynamic range of squeezing possible, a device which could squeeze the fiber to the point of damage was desired. This level of applied stress was not possible with the manual polarization controller, so for high levels of applied stress, a micro-vise (purchased from Kammrath and Weiss Technologies, Inc.) was used. A diagram and an image of the micro-vise are shown in Fig. 5.6.

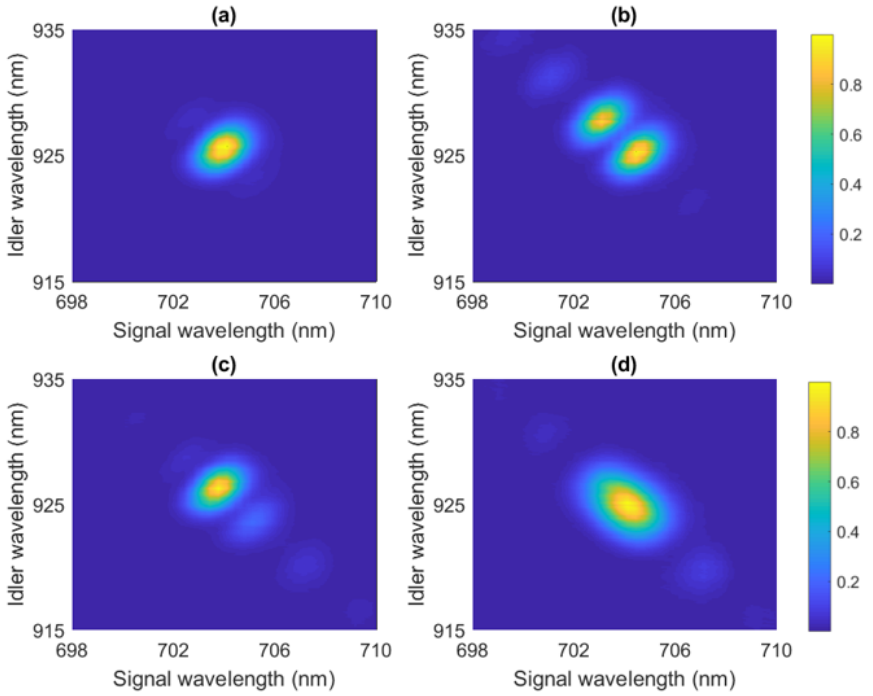

FIGURE 5.5: Example joint spectra of a PCF squeezed at different angles using a manual fiber polarization controller. (a) no squeezing, (b) squeezed along the fiber fast axis, (c) squeezed along the slow axis, (d) squeezed at 45° to the fast axis. The force applied to the fiber varies across (b-d).

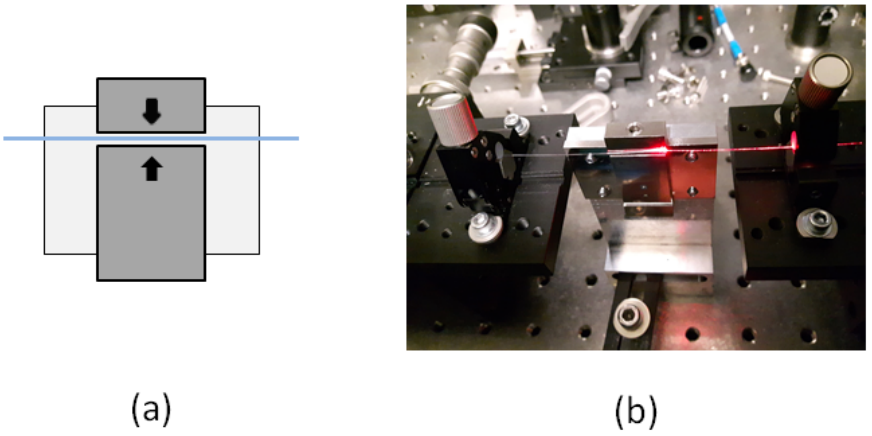

FIGURE 5.6: (a) Diagram of the micro-vise used, where the blue line represents the fiber and the black arrows show the direction of squeezing. The squeezing region is 1.8 cm long. (b) Picture of the micro-vise in operation. The fiber is held clamped at either edge of the picture by a clamp and is squeezed in the middle by the micro-vise. This fiber has been squeezed to the point of material damage, and visible light is coupled into the fiber showing the scatter coming from the crushed fiber section.

As shown in Fig. 5.7, the JSI results are quite similar to the results from the polarization controller. Again, there is no major shift in the signal and idler central wavelengths, even when the fiber is squeezed to the point of irreversible material damage. There does not seem to be a discernable trend that appears as the fiber is squeezed more and more. Results for both the PCF and the SMF tested were comparable.

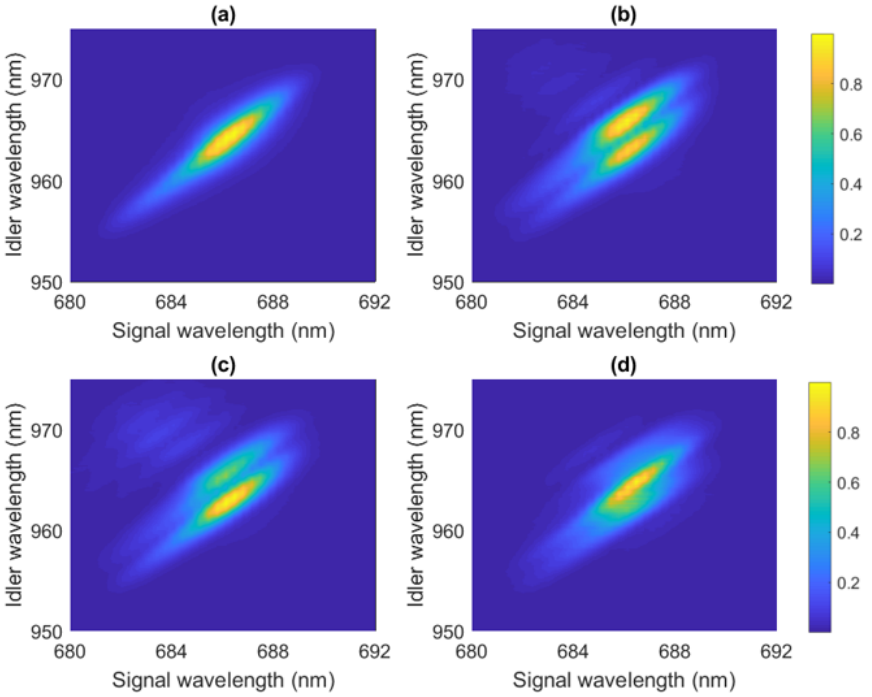

FIGURE 5.7: Example joint spectra of a ∼10 cm long PM fiber (Fibercore HB800) with (a) no squeezing and (b-d) increasing amounts of squeezing applied with a micro-vise. The JSI shown in (d) was recorded at a squeezing force just below the force needed to crush the fiber. The pump spectrum used for this measurement was 9 nm.

To better understand the effect of squeezing on the fiber, efforts were made to directly measure the change in birefringence induced by squeezing. This was done by looking at the interference between light travelling along the fiber slow and fast axes as the fiber was squeezed, as shown in Fig. 5.8. Using the 800 nm pump, the beam is prepared in a linear polarization state at 45° relative to the fast and slow axes of the PM fiber. The pump is then coupled into the polarization maintaining PCF, which is held in the micro-vise. A polarizer, also at 45°, is placed at the output of the fiber and the light which passes through the polarizer is sent to a power meter. As the micro-vise squeezes the fiber, the change in birefringence affects the phase difference between the light travelling along the fast and slow axes. This changes the polarization state at the output of the fiber. As the stress on the fiber increases, the measured power oscillates. Approximately 10 oscillations were observed as the fiber was squeezed from no stress up until its breaking point, corresponding to an induced phase difference of $\Delta\phi \simeq 20\pi$ radians.

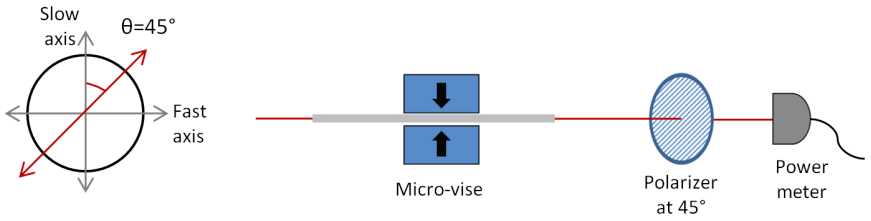

FIGURE 5.8: Schematic showing how the change in birefringence due to squeezing was measured. The diagram on the left shows the pump polarization relative to the fiber axes.

With some assumptions, this phase difference can be used to calculate the change in birefringence. As a first order approximation, we assume that the induced birefringence is constant, and exists over a distance $L = 1.8\,\text{cm}$ corresponding to the length of the micro-vise. Note that this is a very crude approximation, since the induced birefringence likely extends beyond this length and is likely not a constant value. With this assumption, the change in the propagation constant is $\Delta\beta = \Delta\phi/L = 3490$ rad/m. Using Eq. 5.1 to determine the change in refractive index Δn, we calculate $\Delta n = 4.4 \times 10^{-4}$

$$\Delta n = \frac{\Delta\beta\lambda}{2\pi}. \tag{5.1}$$

This calculated induced birefringence is very large, as it is comparable to the inherent birefringence of bow-tie and panda style PM fibers. Accordingly, one would expect to see changes on the order of 10 s or 100 s of nanometers in the signal and idler wavelengths produced as the fiber is squeezed. Clearly, this does not agree with what was observed. There are a few possible explanations for why these large changes in the joint spectrum are not observed. One possibility is that the birefringence induced by squeezing has some wavelength dependence. This would add more complexity to the phasematching function. Another possibility is that there could be interference between the signal produced in different sections of the fiber. Particularly if the birefringence profile along the fiber is continuously changing, the signal produced from different points along the fiber will certainly not be in phase. It should also be noted that the squeezed segment of the fiber is short compared to the non-squeezed segment (1.8 cm compared to 8 cm), so significantly less light may be produced in the squeezed segment. Lastly, there may also be other propagation modes travelling in the fiber. While for a single mode fiber, the TEM_{00} mode is the dominant mode, perhaps the squeezing transfers energy into higher order TEM modes or cladding modes. Higher order modes would have more loss and the propagation constants would be different, again making phasematching more complex.

In short, squeezing birefringent fibers resulted in changes to the shape of the measured joint spectra, but no substantial shifts in the idler and signal wavelengths. However, direct measurement of the change in birefringence suggests a large shift in wavelengths should be expected. Unexpected behaviour, such as higher order mode propagation, may explain why this shift is not observed.

5.2.2 Bending

As an alternative to squeezing fibers, bending was explored as a way to modify the joint spectral properties of fiber based sources. Bending a straight rod induces both tensile and compressive stress within the medium, which should have some effect on the fiber birefringence. Since it was not possible in this implementation to orient the fiber slow and fast axes relative to the plane of bending, it is not straightforward to picture or model exactly how the bending affects the stress profile within the fiber. However, reasonable success at modifying fiber birefringence was demonstrated in the 1980's with bending [70].

For these tests, the fiber was wrapped around a cylindrical object to achieve a uniform bend radius, as shown in Fig. 5.9. A short segment at either end of the fiber was kept straight and held in place with a clamp to facilitate coupling in and out of the fiber.

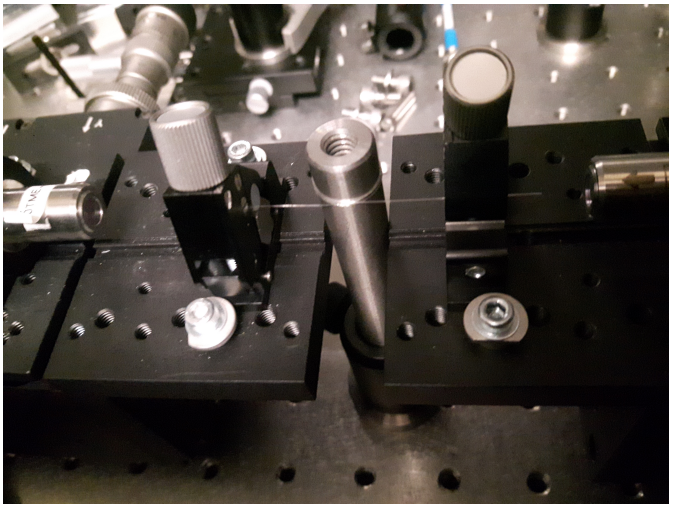

FIGURE 5.9: Photo of a fiber wrapped around a cylindrical object with a bending radius of R=6.4 mm. The fiber is clamped down on each side of the cylindrical object.

The response of the photonic crystal fiber to bending was tested by examining three different bending radii. In each case, the wrapped portion formed the majority of the fiber, with approximately 17 cm wrapped around the cylinder and approximately 3 cm kept straight both before and after the cylinder. As shown in Fig. 5.10, bending clearly induces significant changes in the joint spectrum compared to the same fiber held straight.

Bending greatly increases the bandwidth of both the signal and idler, with a tighter bend radius corresponding to a larger bandwidth. Looking at Fig. 5.11, a 3 mm bend radius increases the bandwidth in both the signal and idler by over a factor of 5 compared to the straight fiber. In addition to the change in bandwidth, the JSI of the bent fiber also has qualitative differences: it contains two bright features and many small lobes. Conversely, a typical joint spectrum contains one main feature, with symmetric side-lobes. Looking at Fig. 5.10, the two bright features move further away from the main peak in the straight fiber as the bending radius is decreased.

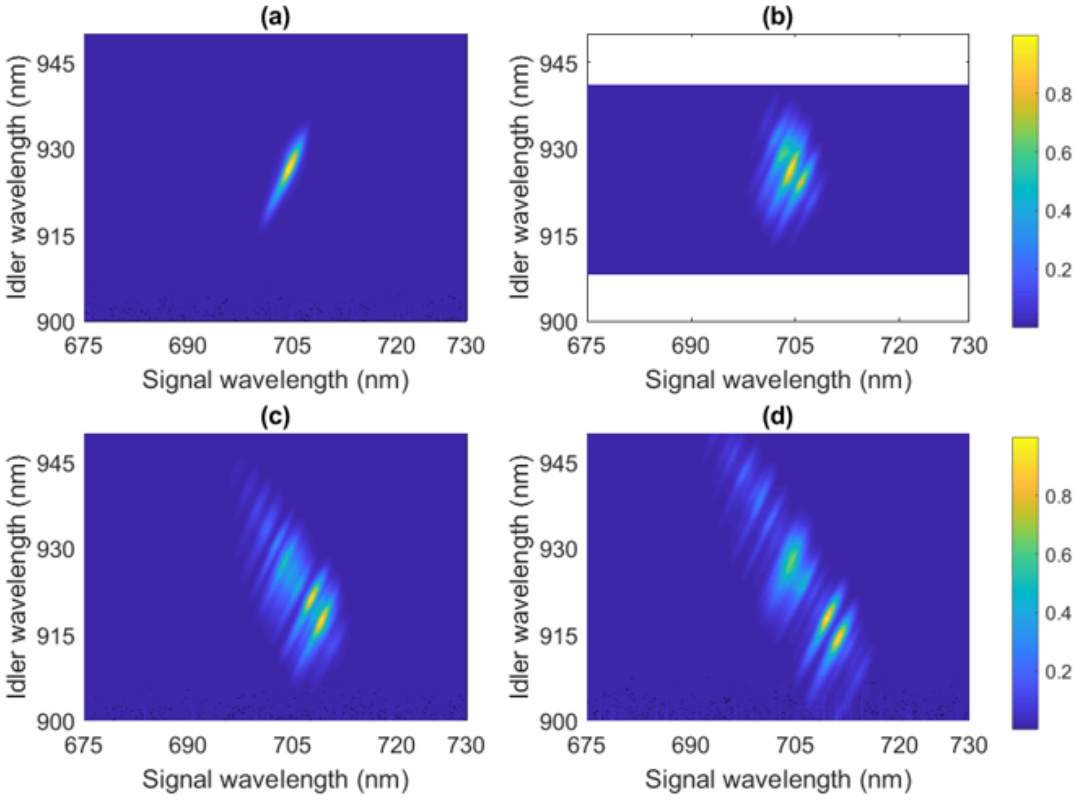

FIGURE 5.10: Example joint spectra of a 23 cm long birefringent PCF with (a) no bending, (b) R=6.4 mm (c) R=4 mm, and (d) R=3 mm bend radius. The pump bandwidth was 9 nm for these measurements.

To provide a theoretical comparison, we calculate the expected difference in propagation constant due to bending using Eq. 5.2, as outlined in [75]

$$\Delta\beta_{bending} = \frac{-1}{8}\left(\frac{d}{R}\right)^2 ECk_0\left[1 - \frac{a^2}{3d^2}H(V)\right], \tag{5.2}$$

where $\Delta\beta_{bending}$ is the change in propagation constant in radians/m, d is the diameter of the fiber cladding, R is the bend radius, E is Young's modulus, C is the photoelastic constant, k_0 is the wave vector in vacuum, a is the radius of the core, and $H(V)$ is a normalized frequency dependence factor.

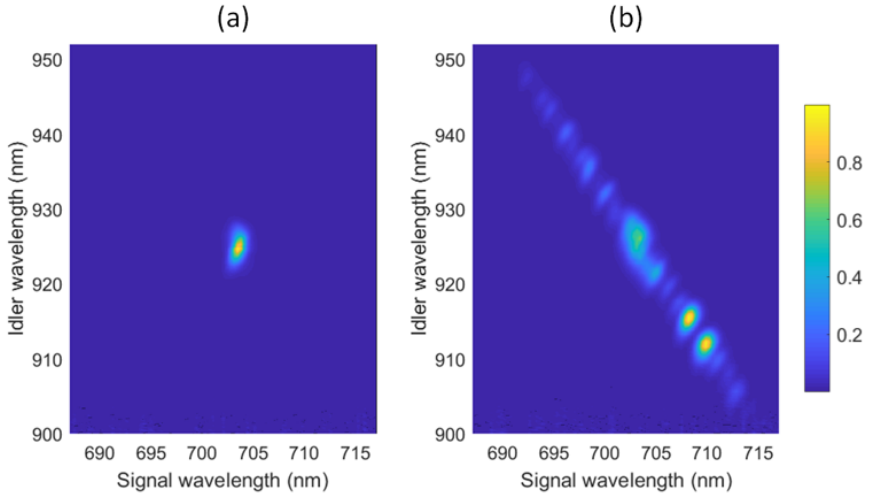

FIGURE 5.11: Example joint spectra for (a) straight fiber and (b) fiber with 3 mm bend radius using a pump bandwidth of 3 nm.

The factor V is defined as

$$V = ak_0\sqrt{n_1^2 - n_2^2}, \tag{5.3}$$

where n_1 and n_2 are the refractive indices of the fiber core and cladding respectively.

For the HB800, at 800 nm we have $n_1 = 1.4621$ and $n_2 = 1.4533$ based on the Sellmeier equation for fused silica and discussions with the manufacturer. Assuming a core diameter of 4.3 μm based on the mean field diameter of the fiber, we get $V = 2.7$. From Fig. 7 in [75], for $V = 2.7$, $H(V) < 5$ and is a negligle correction in Eq. 5.2. It is not possible to calculate $H(V)$ for the photonic crystal fiber tested, since there is no defined core and cladding. However, for the sake of simplicity it will be assumed that the correction due to $H(V)$ for the PCF is negligible as well.

For the photoelastic constant, a value of $C = 3.5 \times 10^{-12}\text{m}^2/\text{N}$ [76] was used. Note that this is an overestimation of the photoelastic constant for fused silica at 800 nm, but the range of wavelengths measured in [76] did not extend up past 650 nm. The values for Young's modulus and the cladding diameter are $E = 72$ GPa and $d = 125$ μm. Using these values in Eq. 5.2 with a bend radius $R = 3$ mm gives a value of $\Delta\beta = 480$ rad/m. Then the change in refractive index $\Delta n_{bending}$ can be calculated using Eq. 5.1.

For the 3 mm bend radius, this gives a bending-induced birefringence on the order of $\Delta n_{bending} = 6 \times 10^{-5}$. For the PCF measured here and assuming a reduction in birefringence, this would correspond to shifting the signal and idler wavelengths to approximately 716 nm and 906 nm respectively. Looking at Fig. 5.11, we see that while the two bright lobes in the bottom right corner of subplot (b) have not shifted quite as far as the predicted values, the observed shift is certainly comparable. It should be noted that in the experimental case, it was not possible to align the plane of bending

with one of the fiber axes, thus the true impact of bending may be significantly more complicated then what is captured by this calculation. One could therefore expect a range of different effects, where the birefringence varies from $\Delta n_{intrinsic} - \Delta n_{bending} < \Delta n < \Delta n_{intrinsic} + \Delta n_{bending}$ where $\Delta n_{intrinsic}$ is the birefringence of the fiber before bending. This may help explain the presence of many sidelobes in the joint spectrum and the dramatic increase in JSI bandwidth of bent fibers compared to the straight fiber. Based on this birefringence range, one would expect idler light to be produced between 906 and 944 nm, and signal light to be produced from 694 to 716 nm. From Fig. 5.11, the majority of the light produced does indeed fall within this range. At this time, the reason for the presence of two bright lobes in the bent fibers rather than a single lobe is not well understood. As discussed in the micro-vise subsection, this could be the result of multiple propagation modes in the fiber.

To summarize, bending birefringent fibers caused a clear shift in the signal and idler wavelengths, with the measured change in wavelength comparable to the calculated change. However, two bright features, rather than a single feature, were measured along with a multitude of smaller, faint features present across a large bandwidth. The mechanisms behind these other features are not well understood.

5.2.3 Tapering

Tapering was investigated as a way to permanently change the birefringence of PM fibers. Tapering involves heating the fiber with a torch and then stretching it to create a section with a smaller diameter. It seems reasonable to expect that changes in the diameter of the fiber and the size of the stress rods should have some effect on the stress profile within the fiber. In this case, the tapers were drawn adiabatically, which means that the transition between the untapered fiber and taper waist is smooth and gradual. This minimizes attenuation and coupling to cladding modes and higher order modes [77]. Figure 5.12 shows a schematic of a fiber taper, as well as a microscope image of a taper cross-section. Through microscope images, it was verified that the relative size of the stress rods compared to the fiber diameter is the same in the tapered regions as it is in the untapered fiber.

The HB800 bow-tie style fiber was modified by creating fiber tapers of several different diameters. The taper waist length for all tapers was 10 mm, and the total taper length (including transition regions) varied from 12.4 mm to 19.6 mm depending on the taper waist, with smaller tapers requiring longer transition regions. The diameter of the HB800 (without tapering) is 125 μm, and all fibers were pumped with a pump bandwidth of 4 nm.

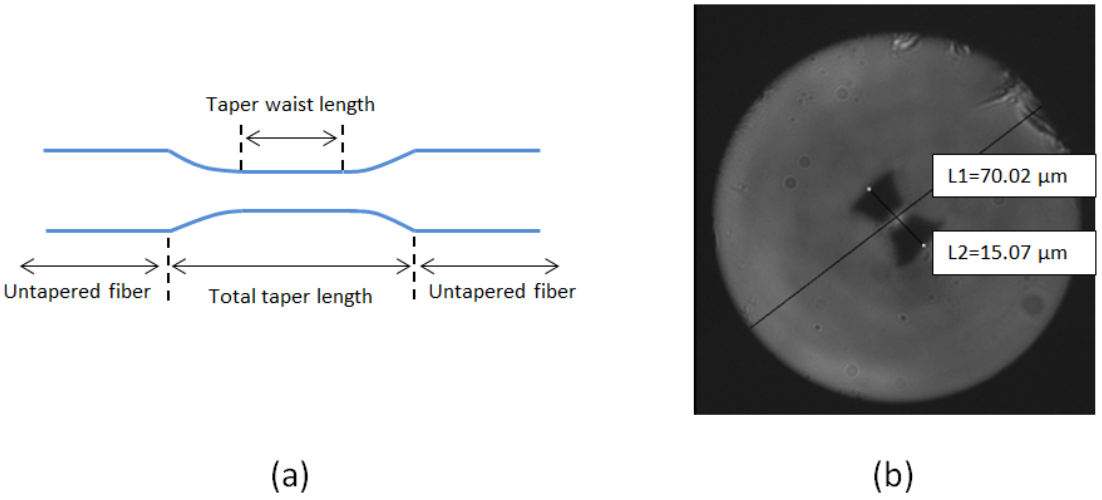

FIGURE 5.12: (a) Schematic of a tapered fiber and (b) microscope image of the cross-section of a tapered fiber. The cross-section is performed at the taper waist of a fiber tapered from 125 μm to 70 μm. As shown in (b), the bow-tie structure of the fiber remains intact throughout the taper.

One long (30 cm) fiber with a taper waist diameter of 95 μm was tested, as shown in Fig. 5.13. A distinct feature towards the lower right corner of the plot is present and thought to come from the tapered region of the fiber. This supports the idea that tapering a fiber can affect the fiber birefringence, and suggests that the birefringence in the tapered region is lower than in the untapered fiber. Fig. 5.13 also highlights how the joint spectral intensity measurement technique outlined in Ch. 4 can have resolution problems for long fiber sources. The two bright lobes, shifted relative to each other in the idler degree of freedom, originate from different regions of the fiber. One comes from the untapered fiber before the taper, and the other from the untapered region after the taper. The shift in the JSI between these two regions is not real, but is an artifact of the measurement technique which comes from the walk-off between the pump and seed within the fiber. However, this artifact does allow us to see that there is a distinct region in the middle of the fiber (the taper) where photons are not produced at the same wavelengths as in the untapered sections of the fiber.

To investigate the effect of taper diameter, a variety of fibers with taper diameters from 81 to 112 μm were tested. These fibers were kept short (total length $\sim$5 cm) to reduce the effect of walk-off on the measurements. The results of these tests are shown in Fig. 5.14. For tapers smaller than 80 μm, the seed beam was not guided well through the taper and coupling efficiencies were very low.

As shown in Fig. 5.14 subplots (c-f), the tapers clearly have an impact on the joint spectral properties of fiber-based photon sources. The joint spectra of the tapered fibers have a larger bandwidth than the untapered fibers, with many small features, similar

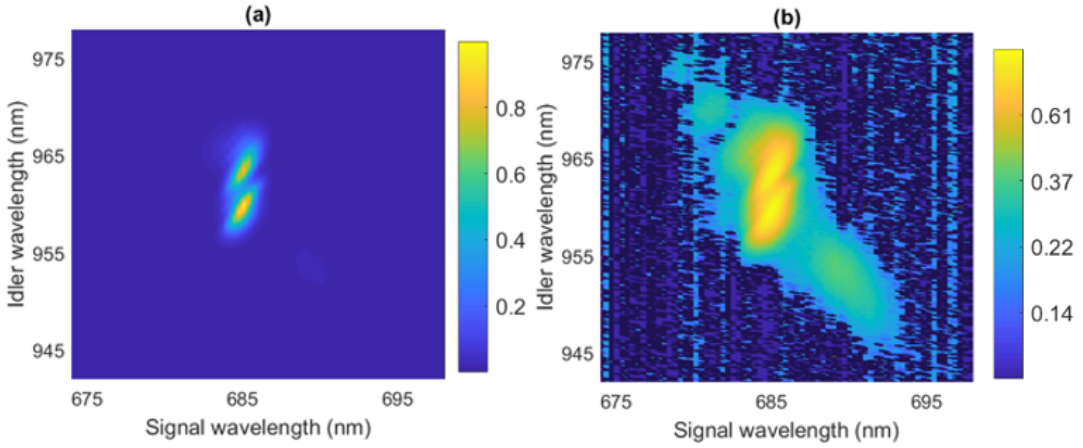

FIGURE 5.13: Joint spectrum for a 30 cm fiber with a 10 mm long 95 μm diameter taper (a) on a linear intensity scale and (b) on a logarithmic intensity scale.

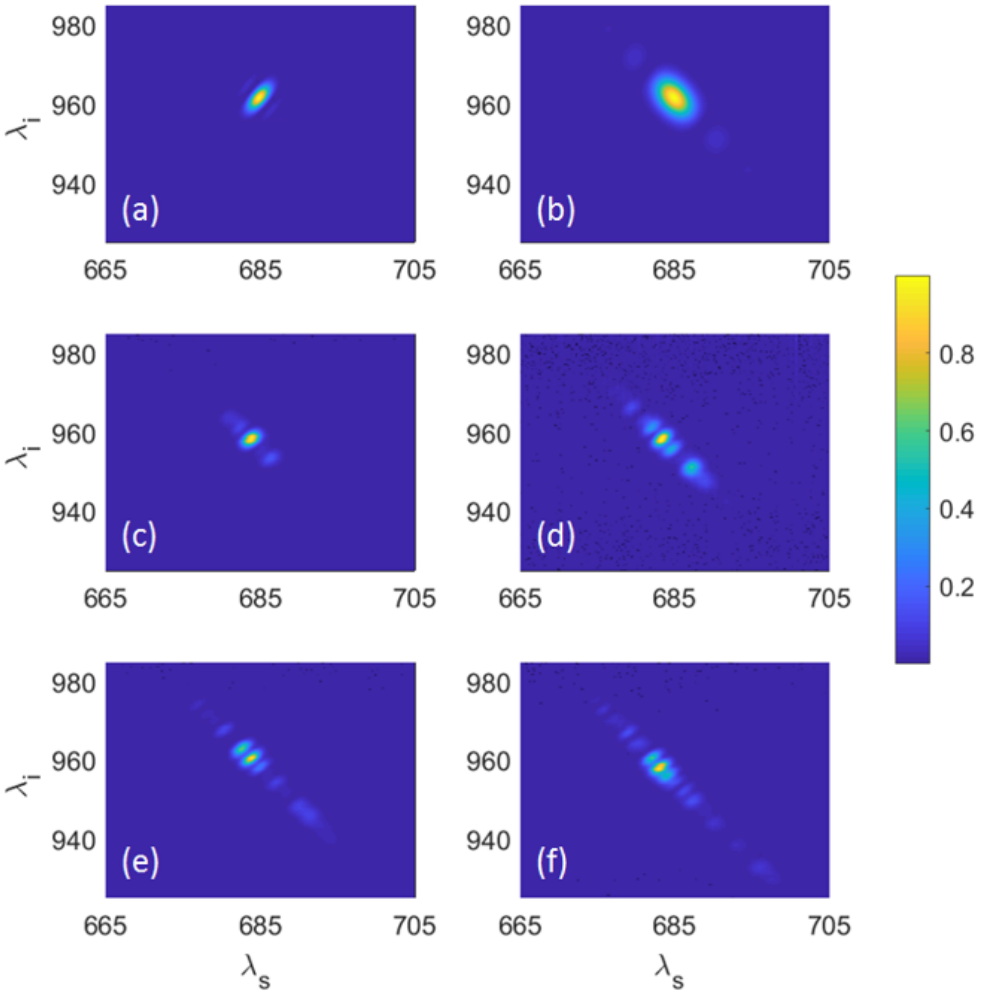

FIGURE 5.14: (a) Theoretical JSI for a 5 cm long fiber, (b) theoretical JSI for a 1.5 cm long fiber, (c-f) measured joint spectra for 4 different fibers, each with a total length from 4.5-5 cm and 10 mm taper in the center. The taper waist diameters are (c) 112 μm, (d) 101 μm, (e) 91 μm, and (f) 81 μm. All theoretical and measured joint spectra are for a pump bandwidth of 4 nm.

to the bent fibers from the previous section. Due to the number of small features, it is difficult to definitely say which features are produced in the tapered region or the transition regions. It is also difficult to quantify how the taper diameter affects the birefringence. However, this could certainly be further investigated by testing a broader range of samples. For example, one could draw a fiber such that the tapered region is longer than the transition and untapered sections; this way, a higher proportion of the stimulated four wave mixing light should come from the tapered region.

It is interesting to compare the joint spectra of the tapered fibers to the theoretical joint spectra of untapered fibers (Fig. 5.14 subplots (a-b)). The joint spectrum of the fiber with the largest taper looks somewhat similar to an untapered fiber of the same total length. In contrast, the fiber with the smallest taper has a central region consisting of three main lobes. Grouping those three lobes together, their shape and location bear some similarities to an untapered fiber only 1.5 cm long, which is a length comparable to untapered regions on either side of the taper. It is possible that the many lobes in the joint spectra of the tapered fibers comes from interference between light produced in the untapered sections at the front and back end of the fiber.

In short, tapering was used as a way to permanently change the joint spectral properties of photon pair sources. Results suggest that tapering results in a wavelength shift of the signal and idler, as well as many additional small features, similar to the joint spectra observed for bending fibers. However, the measured joint spectra are complex and more work will need to be done before a relationship between taper diameter and joint spectrum features can be more confidently described.

5.3 Conclusion

Three different approaches, squeezing, bending, and tapering, were all explored as ways to modify the birefringence of polarization maintaining optical fibers. Comparing the measured joint spectra, a commonality that emerges is the complexity of the joint spectra. In each case, there are more features than in an unmodified single mode fiber. The stress profiles created by these techniques within the fibers are not well understood, making it challenging to predict the birefringence in different sections of the modified fibers. Accordingly, there are plenty of opportunities for future work in the broad area of fiber modification. Further investigation could be done on the approaches shown here and a multitude of other fiber modification approaches could be attempted. These could include temperature tuning, etching the fiber cladding, applying strain, or writing patterns into the core or cladding of the fiber. Additionally, a variety of different types of

fibers could be tested, including non-birefringent fibers, side-pit fibers, or other microsctuctured fibers. This work presented in this chapter also highlights the importance of having a fast and reliable joint spectral measurement tool. Given the complexity of the system, it is significantly easier to measure the joint spectra than to attempt to model them theoretically. The speed of the technique is particularly valuable for characterizing dynamic modifications; many measurements, or even a video, of joint spectral properties could be used to track changes in real time.

Chapter 6

Optical Kerr Switching of Single Photons

While the two previous chapters have focused on sources of light, this chapter focuses on a process for the manipulation of light. We demonstrate an all-optical switch based on the optical Kerr effect capable of efficient switching at the single photon level. By examining photon statistics, we confirm that the switch maintains the non-classical nature of the input photons. Using the stimulated emission tomography approach outlined in Ch. 4, we characterize the process, showing that the switching operation does not change the spectral properties of the input heralded single photons.

6.1 Introduction

In both classical and quantum networks, switches are an essential component that allow for the routing and manipulation of bits and qubits. In quantum systems based on photonics, polarizationtime bins are a convenient degree of freedom for encoding quantum information, and are particularly well-suited for the transmission of photonic qubits over long distances [78]. The ability to switch or route time bin qubits quickly, with low noise, while preserving quantum information is a key step towards the realization of photonic quantum networks [79].

A range of approaches have been demonstrated as switches for photonic qubits. However, many of these approaches, such as those based on electro-optic modulators (EOMs) or micro-electromecanical systems (MEMs) [80] are either incapable of operating at ultrafast speeds and high repetition rates, or introduce unacceptable loss [79]. All-optical approaches, including those based on silicon-based ring resonantors [81] and

Nonlinear Optical Loop Mirrors (NOLMs) [82] have had more success. Preservation of photon entanglement has been demonstrated with NOLMs [79], with switching times as low as 45 ps [83].

Another all-optical switching approach uses the Optical Kerr effect to rotate the polarization of the light, which offers several advantages over other all-optical approaches. A Kerr effect based switch can operate with picosecond level switching windows, is straightforward to implement experimentally, and can operate efficiently with a broad range of pump and signal wavelengths. One example of a Kerr effect application is shown in [78]. In that work, the optical Kerr effect is used to convert from time-bin based photonic qubits to polarization-based qubits. In general, time bin qubits are better suited for long-distance transmission, while polarization qubits are easier to manipulate and detect, so efficiently converting between the two is an important step towards larger networks. In [78], the Kerr effect is used to selectively rotate the polarization state of one of two time bins. Afterwards, the two time bins are brought back into the same temporal mode using a birefringent medium. For ease of implementation, Kerr effect based switching was demonstrated with attenuated coherent beams. In this chapter, the Kerr effect based switching shown in [78] is extended to show switching of heralded single photons. Using the heralded single photon source outlined in Ch. 4, we develop demonstrate an efficient switch which operates at nanojoule level pump powers, picosecond timescales, and 80 MHz repetition rates. Additionally, the photon statistics and spectral properties are characterized before and after switching to show any noise introduced by the switching process.

6.1.1 Theory

The intensity dependence of the refractive index is known as the Kerr effect. This effect occurs in materials with a third order ($\chi^{(3)}$) nonlinearity [38], and the total refractive index in a material can be defined as $n = n + n_2 I$, where n_2 is the intensity dependent refractive index, and I is the light intensity. The value of n_2 for fused silica is on the order of $3 \times 10^{-16}\text{cm}^2/\text{W}$, so in general only ultrafast laser pulses reach the intensities needed to generate noticeable nonlinear effects.

One application of the optical Kerr effect is to manipulate the polarization of light. In this process, a strong pump propagates through a medium with a suitable intensity dependent refractive index (n_2). The intensity of the pump induces a change in the refractive index along the axis of polarization of the strong pump. The result is a medium where the refractive index along one axis is different; in essence a birefringent material. Similarly to a waveplate, this birefringence can rotate the polarization state

of a second beam, usually called the signal or probe beam. It is assumed that the probe beam is too weak to induce a significant change in the refractive index on its own. Unlike a waveplate, the degree of birefringence depends on the intensity of the pump. Additionally, the birefringence only exists while the pump is present the medium. Since the pump can be an ultrafast laser pulse, the Optical Kerr effect can work at ultrafast timescales.

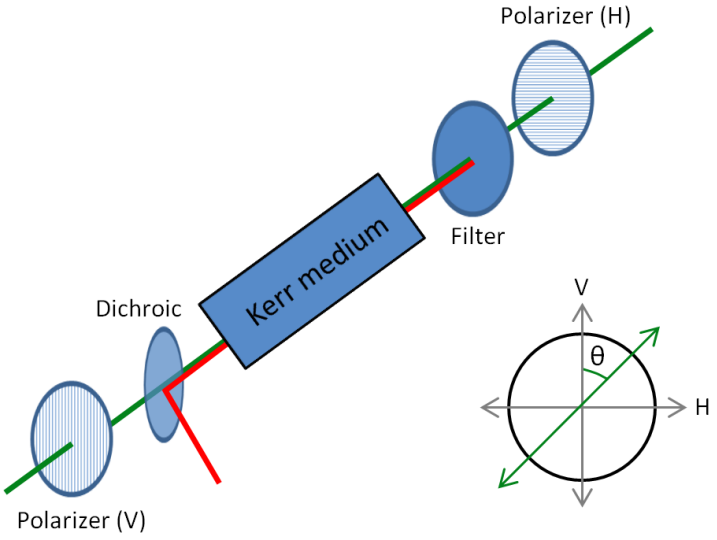

FIGURE 6.1: Schematic of a Kerr medium placed between two crossed polarizers, also called an Optical Kerr Shutter (OKS). The cross-section in the lower right shows the orientation of the pump relative to the polarizer axes. For maximum switching, the pump angle is set to $\theta = \pi/4$.

Often, the Kerr medium is placed between two crossed polarizers to make an Optical Kerr Shutter (OKS) [84]. Here, the transmission of the signal light through the second polarizer depends on the polarization rotation achieved through the Kerr effect.

The switching efficiency η i is given by [85]

$$\eta = \sin^2(2\theta)\sin^2\left(\frac{\Delta\phi}{2}\right), \tag{6.1}$$

where θ is the angle between the pump and probe beams, and $\Delta\phi$ is the phase shift induced by the pump beam. A switching efficiency of 0 corresponds to no polarization rotation, while an efficiency of 1 represents a rotation to an orthogonal polarization state.

The induced phase shift is given by the B integral

$$\Delta\phi = \frac{2\pi}{\lambda_{probe}} \int n_2 I(z) dz, \tag{6.2}$$

where n_2 is the intensity dependent refractive index of the medium, z is a length parameter, I is the intensity of the pump, λ_{probe} is the wavelength of the probe, and we integrate over the length of the Kerr medium.

6.2 Experiment

A schematic of the experimental apparatus is shown in Fig. 6.2. The apparatus consists of two main segments: the photon pair source and a medium suitable for Kerr switching. The photon pair source used here is the same pair source used and described in Ch. 4 based on spontaneous four wave mixing (SFWM) in a polarization maintaining fiber (PMF). However, in this chapter the photon pair source is operated mostly in the spontaneous four wave mixing regime, with no seed to stimulate the process. An energy level diagram of the SFWM process is shown in the inset of Fig. 6.2, but a more detailed description of this photon pair source, including photon statistics of the source, can be found in Ch. 4. Here, the Kerr medium used is a 10 cm, commercially available single mode fiber (Thorlabs S630-HP). In [78], a yttrium aluminum garnet (YAG) bulk crystal is used as the Kerr medium, chosen for its relatively high n_2. However, Kerr switching was later tested with single mode fiber, which has a lower n_2, but a much longer interaction length due to the guiding properties of optical fiber.

The same Titanium-Sapphire oscillator used in Ch. 4 is used in this section to pump both the photon pair source and the Kerr switch. A beamsplitter is used to direct approximately 70 mW of pump power to the photon pair source, which has a coupling efficiency of just under 50%. The remainder of the oscillator pump power is used as the pump for the Kerr switch. After the signal and idler photons are generated, they are split on a dichroic and the idler is coupled to an avalanche photodiode (APD) to act as the herald for the signal photons. Rather than coupling the signal photons to a spectrometer, as shown in Ch. 4, here the signal photons are prepared for the Kerr switch. To set the input signal polarization, we rotate the signal photons into the diagonal polarization. The polarization preparation is not perfect however, with approximately 1% of the signal photons leaking into the anti-diagonal polarization.

As shown in Fig. 6.2, a portion of the oscillator pump is used as the Kerr switch pump. This portion of the pump is spectrally filtered to a bandwidth of $\Delta\lambda_{pump} = 2.6\,\text{nm}$ in order to reduce the amount of self-phase modulation (SPM) that occurs in the Kerr medium. Additionally, 5 cm of SF69 glass is used to chirp the pump pulse, increasing its duration and further reducing the peak intensity. SPM can cause spectral broadening and other undesirable effects which can increase noise, and chirping the pump was observed to significantly reduce the number of noise photons at the signal wavelength

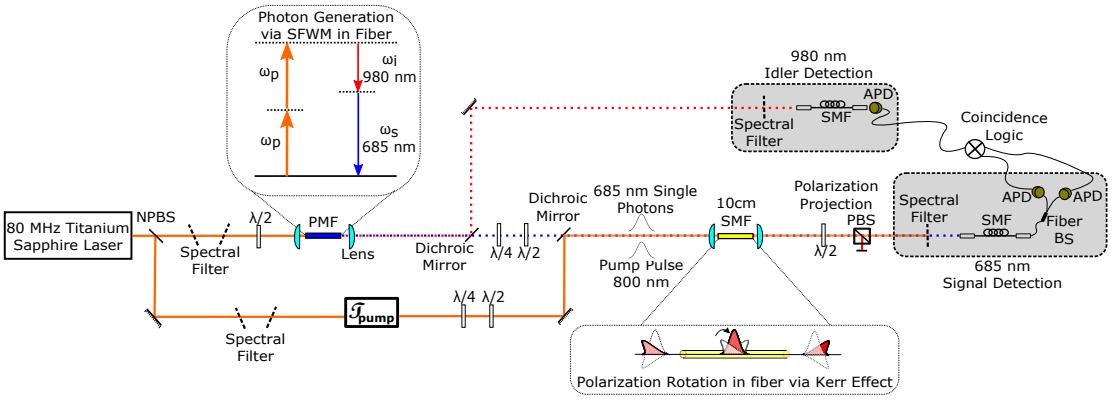

FIGURE 6.2: Schematic of the experimental apparatus. NPBS, non-polarizing beam-splitter; $\lambda/2$, half wave plate; $\lambda/4$, quarter wave plate; SFWM, spontaneous four wave mixing; PMF, polarization maintaining fiber; τ_{pump}, variable time delay in the pump; SMF, single mode fiber; PBS, polarizing beam splitter; APD, avalanche photodiode.

generated by the pump through SPM. After the SF69 glass, the pump passes through an optical delay line with variable delay (τ_{pump}) before combination with the signal photons on a short-pass dichroic mirror.

After combination, the signal photons and pump beam are coupled into the 10 cm single mode fiber (SMF) for Kerr switching. Compared to a bulk Kerr medium, the use of a fiber ensures good spatial overlap over a longer optical pathlength. This increased interaction length reduces the pump pulse energy required for efficient switching. For example, the pump energy required here is several hundred times less than the pump energy required in [78]. After the Kerr medium, a set of quarter and half-waveplates ($\lambda/4$ and $\lambda/2$) and a polarizing beam-splitter (PBS) are used to analyze the polarization of the signal photons. Projecting onto anti-diagonal polarization corresponds to photons successfully switched in the Kerr medium and projecting onto diagonal polarization corresponds to photons not switched. Spectral filters remove the pump beam, then the signal photons are coupled to an APD via single mode fiber. When making measurements, we look for heralded signal photons, or coincidences between the signal and idler APDs. For some measurements, the APD for signal photon detection is replaced by a fiber beam-splitter (BS) with the outputs coupled to two independent APDs (as shown in Fig. 6.2).

While the results outlined in the following section were achieved using heralded single photons, stimulated four wave mixing, as outlined in Ch. 4, was used extensively when setting up the experimental apparatus. Having a bright beam at the signal photon wavelength and in the same spatial mode was very useful for aligning all optics after the photon pair source. It was also helpful for tasks such as finding the zero delay point between the pump and signal, as well as measuring and optimizing coupling efficiencies. Lastly, the switching efficiency of the bright signal beam was a good approximation for

the switching efficiency of the single photons under the same pump conditions. This allowed for optimization of the switching using a bright beam and a table-top spectrometer, rather than relying only on single photon detectors.

6.3 Results

The Optical Kerr switch demonstrated was characterized by measuring the noise and switching efficiency as a function of pump pulse energy. During this measurement, the pump polarization is set to horizontal polarization, such that it is rotated by 45° with respect to the signal polarization. The variable delay τ_{pump} is set to 0. We project the signal photons on the anti-diagonal (switched) polarization to look for switched, heralded signal photons. As expected from Eq. 6.1, the switching efficiency follows a sine squared dependence on the pump energy. The efficiency peaks at 96% switching, occuring at a pump power of 3.0 nJ. We also measure the noise characteristics of the switch by blocking the input signal photons. Here, the main noise mechanism is self-phase modulation of the pump within the Kerr medium. Around maximum switching, the noise level is on the order of $\sim 1 \times 10^{-4}$ noise photons per pump pulse. We note that if a shorter signal wavelength were used, the pump energy needed for maximum switching would be lower. This would have the added benefit of reducing the number of noise photons, increasing the signal to noise ratio (SNR).

To examine the temporal response of the switch, the switching efficiency was also measured as a function of delay between the pump pulse and signal pulse, as shown in Fig. 6.4. In this case, the pump energy was set to 3.0 nJ per pulse for maximum switching efficiency. We look at both switched heralded photons (anti-diagonal polarization) and anti-switched heralded photons (diagonal polarization). Considering the flat-top section of the efficiency curve around zero delay, we can calculate the efficiency and the SNR of the switch. We define the switch efficiency as

$$\eta_{\text{switch}} = \frac{N_{\text{switch}} - N_{\text{noise}}}{N_{\text{input}}}, \tag{6.3}$$

where N_{switch} is the mean switched photon counts near zero delay, N_{noise} is the mean photon noise counts, and N_{input} is the mean input photon counts. This gives a maximum switching efficiency of $\eta_{\text{switch}} = 96.7 \pm 0.5\%$.

Similarly, we define the signal-to-noise ratio (SNR) as the ratio between the coincidence counts recorded at peak photon switching efficiency and the noise counts. The SNR was found to be 790 ± 70, approximately 80 times higher than the SNR for a similar switch

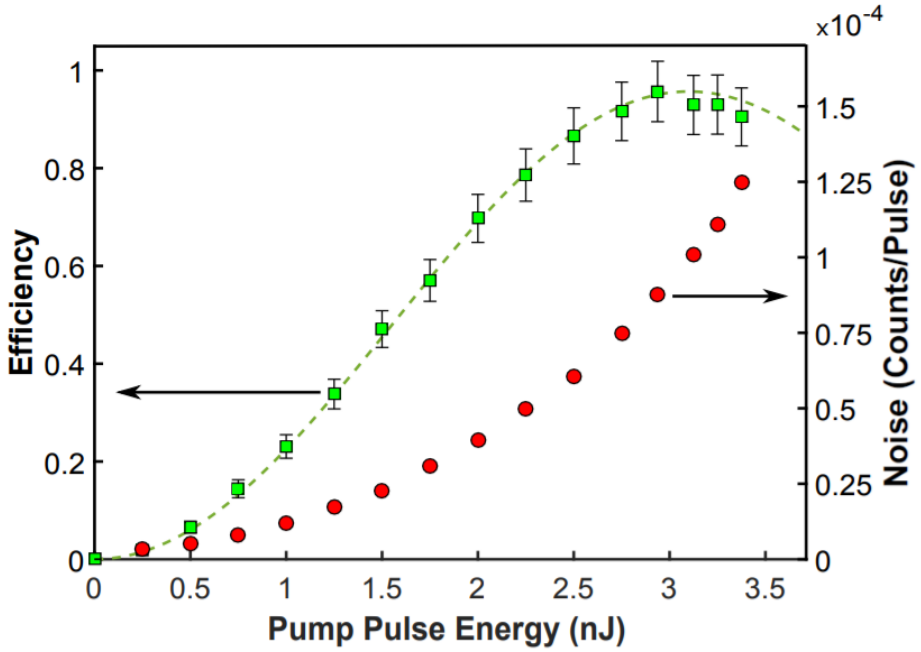

FIGURE 6.3: Measured switching efficiency (green squares, left ordinate) and noise (red circles, right ordinate) as a function of pump pulse energy, where the pump energy is measured at the output of the Kerr medium. The efficiency is fit with $\sin^2(\frac{\Delta\phi}{2})$ (dashed green line), following Eqs. 6.1 and 6.2.

performed in a bulk crystal setup [78]. Two major differences in this implementation allow for a significant pump energy reduction compared to the bulk crystal switch; the use of optical fiber increases the interaction length, and the condition that the pump fully walks through the signal ensures that all energy in the pump pulse contributes to the induced phase difference. This significant reduction in pump energy required leads to improved SNR, as the main source of noise is from self-phase modulation of the pump. The pump energies used in this demonstration are comparable to those needed for the NOLM approach [79].

The width of the switching efficiency curve in Fig. 6.4 corresponds to the speed of the switch, with a measured full width at half maximum (FWHM) of $\Delta t_{switch} = 1.69 \pm 0.01$ ps. This switching response depends on three main factors: the pump duration, the signal duration, and the walk-off between the pump and signal within the Kerr medium. In this implementation, the pump duration is measured through autocorrelation to be 410 fs. The signal temporal profile is calculated to be the convolution of a 100 fs Gaussian and a 380 fs rectangle function based on the length of the photon source and the photon source pump duration. The temporal walk-off between the pump and signal can be calculated using the length of the fiber (L=10 cm), the group index of the pump and signal wavelengths $\big(n_g(800) = 1.4671$ and $n_g(685) = 1.4720\big)$ [86], and the speed of light, c. Then the temporal walk-off Δt is given by

$$\Delta t = \frac{L\big(n_g(685) - n_g(800)\big)}{c} = 1.63\,\text{ps}. \tag{6.4}$$

To determine the intrinsic response of the Kerr switch (independent of the input signal), we use the pump duration and the pump-signal walk off to numerically calculate the B integral from 6.2 as a function of pump delay τ_{pump}. The resulting delay-dependent nonlinear phase-shift $\Delta\phi(\tau_{pump})$ is inserted into Eq. 6.1 to determine the intrinsic efficiency response function of the switch. This is the switching efficiency an input delta function would experience as a function of τ_{pump}. The intrinsic response function is independent of the switch input and its width determines the fastest possible switching speed. However, the total switching efficiency for a given input depends on both the properties of the switch and the properties of the input signal. To calculate the switching efficiency of the input signal photons used here, we integrate the intrinsic response function over the duration of the signal photon, weighted by the temporal profile of the signal photon. This total efficiency curve is shown in Fig. 6.4 (dashed green line). The calculated switching curve width $\Delta t_{calc} = 1.63\,\text{ps}$ is in good agreement with the measured temporal response ($\Delta t_{switch} = 1.69 \pm 0.01\,\text{ps}$).

The speed of the switch can be improved by choosing the length of the Kerr medium appropriately. In this implementation, the pump and signal need to walk through each other completely for efficient switching. Otherwise, the signal will see a non-uniform phase shift. This walk-through requirement defines the lower limit on the length of the Kerr medium. In this situation, we define the two pulses as separate when their peaks are separated by the sum of their $1/e^2$ half-widths. Accordingly, complete walk-through for the pulse durations and Kerr medium used here requires $\tau'_{pump} + \tau'_{signal} = 1.19\,\text{ps}$, where τ' represents the $1/e^2$ full width of a pulse. The switch response time could be further improved by reducing the durations of the pump and signal. However, a shorter pump pulse of comparable energy would lead to higher SPM and higher noise levels.

6.3.1 Characterization of the switched photons

While the speed and efficiency of a switch are clearly essential parameters, it is also important to characterize the effect of the switch on the input single photons. Particularly for quantum photonic applications, noise can be very detrimental and needs to be tightly controlled. While an ideal switch adds no noise, in reality, almost no operation is totally noise-free. A perfect Kerr switch would also have no impact on any photon property except the polarization. Any changes in the spectral mode or other properties of the signal photon could have negative implications on photon indistinguishability in some quantum protocols. In this section we characterize the Kerr switch's effect on noise

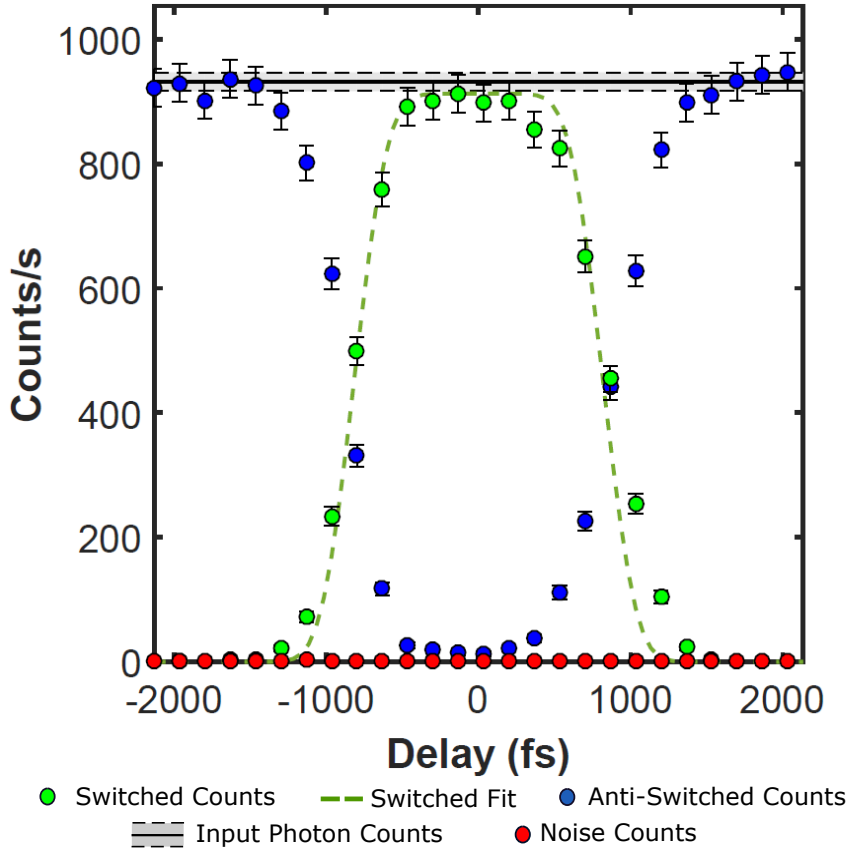

FIGURE 6.4: Heralded signal photons measured in the switched polarization (green circles) and unswitched polarization (blue circles) as a function of the pump delay τ_{pump}. The calculated temporal response (dashed green line) is modelled using the pump and signal durations, as well as the calculated walk-off within the Kerr medium. The input photon count (solid black line, with grey shading denoting uncertainty) and the noise photon counts (red circles) are also shown. Error bars are based on Poissonian statistics.

and spectral correlations in the signal by examining the second order autocorrelation and joint spectral intensity respectively.

6.3.1.1 Second order autocorrelation

Measurements of the second order autocorrelation function $\left(g^{(2)}_{s,s}(0)\right)$ were made as a function of power to examine the effect of the switch on the photon source statistics, as shown in Fig. 6.5. For these measurements, the signal photons were sent to a 50:50 beamsplitter with each output coupled to an APD (as shown in Fig. 6.2). Since the main mechanism for noise is self-phase modulation of the pump in the Kerr medium, we compare the measured $\left(g^{(2)}_{s,s}(0)\right)$ values to values calculated by assuming there is no coherence between the noise and signal photons, as described in Appendix B.4 in [87].

This model calculates the total result of the second order autocorrelation $\left(g^{(2)}_{tot}(0)\right)$ assuming that the total field is an incoherent mixture of the signal and noise fields, as if they were combined on a beamsplitter. This model is summarized in Eq. 6.5

$$g^{(2)}_{tot} = \frac{(N_{sig})^2 \cdot g^{(2)}_{sig} + 2N_{sig} \cdot N_{noise} + (N_{noise})^2 \cdot g^{(2)}_{noise}}{(N_{sig} + N_{noise})^2} \tag{6.5}$$

where N_{sig} and N_{noise} are the number of heralded signal and heralded noise photons respectively, and $g^{(2)}_{sig}$ and $g^{(2)}_{noise}$ are the second order autocorrelation functions of the signal and noise photons independently [87]. There are three different terms which contribute to $g^{(2)}_{tot}$. The first term on the right hand side of Eq. 6.5 corresponds heralded coincidences between two signal photons. This is simply a reflection of the source quality, and is tied to the $g^{(2)}$ of the input photons. The second term is a cross-term corresponding to heralded coincidences occuring between one signal photon and one noise photon. Since the signal and noise photons are assumed to be uncorrelated, this term is simply proportional to the product of the probabilities of detecting signal and noise photons. The last term corresponds to heralded coincidences between two noise photons. This is weighted by the statistical properties of the noise photons ($g^{(2)}_{noise}$).

In this case, we measure $g^{(2)}_{sig} = 0.0076 \pm 0.0003$ by measuring the unswitched photons without the presence of the pump pulse and $g^{(2)}_{noise} = 1.07 \pm 0.05$ by measuring the pump noise without the presence of the signal photons. Even at the highest pump powers, the number of heralded coincidences from two signal photons is several hundred times larger than the number of heralded coincidences from two noise photons. Accordingly, almost all of the increase in $g^{(2)}_{tot}$ compared to the input $g^{(2)}$ comes from the cross-term (coincidences between a signal photon and a noise photon). From Fig. 6.5, the incoherent model agrees closely with the measured $g^{(2)}_{switched}(0)$ values and the noise from the switch has only a modest effect on the statistical properties of the photon source.

6.3.1.2 JSI measurement

To verify that the switching operation does not substantially change the spectral composition of the signal, JSI measurements of the input signal and the switched signal are compared, as shown in Fig. 6.6. Both measurements are made using a signal beam generated through stimulated four wave mixing, as discussed in Chapter 4. For the input JSI, no switching pump is present, and the signal is projected on to the diagonal (unswitched) polarization. For the switched JSI, the anti-diagonal (switched) polarization is examined and the switching pump is on. From Fig. 6.6 it is apparent that there are no substantial differences in the two JSI measurements, indicating that the switching

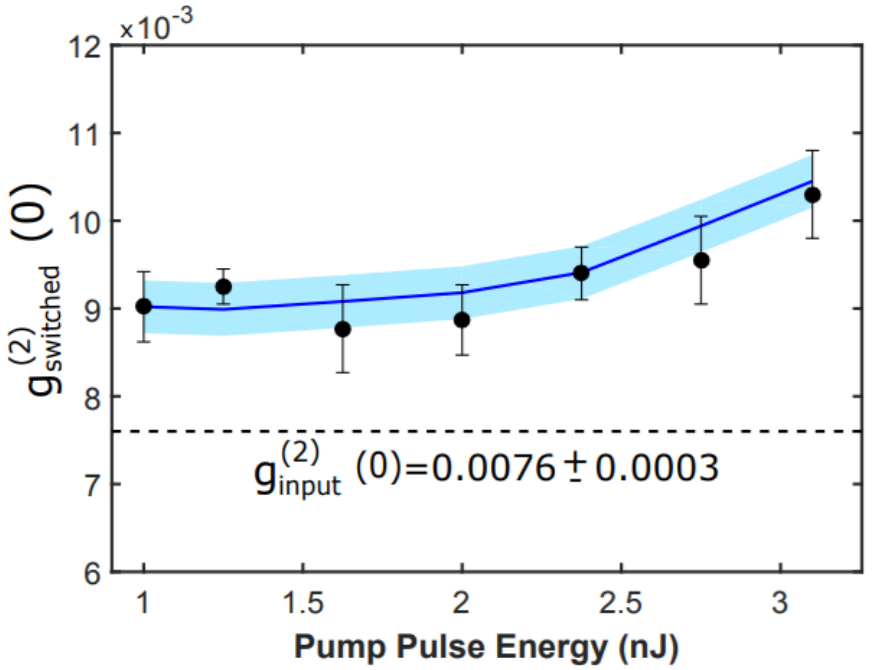

FIGURE 6.5: The measured second order auto-correlation function (black circles) of the switched signal photons shown as a function of pump pulse energy. For comparison, the $g^{(2)}(0)$ of the input signal photons is shown as a dashed line. An incoherent model is used to calculate the expected $g^{(2)}(0)$ of the switched photons (blue line, with blue shaded region denoting uncertainty) based on the measured noise counts.

operation does not affect the spectrum of the signal. However, by examining Eq. 6.2, one can see that the Kerr phase shift depends on the signal wavelength. If one was interested in switching a signal with a very large bandwidth, it should be noted that the switching efficiency would vary across the bandwidth of the signal.

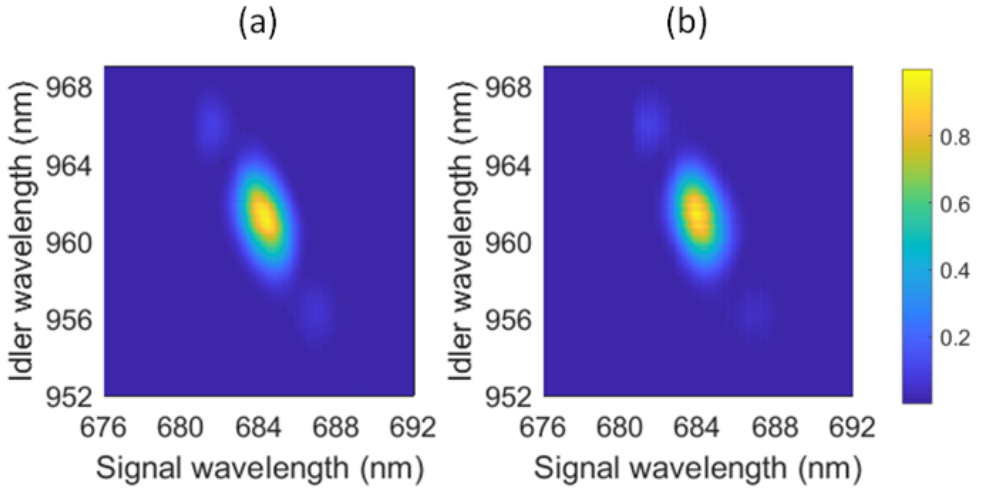

FIGURE 6.6: (a) The measured JSI of the input signal with no switching pump applied and (b) the measured JSI of the switched signal. Both measurements were made using the stimulated four wave mixing approach described in Chapter 4.

6.4 Conclusion and applications

In summary, we have demonstrated a technique for ultrafast, efficient, and low-noise switching of single photons. This technique is relatively simple to implement: all components are readily commercially available, no active stabilization is required, and efficient switching can be achieved with nanojoule pump energies. As an added benefit, this technique offers wide flexibility in both the pump and signal wavelengths.

The demonstrated switch only modestly impacts the statistical properties of single photons, making it suitable for a range of quantum processing applications. Examples of such applications include the conversion of photonic qubits [78], optical computing in a single spatial mode [88], and the processing of high dimensional and hyperentangled quantum states [89].

Time-gating of signals is another important application of this technique. In ultrafast photonics, often the timescales of interest are much shorter than the timing resolution of conventional electronics and detectors. A solution is to time-gate using a nonlinear process, such as second harmonic generation (SHG), and detect the upconverted signal [90, 91]. Kerr switching is a good alternative to SHG, which can often have low efficiencies. Time-gating signals is also used outside of quantum photonics. For example, Kerr switches have been demonstrated in both microscopy [92] and spectroscopy [93] to improve timing selectivity.

Due to range of possible applications, it may be interesting to consider further development of this technique. A user-friendly, self-contained unit for Kerr switching might be of interest for people interested in ultrafast switching or time-gating. The work demonstrated here could be extended, optimizing the switch for efficiency, flexibility, and stability, perhaps using an all-fiber approach. One could envisage such a unit as an add-on piece of technology for single photon detectors or microscopes to provide ultrafast time-gating.

Chapter 7

Conclusion

7.1 Summary

Quantum photonic technologies are an area of great potential for many applications including secure communications, sensing, and computation and simulation. Many of these technologies will require non-classical states of light in the form of single photons or photon pairs. Currently, probabilistic photon pair sources based on either spontaneous four wave mixing or spontaneous parametric down-conversion are the most common methods for producing heralded single photons or entangled photon pairs. This thesis focuses on the spectral correlations present in photon pair sources based on spontaneous four wave mixing in birefringent optical fibers. A technique for the rapid measurement of spectral correlations in photon pair sources is presented. A chirped, broadband beam is used to seed the four wave mixing interaction, generating a signal many orders of magnitude larger than the spontaneous four wave mixing case. This technique builds on previous literature to provide even faster measurements with reduced experimental complexity. While other demonstrated techniques for joint spectral measurements have measurement times on the scale of hours or minutes, the approach we demonstrate can perform measurements on the 5-30 s timescale.

We then highlight the usefulness of such a tool in the following two chapters of the thesis. In Ch. 5, we investigate how modifications to polarization maintaining fibers affect the joint spectrum of photon pair sources. The ability to adjust the joint spectrum of photon sources in a controlled way would increase the versatility and range of applications of these sources. A variety of fiber modification approaches are investigated, including squeezing, bending, and tapering the fibers. The characterization tool presented in Ch. 4 was essential, allowing for quick measurements of the joint spectrum as the fiber sources were modified. All the approaches investigated produced measurable changes in the

joint spectrum, however, the mechanisms for these changes is still not well understood. There is significant room for future work in this field to continue investigating the effects of these modifications.

In Ch. 6, we show how the joint spectral measurement tool demonstrated in Ch. 4 can be used to characterize a process, not only a source. We demonstrate an ultrafast all-optical switch at the single photon level based on the optical Kerr effect. Using the heralded single photon source outlined in Ch. 4, we achieve 97% switching efficiency and 1.6 ps switching time at nJ level pump powers, with little noise added to the single photons. Ultrafast switches such as this have a range of applications in quantum photonic networks, as well as ultrafast time-gating. We use the spectral characterization tool developed in Ch. 4 to measure what effect this switch has on the spectral properties of the input photons by comparing the joint spectral properties of both the switched and unswitched photons. From a practical perspective, we also highlight how useful such a tool is in the set-up and alignment of laboratory experiments. Having access to a bright beam with very similar properties to the single photons of interest makes nearly every step in setting up or optimizing an experiment significantly easier.

7.2 Future work

Since the work presented in Ch. 4 is a tool for joint spectral measurements, it follows that it should be used to characterize different sources and processes. While Chapters 5 and 6 have shown a few examples of this, there are many other applications of this measurement technique. Recently, some very interesting work has been done using Stimulated Emission Tomography for Quantum State Tomography (QST) [62, 63]. Using a stimulated, rather than spontaneous, process for QST has allowed groups to make measurements with much better speed and signal to noise ratios. This allows them to probe correlations which would be too experimentally difficult using traditional QST. For many of these types of experiments, using a chirped, broadband seed as demonstrated in Ch. 4 rather than a continuous wave laser to seed the nonlinear process should be feasible. This technique may be more attractive to groups who don't already have a tunable continuous wave laser, since photonic crystal fibers or other equipment for supercontinuum generation can be much less expensive than a new laser system.

The joint spectral intensity modification shown in Ch. 5 showed that there are still many aspects of this concept that are not well understood or well characterized. As such, much more work could be done in the area of fiber-based photon pair source modification. The techniques demonstrated in this thesis could certainly be extended by examining a greater number of situations. Mathematical modelling of stress profiles

within optical fibers may also provide some insight. Additionally, a larger set of fiber samples could be tested; different types of fibers, such as elliptical core, non-polarization maintaining, side-hole, and microstructured fibers may respond differently to stress, bending, and tapering. Lastly, a number of different ways of modifying these fibers could be attempted. Temperature tuning, strain, etching the fiber cladding, and writing patterns into the core or cladding of the fibers (as done in fiber-bragg gratings) could all be interesting to examine.

The fast Kerr-effect based switch demonstrated in Ch. 6 has many potential applications that would be interesting to pursue. One such application is for time-gating in spectroscopy and microscopy. In these fields, often the time-dependence of signals is relevent, but detectors provide insufficient timing resolution. A fast Kerr effect shutter could be used instead to provide timing resolution on the picosecond timescale. Particularly since many microscopy and spectroscopy systems, such as commercial Raman microscopes, are designed to be very user-friendly, a future project could involve designing a Kerr-effect based add-on to provide additional timing resolution to existing commercial microscope systems.

Bibliography

[1] M. D. Eisaman, J. Fan, A. Migdall, and S. V. Polyakov. Invited review article: Single-photon sources and detectors. *Review of Scientific Instruments*, 82(7):071101, 2011.

[2] Stefan Scheel. Single-photon sources - an introduction. *Journal of Modern Optics*, 56(2-3):141–160, 2009.

[3] Brahim Lounis and Michel Orrit. Single-photon sources. *Reports on Progress in Physics*, 68(5):1129, 2005.

[4] Charles Santori, David Fattal, Jelena Vukovi, Glenn S. Solomon, and Yoshihisa Yamamoto. Indistinguishable photons from a single-photon device. *Nature*, 419:594, October 2002.

[5] Christian Kurtsiefer, Sonja Mayer, Patrick Zarda, and Harald Weinfurter. Stable solid-state source of single photons. *Phys. Rev. Lett.*, 85:290–293, Jul 2000.

[6] Matthias Keller, Birgit Lange, Kazuhiro Hayasaka, Wolfgang Lange, and Herbert Walther. Continuous generation of single photons with controlled waveform in an ion-trap cavity system. *Nature*, 431:1075, October 2004.

[7] L.-M. Duan, M. D. Lukin, J. I. Cirac, and P. Zoller. Long-distance quantum communication with atomic ensembles and linear optics. *Nature*, 414:413, November 2001.

[8] Xing-Can Yao, Tian-Xiong Wang, Ping Xu, He Lu, Ge-Sheng Pan, Xiao-Hui Bao, Cheng-Zhi Peng, Chao-Yang Lu, Yu-Ao Chen, and Jian-Wei Pan. Observation of eight-photon entanglement. *Nature Photonics*, 6:225, February 2012.

[9] Dik Bouwmeester, Jian-Wei Pan, Klaus Mattle, Manfred Eibl, Harald Weinfurter, and Anton Zeilinger. Experimental quantum teleportation. *Nature*, 390:575, December 1997.

[10] E. Knill, R. Laflamme, and G. J. Milburn. A scheme for efficient quantum computation with linear optics. *Nature*, 409:46–52, January 2001.

[11] Alois Mair, Alipasha Vaziri, Gregor Weihs, and Anton Zeilinger. Entanglement of the orbital angular momentum states of photons. *Nature*, 412:313, July 2001.

[12] Paul G. Kwiat, Klaus Mattle, Harald Weinfurter, Anton Zeilinger, Alexander V. Sergienko, and Yanhua Shih. New high-intensity source of polarization-entangled photon pairs. *Phys. Rev. Lett.*, 75:4337–4341, Dec 1995.

[13] Nicolas Gisin, Grégoire Ribordy, Wolfgang Tittel, and Hugo Zbinden. Quantum cryptography. *Rev. Mod. Phys.*, 74:145–195, Mar 2002.

[14] Tobias Schmitt-Manderbach, Henning Weier, Martin Fürst, Rupert Ursin, Felix Tiefenbacher, Thomas Scheidl, Josep Perdigues, Zoran Sodnik, Christian Kurtsiefer, John G. Rarity, Anton Zeilinger, and Harald Weinfurter. Experimental demonstration of free-space decoy-state quantum key distribution over 144 km. *Phys. Rev. Lett.*, 98:010504, Jan 2007.

[15] C. L. Degen, F. Reinhard, and P. Cappellaro. Quantum sensing. *Rev. Mod. Phys.*, 89:035002, Jul 2017.

[16] Vittorio Giovannetti, Seth Lloyd, and Lorenzo Maccone. Quantum metrology. *Phys. Rev. Lett.*, 96:010401, Jan 2006.

[17] Seth Lloyd. Enhanced sensitivity of photodetection via quantum illumination. *Science*, 321(5895):1463–1465, 2008.

[18] Ryan S. Bennink, Sean J. Bentley, Robert W. Boyd, and John C. Howell. Quantum and classical coincidence imaging. *Phys. Rev. Lett.*, 92:033601, Jan 2004.

[19] Justin B. Spring, Benjamin J. Metcalf, Peter C. Humphreys, W. Steven Kolthammer, Xian-Min Jin, Marco Barbieri, Animesh Datta, Nicholas Thomas-Peter, Nathan K. Langford, Dmytro Kundys, James C. Gates, Brian J. Smith, Peter G. R. Smith, and Ian A. Walmsley. Boson sampling on a photonic chip. *Science*, 2012.

[20] T. D. Ladd, F. Jelezko, R. Laflamme, Y. Nakamura, C. Monroe, and J. L. OBrien. Quantum computers. *Nature*, 464:45, March 2010.

[21] Peter W. Shor. Polynomial-time algorithms for prime factorization and discrete logarithms on a quantum computer. *SIAM Rev.*, 41:303–332, 1996.

[22] Christof Zalka. Efficient simulation of quantum systems by quantum computers. *Fortschritte der Physik*, 46(68):877–879.

[23] Andrew Steane. Quantum computing. *Reports on Progress in Physics*, 61:117, Feb 1998.

[24] P. Walther, K. J. Resch, T. Rudolph, E. Schenck, H. Weinfurter, V. Vedral, M. Aspelmeyer, and A. Zeilinger. Experimental one-way quantum computing. *Nature*, 434:169, March 2005.

[25] Robert Prevedel, Philip Walther, Felix Tiefenbacher, Pascal Bhi, Rainer Kaltenbaek, Thomas Jennewein, and Anton Zeilinger. High-speed linear optics quantum computing using active feed-forward. *Nature*, 445:65–9, 02 2007.

[26] Ying Li, Peter C. Humphreys, Gabriel J. Mendoza, and Simon C. Benjamin. Resource costs for fault-tolerant linear optical quantum computing. *Phys. Rev. X*, 5:041007, Oct 2015.

[27] Scott Aaronson and Alex Arkhipov. The computational complexity of linear optics. In *Proceedings of the Forty-third Annual ACM Symposium on Theory of Computing*, STOC '11, pages 333–342, New York, NY, USA, 2011. ACM.

[28] B. T. Gard, K. R. Motes, J. P. Olson, P. P. Rohde, and J. P. Dowling. *An Introduction to Boson-Sampling*, pages 167–192. World Scientific Publishing Co, June 2015.

[29] Matthew A. Broome, Alessandro Fedrizzi, Saleh Rahimi-Keshari, Justin Dove, Scott Aaronson, Timothy C. Ralph, and Andrew G. White. Photonic boson sampling in a tunable circuit. *Science*, 339(6121):794–798, 2013.

[30] C. H. Bennett and G. Brassard. Quantum cryptography: Public-key distribution and coin tossing. In *Proceedings of IEEE International Conference on Computers, Systems and Signal Processing, Bangalore, India, 1984*, pages 175–179. IEEE Press, 1984.

[31] Thomas Jennewein, Christoph Simon, Gregor Weihs, Harald Weinfurter, and Anton Zeilinger. Quantum cryptography with entangled photons. *Phys. Rev. Lett.*, 84:4729–4732, May 2000.

[32] R. Ursin, F. Tiefenbacher, T. Schmitt-Manderbach, H. Weier, T. Scheidl, M. Lindenthal, B. Blauensteiner, T. Jennewein, J. Perdigues, P. Trojek, B. mer, M. Frst, M. Meyenburg, J. Rarity, Z. Sodnik, C. Barbieri, H. Weinfurter, and A. Zeilinger. Entanglement-based quantum communication over 144km. *Nature Physics*, 3:481, June 2007.

[33] Simon Grblacher, Thomas Jennewein, Alipasha Vaziri, Gregor Weihs, and Anton Zeilinger. Experimental quantum cryptography with qutrits. *New Journal of Physics*, 8(5):75, 2006.

[34] Alicia Sit, Frédéric Bouchard, Robert Fickler, Jérémie Gagnon-Bischoff, Hugo Larocque, Khabat Heshami, Dominique Elser, Christian Peuntinger, Kevin Günthner, Bettina Heim, Christoph Marquardt, Gerd Leuchs, Robert W. Boyd, and Ebrahim Karimi. High-dimensional intracity quantum cryptography with structured photons. *Optica*, 4(9):1006–1010, Sep 2017.

[35] M. Sasaki, M. Fujiwara, H. Ishizuka, W. Klaus, K. Wakui, M. Takeoka, S. Miki, T. Yamashita, Z. Wang, A. Tanaka, K. Yoshino, Y. Nambu, S. Takahashi, A. Tajima, A. Tomita, T. Domeki, T. Hasegawa, Y. Sakai, H. Kobayashi, T. Asai, K. Shimizu, T. Tokura, T. Tsurumaru, M. Matsui, T. Honjo, K. Tamaki, H. Takesue, Y. Tokura, J. F. Dynes, A. R. Dixon, A. W. Sharpe, Z. L. Yuan, A. J. Shields, S. Uchikoga, M. Legré, S. Robyr, P. Trinkler, L. Monat, J.-B. Page, G. Ribordy, A. Poppe, A. Allacher, O. Maurhart, T. Länger, M. Peev, and A. Zeilinger. Field test of quantum key distribution in the tokyo qkd network. *Opt. Express*, 19(11):10387–10409, May 2011.

[36] Sheng-Kai Liao, Wen-Qi Cai, Wei-Yue Liu, Liang Zhang, Yang Li, Ji-Gang Ren, Juan Yin, Qi Shen, Yuan Cao, Zheng-Ping Li, Feng-Zhi Li, Xia-Wei Chen, Li-Hua Sun, Jian-Jun Jia, Jin-Cai Wu, Xiao-Jun Jiang, Jian-Feng Wang, Yong-Mei Huang, Qiang Wang, Yi-Lin Zhou, Lei Deng, Tao Xi, Lu Ma, Tai Hu, Qiang Zhang, Yu-Ao Chen, Nai-Le Liu, Xiang-Bin Wang, Zhen-Cai Zhu, Chao-Yang Lu, Rong Shu, Cheng-Zhi Peng, Jian-Yu Wang, and Jian-Wei Pan. Satellite-to-ground quantum key distribution. *Nature*, 549:43, August 2017.

[37] Z. Vernon, M. Menotti, C. C. Tison, J. A. Steidle, M. L. Fanto, P. M. Thomas, S. F. Preble, A. M. Smith, P. M. Alsing, M. Liscidini, and J. E. Sipe. Truly unentangled photon pairs without spectral filtering. *Opt. Lett.*, 42(18):3638–3641, Sep 2017.

[38] Robert W. Boyd. *Nonlinear Optics*. Elsevier Inc., third edition edition, 2008.

[39] Mark Fox. *Quantum Optics: an introduction*. Oxford University Press, 2006.

[40] Christopher C. Gerry and Peter L. Knight. *Introductory Quantum Optics*. Cambridge University Press, 2005.

[41] J. Noda, K. Okamoto, and Y. Sasaki. Polarization-maintaining fibers and their applications. *Journal of Lightwave Technology*, 4(8):1071–1089, Aug 1986.

[42] H. Jin, F. M. Liu, P. Xu, J. L. Xia, M. L. Zhong, Y. Yuan, J. W. Zhou, Y. X. Gong, W. Wang, and S. N. Zhu. On-chip generation and manipulation of entangled photons based on reconfigurable lithium-niobate waveguide circuits. *Phys. Rev. Lett.*, 113:103601, Sep 2014.

[43] S. Tanzilli, H. De Riedmatten, W. Tittel, H. Zbinden, P. Baldi, M. De Micheli, D.B. Ostrowsky, and N. Gisin. Highly efficient photon-pair source using periodically poled lithium niobate waveguide. *Electronics Letters*, 37:26–28(2), January 2001.

[44] J. W. Silverstone, D. Bonneau, K. Ohira, N. Suzuki, H. Yoshida, N. Iizuka, M. Ezaki, C. M. Natarajan, M. G. Tanner, R. H. Hadfield, V. Zwiller, G. D. Marshall, J. G. Rarity, J. L. O'Brien, and M. G. Thompson. On-chip quantum interference between silicon photon-pair sources. *Nature Photonics*, 8:104, December 2013.

[45] P. Ben Dixon, Danna Rosenberg, Veronika Stelmakh, Matthew E. Grein, Ryan S. Bennink, Eric A. Dauler, Andrew J. Kerman, Richard J. Molnar, and Franco N. C. Wong. Heralding efficiency and correlated-mode coupling of near-ir fiber-coupled photon pairs. *Phys. Rev. A*, 90:043804, Oct 2014.

[46] Marlan O. Scully and M. Suhail Zubairy. *Quantum Optics*. Cambridge University Press, 1997.

[47] Justin B. Spring, Patrick S. Salter, Benjamin J. Metcalf, Peter C. Humphreys, Merritt Moore, Nicholas Thomas-Peter, Marco Barbieri, Xian-Min Jin, Nathan K. Langford, W. Steven Kolthammer, Martin J. Booth, and Ian A. Walmsley. On-chip low loss heralded source of pure single photons. *Opt. Express*, 21(11):13522–13532, Jun 2013.

[48] Jun Chen, Aaron J. Pearlman, Alexander Ling, Jingyun Fan, and Alan Migdall. A versatile waveguide source of photon pairs for chip-scale quantum information processing. *Opt. Express*, 17(8):6727–6740, Apr 2009.

[49] Kim Fook Lee, Jun Chen, Chuang Liang, Xiaoying Li, Paul L. Voss, and Prem Kumar. Generation of high-purity telecom-band entangled photon pairs in dispersion-shifted fiber. *Opt. Lett.*, 31(12):1905–1907, Jun 2006.

[50] Wolfgang Mauerer, Malte Avenhaus, Wolfram Helwig, and Christine Silberhorn. How colors influence numbers: Photon statistics of parametric down-conversion. *Phys. Rev. A*, 80:053815, Nov 2009.

[51] Bahaa E. A. Saleh and Malvin Carl Teich. *Fundamentals of Photonics*. John Wiley & Sons, Inc., 2001.

[52] Peter J. Mosley, Jeff S. Lundeen, Brian J. Smith, Piotr Wasylczyk, Alfred B. U'Ren, Christine Silberhorn, and Ian A. Walmsley. Heralded generation of ultrafast single photons in pure quantum states. *Phys. Rev. Lett.*, 100:133601, Apr 2008.

[53] Kevin Zielnicki, Karina Garay-Palmett, Daniel Cruz-Delgado, Hector Cruz-Ramirez, Michael F. OBoyle, Bin Fang, Virginia O. Lorenz, Alfred B. URen, and Paul G. Kwiat. Joint spectral characterization of photon-pair sources. *Journal of Modern Optics*, 0(0):1–20, 2018.

[54] Brian Smith, J. P. Mahou, Offir Cohen, J. S. Lundeen, and I. A. Walmsley. Photon pair generation in birefringent optical fibers. *Optics Express*, 17-26:23589–23602, 2009.

[55] Iman Jizan, Bryn Bell, L. G. Helt, Alvaro Casas Bedoya, Chunle Xiong, and Benjamin J. Eggleton. Phase-sensitive tomography of the joint spectral amplitude of photon pair sources. *Opt. Lett.*, 41(20):4803–4806, Oct 2016.

[56] Andreas Eckstein, Guillaume Boucher, Aristide Lematre, Pascal Filloux, Ivan Favero, Giuseppe Leo, John E. Sipe, Marco Liscidini, and Sara Ducci. High-resolution spectral characterization of two photon states via classical measurements. *Laser & Photonics Reviews*, 8(5):L76–L80, 2014.

[57] Malte Avenhaus, Andreas Eckstein, Peter J. Mosley, and Christine Silberhorn. Fiber-assisted single-photon spectrograph. *Opt. Lett.*, 34(18):2873–2875, Sep 2009.

[58] Alex O. C. Davis, Paul M. Saulnier, Michal Karpinski, and Brian J. Smith. Pulsed single-photon spectrometer by frequency-to-time mapping using chirped fiber bragg gratings. *Optics Express*, 25(11):12804–12811, May 2017.

[59] P. Hariharan. *Basics of Interferometry*. Elsevier Inc., second edition edition, 2007.

[60] M. Liscidini and J. E. Sipe. Stimulated emission tomography. *Physical Review Letters*, 111:193602, 2013.

[61] Bin Fang, Offir Cohen, Marco Liscidini, John E. Sipe, and Virginia O. Lorenz. Fast and highly resolved capture of the joint spectral density of photon pairs. *Optica*, 1-5:281–284, 2014.

[62] B. Fang, M. Liscidini, J. E. Sipe, and V. O. Lorenz. Multidimensional characterization of an entangled photon-pair source via stimulated emission tomography. *Opt. Express*, 24(9):10013–10019, May 2016.

[63] Lee A. Rozema, Chao Wang, Dylan H. Mahler, Alex Hayat, Aephraim M. Steinberg, John E. Sipe, and Marco Liscidini. Characterizing an entangled-photon source with classical detectors and measurements. *Optica*, 2(5):430–433, May 2015.

[64] Jennifer Erskine, Duncan England, Connor Kupchak, and Benjamin Sussman. Real-time spectral characterization of a photon pair source using a chirped supercontinuum seed. *Opt. Lett.*, 43(4):907–910, Feb 2018.

[65] John M. Dudley, Goëry Genty, and Stéphane Coen. Supercontinuum generation in photonic crystal fiber. *Rev. Mod. Phys.*, 78:1135–1184, Oct 2006.

[66] Karen Marie Hilligsøe, Thomas Vestergaard Andersen, Henrik Nørgaard Paulsen, Carsten Krogh Nielsen, Klaus Mølmer, Søren Keiding, Rene Kristiansen, Kim Per Hansen, and Jakob Juul Larsen. Supercontinuum generation in a photonic crystal fiber with two zero dispersion wavelengths. *Opt. Express*, 12(6):1045–1054, Mar 2004.

[67] M. Lorenc, M. Ziolek, R. Naskrecki, J. Karolczak, J. Kubicki, and A. Maciejewski. Artifacts in femtosecond transient absorption spectroscopy. *Applied Physics B*, 74(1):19–27, Jan 2002.

[68] M. N. Islam, L. F. Mollenauer, and R. H. Stolen. Cross-phase modulation in optical fibers. *Optics Letters*, 12:625–627, Aug 1987.

[69] Hee Gap Park, Jae Dong Park, and Sang Soo Lee. Pump-intensity-dependent frequency shift in stokes and anti-stokes spectra generated by stimulated four-photon mixing in birefringent fiber. *Appl. Opt.*, 26(15):2974–2978, Aug 1987.

[70] Nori Shibata, Masaharu Ohashi, Ken ichi Kitayama, and Shigeyuki Seikai. Evaluation of bending-induced birefringence based on stimulated four-photon mixing. *Opt. Lett.*, 10(3):154–156, Mar 1985.

[71] Kenichi Kitayama and Masaharu Ohashi. Frequency tuning for stimulated fourphoton mixing by bendinginduced birefringence in a singlemode fiber. *Applied Physics Letters*, 41(7):619–621, 1982.

[72] Kenichi Kitayama, Shigeyuki Seikai, and Naoya Uchida. Stress-induced frequency tuning for stimulated fourphoton mixing in a birefringent singlemode fiber. *Applied Physics Letters*, 41(4):322–324, 1982.

[73] C. Kerbage, P. Steinvurzel, P. Reyes, P. S. Westbrook, R. S. Windeler, A. Hale, and B. J. Eggleton. Highly tunable birefringent microstructured optical fiber. *Opt. Lett.*, 27(10):842–844, May 2002.

[74] Newport Corporation. Polarization in fiber optics, 2018.

[75] J. Sakai and T. Kimura. Birefringence and polarization characteristics of singlemode optical fibers under elastic deformations. *IEEE Journal of Quantum Electronics*, 17(6):1041–1051, June 1981.

[76] E. S. Jog and R. S. Krishnan. Dispersion of the photoelastic constants of fused silica. *Nature*, 179:540, March 1957.

[77] J. D. Love, W. M. Henry, W. J. Stewart, R. J. Black, S. Lacroix, and F. Gonthier. Tapered single-mode fibres and devices. i. adiabaticity criteria. *IEE Proceedings J - Optoelectronics*, 138(5):343–354, Oct 1991.

[78] Connor Kupchak, Philip J. Bustard, Khabat Heshami, Jennifer Erskine, Michael Spanner, Duncan G. England, and Benjamin J. Sussman. Time-bin-to-polarization conversion of ultrafast photonic qubits. *Phys. Rev. A*, 96:053812, Nov 2017.

[79] Matthew A. Hall, Joseph B. Altepeter, and Prem Kumar. Ultrafast switching of photonic entanglement. *Phys. Rev. Lett.*, 106:053901, Feb 2011.

[80] Caleb Knoernschild, Changsoon Kim, Felix P. Lu, and Jungsang Kim. Multiplexed broadband beam steering system utilizing high speed mems mirrors. *Opt. Express*, 17(9):7233–7244, Apr 2009.

[81] Vilson R. Almeida, Carlos A. Barrios, Roberto R. Panepucci, Michal Lipson, Mark A. Foster, Dimitre G. Ouzounov, and Alexander L. Gaeta. All-optical switching on a silicon chip. *Opt. Lett.*, 29(24):2867–2869, Dec 2004.

[82] K. J. Blow, N. J. Doran, B. K. Nayar, and B. P. Nelson. Two-wavelength operation of the nonlinear fiber loop mirror. *Opt. Lett.*, 15(4):248–250, Feb 1990.

[83] N. N. Oza, Y. P. Huang, and P. Kumar. Entanglement-preserving photonic switching: Full cross-bar operation with quantum data streams. *IEEE Photonics Technology Letters*, 26(4):356–359, Feb 2014.

[84] J. Etchepare, G. Grillon, R. Muller, and A. Orszag. Kinetics of optical kerr effect induced by picosecond laser pulses. *Optics Communications*, 34(2):269 – 272, 1980.

[85] Hirohisa Kanbara, Hideki Kobayashi, Toshikuni Kaino, Takashi Kurihara, Naoki Ooba, and Ken'ichi Kubodera. Highly efficient ultrafast optical kerr shutters with the use of organic nonlinear materials. *J. Opt. Soc. Am. B*, 11(11):2216–2223, Nov 1994.

[86] I. H. Malitson. Interspecimen comparison of the refractive index of fused silica∗,. *J. Opt. Soc. Am.*, 55(10):1205–1209, Oct 1965.

[87] P S Michelberger, T F M Champion, M R Sprague, K T Kaczmarek, M Barbieri, X M Jin, D G England, W S Kolthammer, D J Saunders, J Nunn, and I A Walmsley. Interfacing ghz-bandwidth heralded single photons with a warm vapour raman memory. *New Journal of Physics*, 17(4):043006, 2015.

[88] Peter C. Humphreys, Benjamin J. Metcalf, Justin B. Spring, Merritt Moore, Xian-Min Jin, Marco Barbieri, W. Steven Kolthammer, and Ian A. Walmsley. Linear

optical quantum computing in a single spatial mode. *Phys. Rev. Lett.*, 111:150501, Oct 2013.

[89] Takuya Ikuta and Hiroki Takesue. Implementation of quantum state tomography for time-bin qudits. *New Journal of Physics*, 19(1):013039, 2017.

[90] Jean-Philippe W. MacLean, John M. Donohue, and Kevin J. Resch. Direct characterization of ultrafast energy-time entangled photon pairs. *Phys. Rev. Lett.*, 120:053601, Jan 2018.

[91] John M. Donohue, Megan Agnew, Jonathan Lavoie, and Kevin J. Resch. Coherent ultrafast measurement of time-bin encoded photons. *Phys. Rev. Lett.*, 111:153602, Oct 2013.

[92] Jolie C. Blake, Jesus Nieto-Pescador, Zhengxin Li, and Lars Gundlach. Ultraviolet femtosecond kerr-gated wide-field fluorescence microscopy. *Opt. Lett.*, 41(11):2462–2465, Jun 2016.

[93] J. Takeda, K. Nakajima, S. Kurita, S. Tomimoto, S. Saito, and T. Suemoto. Time-resolved luminescence spectroscopy by the optical kerr-gate method applicable to ultrafast relaxation processes. *Phys. Rev. B*, 62:10083–10087, Oct 2000.